2008

Instability of stagnation and attachment line icing

Shourya Prakash Otta
Iowa State University

Stability of stagnation and attachment line icing

by

Shourya Prakash Otta

A dissertation submitted to the graduate faculty

in partial fulfillment of the requirements for the degree of

DOCTOR OF PHILOSOPHY

Major: Aerospace Engineering

Program of Study Committee:
Alric P. Rothmayer, Major Professor
Paul Durbin
Z J Wang
Tom I-P Shih
Srinivas Aluru

Iowa State University

Ames, Iowa

2009

Dedication

Dedicated to my parents,

who have always inspired and encouraged me, and

Divine Grace

without which nothing happens.

TABLE OF CONTENTS

LIST OF TABLES

LIST OF FIGURES

NOMENCLATURE

$\mathcal{T}$	Free-stream air temperature perturbation from wall temperature
Re	Reynolds number
V_∞, T_∞	Free-stream velocity and temperature
M_∞	Free-stream Mach number
ξ, η, ζ	Scaled Hiemenz flow coordinates
$\hat{T}$	Non-dimensional perturbation temperature within the boundary layer
ΔT^*	Dimensional temperature difference between the free-stream and the wall
m_∞	Parameter relating $\mathcal{T}$ and M_∞
Pr	Prandtl number
λ	Sweep angle
$\bar{\Lambda}$	Scaled sweep angle parameter in the stagnation flow
f	Stream function for the stagnation flow
g	Scaled sweep velocity in the attachment line flow
F	Scaled streamwise velocity in air boundary layer over a parabola
$\bar{V}$	Scaled vertical velocity in air boundary layer over a parabola
h	Scaled sweep velocity in air boundary layer over a parabola
$\mathcal{K}, \mathcal{M}$	Film inertia parameters
K_{wa}	Water/air thermal conductivity ratio
D_{aw}	Air/water density ratio
D_{iw}	Ice/water density ratio

K_{iw}	Ice/water conductivity ratio
C_{ai}	Air/ice specific heat ratio
C_{aw}	Air/water specific heat ratio
Ste	Stefan number
LWC	Liquid water content
β_{CE}	Collection efficiency

Subscripts

air	Variables defined in air
$water$	Variables defined in water
ice	Variables defined in ice
∞	Free-stream quantities
H	Hiemenz flow variable

Superscripts

$\hat{}$	Non-dimensional perturbation temperature within the boundary layer
$*$	Dimensional quantities

Greek symbols

σ, γ_g	Surface tension of water
ρ	Density
γ	Specific heat ratio in air
κ	Surface curvature
ε	Gibbs-Thomson parameter
μ	Viscosity
α, β	Streamwise and spanwise wave numbers

ACKNOWLEDGEMENTS

I wish to thank my advisor Dr. Alric Rothmayer for his constant guidance, inspiration and financial support thoughout my stay because of which this work has been possible. I especially want to thank him for helping me develop a sound understanding of the icing problem, and for his patience in allowing me the time to do it. I wish to thank Dr. Mario Vargas and Dr. Paul Tsao for providing me the pictures of experiments conducted at NASA Glenn Icing Research Tunnel and figures from their papers and Dr. Emmanuel Montreil for the permission to use a picture from his icing experiments at ONERA. I wish to thank Dr. Mark Potapczuk at the NASA Glenn Research Center and Mr. Thomas Bond at the Federal Aviation Administration for their helpful guidance and support. This research was partially supported by the Icing Branch at the NASA Glenn Research Center under contract NAG-3-2863. I would like to thank Dr. Tom Shih, Dr. Paul Durbin and Dr. Z. J. Wang for graciously agreeing to be on my committee. I am most obliged to Dr. Srinivas Aluru for his consent to be the minor representative on my committee. I would also like to acknowledge the support of the Department of Aerospace Engineering and Dr. Tom Shih for the funding through the teaching assistantships. I wish to thank my office mates Brian Matheis & Guoqing Wang for many interesting discussions. I wish to thank the graduate secretary Ms. Delora Pfeiffer for her help.

I wish to acknowledge the help and advice of my undergraduate advisor Dr. C. Venkatesan at IIT Kanpur. I would also like to thank Dr. T. K. Sengupta, Dr. S. Kamle and Dr. K. S. Ravichandran for their recommendations which helped me come to Iowa State.

I was very fortunate to have many friends from my undergraduate days in IIT Kanpur here at Iowa State and also met many more new friends. I would like to acknowledge the help and advice of Vipul Katyal and Vikas Yadav, Hullas Sehgal for his great supply of jokes and Pranav Agarwal, all of whom are from the batch of Y2K (in electrical engineering in ISU) and also Janhavi Agashe for many discussions. I especially thank Shakti Chauhan for his help and advice in my job search. I wish to thank Rishabh Mehandru for his continuous encouragement and numerous suggestions. Bipin Singh and Tanuj Aggarwal were great roommates. I wish to thank Senthan Swaminathan for his insightful suggestions and advice. Sudipta De often encouraged me to work on a PhD and also took the time to discuss many philosophical issues. I thank Oscar Murrillo for our flight to Iowa Aviation Museum. I thank Susanta Nanda, Sriram Rallabhandi, Sudarshan Koushik, Anwitaman Datta and many other friends who kept in touch with me over the years and helped me on many occasions.

Last and most important is the patience and constant encouragement of my father, Mr. Prabodh Kumar Otta, my mother, Ms. Simantini Dwibedi, my sister, Swagatika Otta, and my brother Sitikantha Otta, because of which I am achieving this milestone in my life.

ABSTRACT

Ice accretion for in-flight icing conditions often yields complicated shapes which can significantly affect the performance of an aircraft. This has been a primary motivation for numerous studies to understand the physics of ice formation on aircraft and develop prediction methodologies. During icing experiments, many of the complex shapes found in later stages of ice accretion have been observed to their origins in ice roughnesses which form early in the ice accretion process.

The present work focuses on the formation of roughnesses due to the inherent interfacial instabilities of a wetted ice surface. Solutions are found using a multiple scales model for the stagnation region near the leading edge of a wing. In the computations for both unswept and swept wing icing, the roughness sizes are found to be about the same size as the air boundary layer thickness. These roughnesses qualitatively agree with the typical geometries and properties of the roughnesses seen in unswept and swept wing icing experiments.

Using the multiple scales model for the stagnation region as a guide, a preliminary simplified engineering linear stability analysis is developed for glaze icing. The roughness diameters predicted using this model generally agree with the typical characteristics of the ice roughnesses seen in experiments providing that the airfoil surface temperature is sufficiently close to freezing. Smooth zones devoid of roughnesses, which have a sharp demarcation between the smooth and rough regions, can be present near the

stagnation line. However, the solutions of the linear stability model are found to be overly sensitive to the temperature of the airfoil, which suggests the need for further modeling to incorporate the transient changes in the airfoil skin temperature and ice thickness during the ice accretion process.

CHAPTER 1. INTRODUCTION

Complex ice shapes often form on aircraft surfaces such as wings, propellers, turbine engines and helicopter blades in a variety of atmospheric conditions, usually with supercooled water droplets in the cloud. These ice shapes can have a significant adverse effect on the aerodynamic properties of these surfaces. For example, ice accretion on wings can have a significant influence on the aerodynamics of the wing, which can lead to loss of lift as well as adversely affect flight control. Numerous accidents have been attributed to ice buildup on wings, such as the in-flight encounter with icing and the resulting uncontrolled collision with terrain of Comair flight 3272, an Embraer 120RT on January 9, 1997 (see National Transport Safety Board Report [7]) and also the in-flight icing encounter and loss of control of American Eagle Flight 4184 (see National Transport Safety Board Report [8]). As a result, the National Transportation Safety Board (NTSB) lists aircraft icing as one of the major challenges facing aviation safety. Better understanding of icing phenomena can lead to development of improved ice protection systems to help prevent in-flight icing and the resulting accidents.

Aircraft icing happens when small supercooled liquid water droplets impact and freeze on an aircraft surface causing ice to grow on the surface (see Fig. 1.1, also see Gent *et al* [9] for a general introduction to the aircraft icing problem, and see Poots [10] for other icing problems, such as ice accretion on power cables and towers). Supercooled water droplets which are present in the airflow impact the aircraft when it is passing through clouds (see Pruppacher and Klett [11] for the physics of these water droplets and the clouds containing them). These supercooled water droplets follow trajectories which

Figure 1.1 A typical ice accretion on an aircraft wing (courtesy: NASA Glenn Research Center).

are influenced by the airflow. While the droplets are often assumed to be deposited uniformly over the surface, the local effects of splashing can be important for larger drops (see Tan and Papadakis [12]). Depending on the ambient temperature in the airflow, these supercooled water droplets might completely or partially freeze. There are two main types of ice accretion: rime ice, without any significant residual water surface present on the ice, and glaze ice, which has residual water on the ice surface. Rime ice is opaque, occurs in colder conditions and leads to relatively simple macroscopic ice shapes (albeit very complex microscopic shapes). However, for temperatures close to freezing, the entire mass of water coming onto the surface does not freeze and there is a combination of water and ice on the surface. Such an ice formation is referred to as glaze ice. Glaze ice often leads to more complex ice shapes due to a combination of effects, such as the heat transfer from air, the heat flux within the ice and the transport of water on the ice surface. As a result, the prediction of glaze ice shapes continues to be a challenging problem.

The development of ice accretion codes for prediction of ice shapes and aircraft cer-

tification is an integral part of icing studies. A brief review of the icing codes is given here. LEWICE, and LEWICE3D are the ice accretion codes developed by the Icing Research Branch of NASA Glenn Research Center (see Wright [13] and Bidwell *et al.* [14]). FENSAP-ICE (see Bourgault, Beaugendre, and Habashi [15] and Beaugendre, Morency and Habashi [16]) and CANICE (see Tran *et al.* [17]) are Canadian codes for ice accretion developed by Newmerical Technologies and Bombardier Aerospace respectively [17]. ICECREMO (see Myers[18], Myers and Charpin [19] and Myers *et al.* [20]) and TRAJICE2 (see Gent [21]) are British ice accretion codes developed by DERA and defense industries in the UK. These icing codes involve a thermodynamic balance at the ice surface using some variant of the Messinger model (see Messinger [22]) and predict a relatively smooth macroscopic ice growth. However, the real ice accretion process is very complex on the shorter scales and there is often a significant mismatch between computed ice shapes and experimental ice shapes in experiments for identical flow conditions, and also between experimental ice shapes seen after repeating the same flow conditions. This makes the simulation of ice accretion a challenging exercise. There are four main components to numerically predicting ice accretion : (a) computation of the airflow (b) computation of droplet trajectories and the resulting water mass accumulation (c) computation of the water transport over the ice surface, and finally (d) computing the ice growth. Computation of the airflow may range from a simple inviscid flow calculation, with an associated boundary layer calculation, to a full-blown Navier-Stokes problem. The droplet trajectories are often computed using either Eulerian or Lagrangian methods (see Bourgalt, Boutanios and Habashi [23]). For example, LEWICE is a two-dimensional ice accretion code which uses an inviscid panel method with Lagrangian droplet trajectories, and does a reasonable job of matching experiments for unswept rime ice accretion (see Wright [24]). LEWICE3D uses a three-dimensional panel code and applies the two-dimensional ice accretion model along the streamlines (see Bidwell *et al.* [14]). However, this approach was found to be inadequate to predict

the complex ice structures seen in swept wings (see Vargas [25]). A similar deficiency is seen in other ice accretion codes. The three dimensional nature of the ice growth is thought to be a principal reason for the problems seen in these codes. This implies that while there has been significant progress in recent years towards understanding ice accretion, much remains to be done to add full three dimensional capability to ice accretion codes. One of the goals for the development of next generation of ice accretion codes is to include the underlying physics in order to produce more realistic ice shapes (see Potapczuk [26]). This necessitates a better understanding of the physical processes leading to small scale ice roughnesses often seen in aircraft icing and the link between these roughnesses and the final ice shapes.

Icing experiments have been important in gaining insight into the physical processes involved in ice accretion. These experiments simulate in-flight aircraft icing conditions in icing wind tunnels, such as the Icing Research Tunnel(IRT) at NASA Glenn Research Center. Ideally, airfoils with geometries which are self-similar to the aircraft's wing are exposed to scaled test conditions found from the icing conditions for the aircraft. Usually, the airstream is colder than the freezing temperature of water. Typical characteristics of the ice formation are measured by hand tracing the ice or from analysis of photographs.

Ice accretion seen in experiments often consists of two separate growths: a macroscale ice growth, and a microscale ice roughness growth which contributes to the formation of the complex macroscopic ice shapes. These natural ice roughnesses vary greatly for different conditions and play a key role in the local heat transfer in the airflow and the evolution of the water on the ice surface. They also influence the growth of larger ice structures seen later in the ice accretion process (see Cebeci and Kafyeke [27] and Vargas [25]).

The formation of the natural ice roughnesses in unswept ice accretion and their characterization has been the focus of numerous icing experimental studies. Hansman and Turnock [28] investigated the interaction of ice roughnesses with the mass transport

of water over an ice surface in glaze icing conditions. In 1994, Shin [29, 30] observed the presence of a smooth zone near the stagnation line devoid of roughness and measured typical diameters of roughness elements in the region beyond this smooth zone. Anderson and Shin [31] note the correlation between the sizes of the roughness and the different experimental parameters, which account for the amount of water being frozen on the surface. Later, detailed experiments by Anderson, Hentschel and Ruff [1] gave more information about the typical sizes of these roughnesses as well as the widths of the smooth zones, and confirmed the decrease of the smooth zone width with increasing time for ice accretion.

The glaze ice roughnesses near the stagnation line influence the airflow and thus, the local heat flux from air which, in turn, affects further ice growth. In 1995, Henry, Hansman and Breuer [32] found that heat transfer enhancement occurs upstream of the roughnesses up to very near the roughnesses and shows a rapid decay thereafter. Navier-Stokes computations of Matheis [33] also show the effect of roughness fields on local heat transfer near the leading edge of an airfoil. This is important because recent experiments have shown that the glaze ice feathers discussed later in this chapter grow from clusters of natural ice roughness elements over a relatively smooth ice surface (see Vargas and Tsao [2] and Vargas, Tsao and Rothmayer [4]).

Inclination of the flow with respect to the wing has a strong influence on the ice formations. For unswept wings, the ice accretion shows horn-shaped macroscopic ice shapes on both sides of the stagnation line. However, the ice accretion becomes more three-dimensional for swept wings (see Vargas and Reshotko [34, 35, 36] and Vargas, Giriunas and Ratvasky [37]). In swept wing ice accretion, there are ice structures called "scallops" which are present across the span of the wing. The ice shapes for swept wings have a spanwise three-dimensional structure which lacks a two-dimensional projection (see Fig. 4.1). In addition, both unswept and swept wing ice accretion have glaze ice roughnesses close to the stagnation line and ice structures called feathers well down-

stream from the stagnation line. These roughnesses and feathers often influence the ice shapes seen in later phases of ice accretion. The understanding of the formation of these natural ice roughnesses then becomes critical in predicting subsequent ice shapes.

Mass transport of water over the ice surface also plays an important part which, interacting with the airflow, determines the amount of water locally available for ice accretion and at times, modifies the heat flux experienced by the ice surface. Olsen and Walker [38] first suggested that the role of water transport and large surface water bead formation on the ice is a key mechanism that needs to be incorporated into the physical model for ice accretion. Recent studies of the interaction of the water film with the airflow by Wang and Rothmayer [39, 40] using small scale roughness fields show that rivulets can form due to the interaction with roughness fields. When the film, rivulet or water beads are large, then they are expected to modify the heat flux between the air and the ice surface. However, when the water film is thin the ice accreting beneath the water film experiences the same heat flux as the surface of the water film.

In a recent review of the role of ice feathers in ice accretion, Vargas, Tsao and Rothmayer [4] note that there are several mechanisms which can trigger ice roughness and feather formation. One of them is the instability of the ice surface in cold airstreams, where aerodynamic cooling causes colder roughness peaks to grow faster than warmer roughness troughs, thereby causing roughness elements to grow. The resulting heat flux within the accreted ice increases the growth rate of the peaks and reduces the growth rate of the troughs.

This ice surface instability was shown to be a possible mechanism for ice roughness formation by Tsao and Rothmayer [41, 42, 43, 44] using triple-deck theory. The near-wall Navier Stokes viscous sublayer model of Rothmayer [45] and the modified triple-deck model of Tsao [46] for cross-flow showed that the instabilities could be strongly three-dimensional. However, these ice surface instability studies examined roughnesses with heights smaller than the thickness of the air boundary layer. A subsequent multiple

scales theory for stagnation line icing (Rothmayer [47]) accomodates three-dimensional roughnesses which are the same size as the height of the air boundary layer and also reconciles the inherent time differences between air, water and ice.

The multiple scales theory of Rothmayer [47] is used here as the starting point for a stagnation line stability analysis of glaze ice surfaces with thin water films. The present study focusses on the incipient growth of ice roughness on an initially smooth ice surface for glaze icing conditions. The multiple scales theory for the stagnation line is modified to account for a thin water film, commonly present for realistic amounts of water mass deposition. The multiple scales analysis shows the thin water film to be purely conducting. A linearized stability analysis is formulated which is used to study both stagnation line as well as swept wing attachment line flows. Based on the observations from the multiple scales analysis, an engineering linear stability model is then constructed to predict roughness diameters and smooth zones.

1.1 Organization of the dissertation

This dissertation is divided into four main chapters. Chapter 2 introduces the equations for modeling attachment line icing. Chapter 3 introduces the multiple scales theory for the stagnation line, as well the key concepts for studying the stability of the ice surface. A high Reynolds number analysis is used to investigate the stability of an ice surface lying beneath a low Mach number stagnation-line air flow. Using the Hiemenz flow as the base solution for stagnation line icing problem, the stability characteristics of the ice surface are studied. Chapter 4 extends this model to swept wings. Chapter 5 introduces an approximate engineering model for ice surface stability to study the formation of roughnesses over leading edges of airfoils using a parabola to approximate the airfoil leading edge. A set of flow conditions from icing experiments is chosen to compute the ice surface stability properties. A comparison is made between the pre-

dictions of the ice surface instability and roughness diameters and smooth zone extents from experiments. Reasonable agreement is seen with experiment, and areas required to improve the engineering model are identified.

CHAPTER 2. REVIEW OF EQUATIONS FOR AIRCRAFT ICING

2.1 Introduction

Ice accretion is a coupled multiphase multiscale problem involving the interaction of air, water and ice. To include all the aspects of the ice accretion problem, it is necessary to use a comprehensive set of equations for each phase involved in this process. It is also necessary to consider the conditions at the air/water and water/ice interface boundaries for heat transfer and movement of the interfaces. It should be noted that it is possible to have conditions where there is complete dryout of water over the ice surface, in which case the air and ice come into direct contact. However, these situations will not be considered in this study. In the present study, it is assumed that the air flows over an ice surface which is continuously wetted by a thin water film. This water film is formed by the uniform mass deposition of supercooled water droplets present in the airflow, a model which is commonly used in ice accretion codes. This chapter introduces the dimensional equations for the airflow, the water and the ice as well as the interface boundary conditions. A set of parameters is introduced for non-dimensionalizing these equations, which are then given in the subsequent section. In order to identify the important characteristics of the multiphase problem, a set of perturbation parameters is also introduced in this chapter. A parameter space (see Rothmayer [48]) is briefly discussed which uses several important perturbation parameters to identify different regimes for the aircraft icing problem.

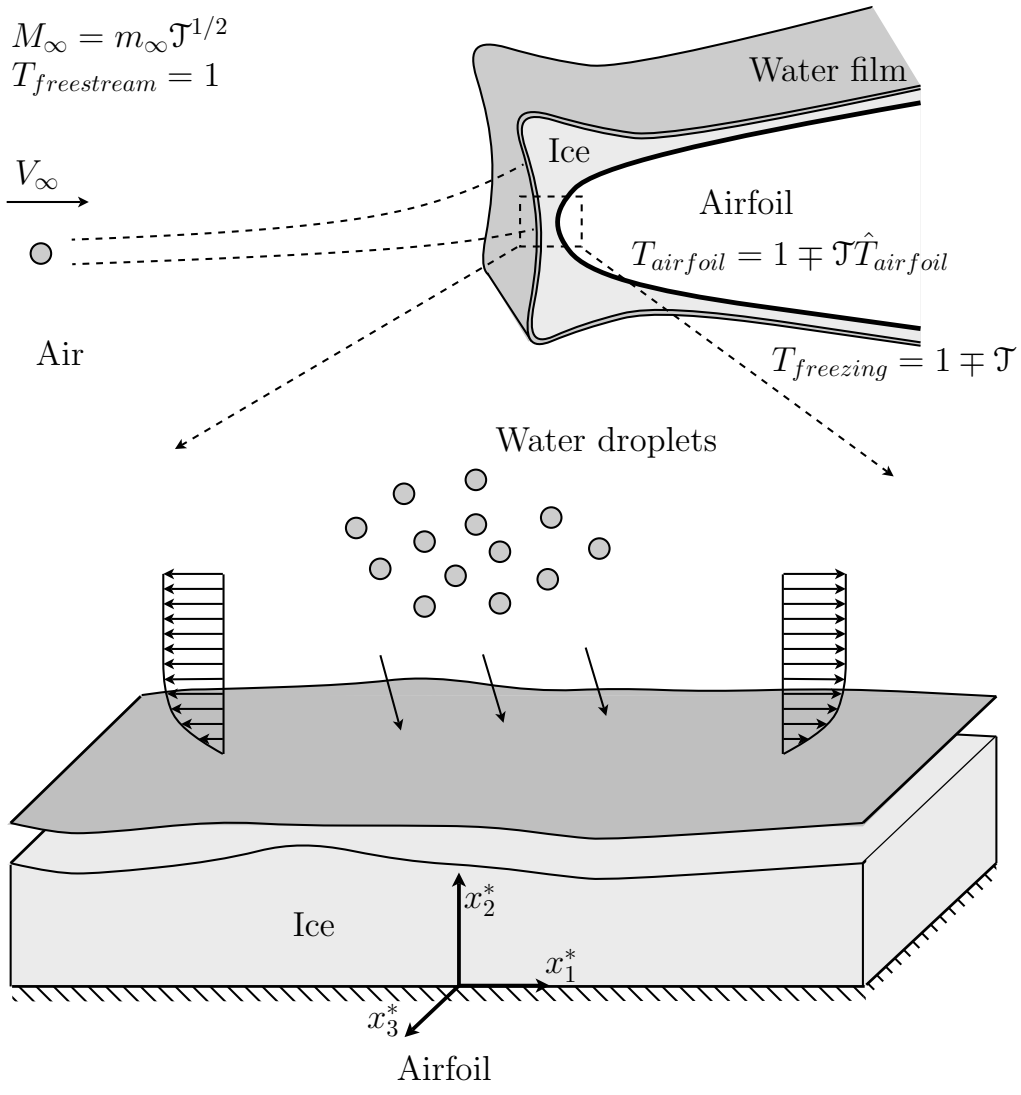

Figure 2.1 Water film and ice surface in the presence of airflow.

2.2 Dimensional equations

The origin of the x_i^* coordinates for each phase is located on the plate/airfoil surface and $(x^*, y^*, z^*) = (x_1^*, x_2^*, x_3^*)$ (see Fig. 2.1). For each phase, suitable coordinate transformations are used later to shift the origin to the interface boundary. Cartesian tensor notation is used below for mass, momentum and energy conservation for compressible airflow, incompressible flow of water and heat conduction within ice (for details, refer to Rothmayer [49]).

Air The mass conservation is written in the form

$$\frac{\partial \rho^*}{\partial t^*} + \frac{\partial}{\partial x_j^*}(\rho^* v_j^*) = 0, \tag{2.1}$$

where (v_1^*, v_2^*, v_3^*) are the velocities in (x_1^*, x_2^*, x_3^*) directions, respectively, and ρ^* is the density of air. The shear stress within the air is written as

$$\tau_{ij}^* = -P^* \delta_{ij} - \frac{2}{3}\mu_{air}^* \frac{\partial v_k^*}{\partial x_k^*}\delta_{ij} + \mu_{air}^* \left(\frac{\partial v_i^*}{\partial x_j^*} + \frac{\partial v_j^*}{\partial x_i^*} \right). \tag{2.2}$$

Here, μ_{air}^* is given by Sutherland's law for the viscosity of air. In most aircraft icing conditions, the temperature changes are small which allows μ_{air}^* to be treated as a constant. The momentum equation then becomes

$$\rho^* \left[\frac{\partial v_i^*}{\partial t^*} + v_j^* \frac{\partial v_i^*}{\partial x_j^*} \right] = \frac{\partial \tau_{ij}^*}{\partial x_i^*}. \tag{2.3}$$

The equation for energy conservation is written as

$$\rho^* c_{v,air}^* \left[\frac{\partial T^*}{\partial t^*} + v_j^* \frac{\partial T^*}{\partial x_j^*} \right] = \tau_{ij}^* \frac{\partial v_i^*}{\partial x_j^*} + \frac{\partial}{\partial x_j^*} \left(k_{air}^* \frac{\partial T^*}{\partial x_j^*} \right). \tag{2.4}$$

where k_{air}^* is given by Sutherland's law for the thermal conductivity of air. In most

aircraft icing conditions, the temperature changes are small which allows k^*_{air} to be treated as a constant as in case of air viscosity μ^*_{air}. The equation of state is written as

$$P^* = \rho^* R T^*. \tag{2.5}$$

Water Water is taken to be incompressible for the conditions of aircraft icing. This implies that the continuity equation reduces to

$$\frac{\partial v^*_j}{\partial x^*_j} = 0. \tag{2.6}$$

The shear stress inside the water is written as

$$\tau^*_{ij} = -P^* \delta_{ij} + \mu^*_{water} \left(\frac{\partial v^*_i}{\partial x^*_j} + \frac{\partial v^*_j}{\partial x^*_i} \right). \tag{2.7}$$

where μ^*_{water} is the viscosity of water and varies significantly with change in temperature. The momentum equations are written as

$$\rho^*_{water} \left[\frac{\partial v^*_i}{\partial t^*} + v^*_j \frac{\partial v^*_i}{\partial x^*_j} \right] = \frac{\partial \tau^*_{ij}}{\partial x^*_i}. \tag{2.8}$$

where ρ^*_{water} is taken to be constant. The equation for energy conservation is written as

$$\rho^*_{water} c^*_{water} \left[\frac{\partial T^*}{\partial t^*} + v^*_j \frac{\partial T^*}{\partial x^*_j} \right] = \tau^*_{ij} \frac{\partial v^*_i}{\partial x^*_j} + \frac{\partial}{\partial x^*_j} \left(k^*_{water} \frac{\partial T^*}{\partial x^*_j} \right). \tag{2.9}$$

Air/water interface The conditions at the air/water interface include a stress match between the two phases, air and water, the mass deposited due to the impact of the supercooled water droplets and a kinematic condition describing the evolution of the water film, where f^*_{water} is the water film height. Including the surface tension of water, the stress match at the air/water interface is written as

$$\left[\tau_{ij}^*\right]_{water} n_j^* = \left[\tau_{ij}^*\right]_{air} n_j^* - \sigma^* \kappa_{water}^* n_i^*, \tag{2.10}$$

where the curvature of the water film for single valued surfaces is given by

$$\kappa_{water}^* = -\frac{\partial^2 f_{water}^*}{\partial x_1^{*2}} \left[1 + \left(\frac{\partial f_{water}^*}{\partial x_1^*}\right)^2\right]^{-3/2} - \frac{\partial^2 f_{water}^*}{\partial x_3^{*2}} \left[1 + \left(\frac{\partial f_{water}^*}{\partial x_3^*}\right)^2\right]^{-3/2}, \tag{2.11}$$

and the surface normals for single valued surfaces are

$$(n_1^*, n_2^*, n_3^*) = \left(-\frac{\partial f_{water}^*}{\partial x_1^*}, 1, -\frac{\partial f_{water}^*}{\partial x_3^*}\right) \left[\left(\frac{\partial f_{water}^*}{\partial x_1^*}\right)^2 + 1 + \left(\frac{\partial f_{water}^*}{\partial x_3^*}\right)^2\right]^{-1/2}. \tag{2.12}$$

In subsequent discussions, all surfaces are taken to be single valued with respect to the coordinate axes. The accumulation of water droplets is modeled by a uniform deposition of mass onto the surface. This uniform mass deposition model is also used to estimate the transfer of the kinetic energy from the droplets to the water film which is included in the heat flux balance at the air/water interface. The increase in the water film height due to the deposition of the water droplets is given by (see Appendix C)

$$\begin{aligned}\frac{d\delta_{water}^*}{dt^*} = \frac{LWC_s^*}{\rho_{water}^*} &\left[v_{1,d}^* \frac{\partial f_{water}^*}{\partial x_1^*} + v_{3,d}^* \frac{\partial f_{water}^*}{\partial x_3^*} + \left|v_{2,d}^*\right|\right] \\ &\times \left[\left(\frac{\partial f_{water}^*}{\partial x_1^*}\right)^2 + 1 + \left(\frac{\partial f_{water}^*}{\partial x_3^*}\right)^2\right]^{-1/2},\end{aligned} \tag{2.13}$$

where $(v_{1,d}^*,\ v_{2,d}^*,\ v_{3,d}^*)$ are the velocities of the droplets in the respective coordinate directions. LWC_s^* is the liquid water content in the airflow at the surface. Since the droplets are seen as coming onto the surface, the velocities as well as the surface normals are pointed into the surface (see Fig. C.1). Similarly, including the heat transfer due to droplet impacts, the heat transfer between air and water is given by

$$k_{air}^* \left[\frac{\partial T^*}{\partial x_j^*}\right]_{air} n_j^* = k_{water}^* \left[\frac{\partial T^*}{\partial x_j^*}\right]_{water} n_j^* + (\rho c)_{water}^* \left[T_{water}^* - T_{impact}^*\right] \frac{d\delta_{water}^*}{dt}, \tag{2.14}$$

where $T^*_{impact} = T^*_{drops} + V^*_{i,drop}V^*_{i,drop}/(2c^*_{water})$. Here, the surface normals are directed in the usual direction of the coordinate system and are given by Eq. 2.12 (see Fig C.2) (For details on the heat transfer balance and the kinematic condition at the ice/water interface, see Appendix C).

Ice The heat conduction equation within ice is given by

$$\rho^*_{ice}c^*_{ice}\frac{\partial T^*}{\partial t^*} = \frac{\partial}{\partial x^*_k}\left[k^*_{ice}\frac{\partial T^*}{\partial x^*_k}\right]. \tag{2.15}$$

The freezing/melting water/ice interface imposes a boundary condition which holds the ice surface at the freezing temperature of water. The temperature at the airfoil surface imposes another boundary condition on Eq. 2.15 which is not as well-defined.

Water/ice interface In solidification problems, there is an inherent morphological instability of the interface. Undercooling leads to a growing instability. The effect of undercooling combines with a surface curvature dependent change in the freezing temperature of ice, called the Gibbs-Thompson effect (see Davis [50] and Gupta [51]), which is given by

$$T^*_{water} = T^*_{ice} = T^*_{freezing}\left(1 - \frac{\gamma^*_{ice/water}}{\rho^*_{ice}H^*_{ice/water}}\kappa^*_{ice}\right), \tag{2.16}$$

where the surface curvature of the ice surface is

$$\kappa^*_{ice} = -\frac{\partial^2 f^*_{ice}}{\partial x^*_1 \partial x^*_1}\left[1 + \left(\frac{\partial f^*_{ice}}{\partial x^*_1}\right)^2\right]^{-3/2} - \frac{\partial^2 f^*_{ice}}{\partial x^*_3 \partial x^*_3}\left[1 + \left(\frac{\partial f^*_{ice}}{\partial x^*_3}\right)^2\right]^{-3/2}. \tag{2.17}$$

Here, the ice surface, denoted by f^*_{ice}, is single valued. A Stefan condition gives the growth of the ice surface, based on the difference in the heat flux from the water and

ice i.e.

$$k^*_{water}\left[\frac{\partial T^*}{\partial x^*_j}\right]_{water} n^*_j = k^*_{ice}\left[\frac{\partial T^*}{\partial x^*_j}\right]_{ice} n^*_j - L^*_{water/ice}\rho^*_{ice}\frac{d\delta^*_{ice}}{dt^*}, \tag{2.18}$$

where $L^*_{water/ice}$ is the latent heat of fusion of water. The kinematic condition for the ice surface is given by

$$n^*_2\frac{\rho^*_{water}}{\rho^*_{ice}}\frac{d\delta^*_{ice}}{dt^*} = \frac{df^*_{ice}}{dt^*} + n^*_1\frac{\rho^*_{water}}{\rho^*_{ice}}\frac{df^*_{ice}}{dx^*_1}\frac{d\delta^*_{ice}}{dt^*} + n^*_3\frac{\rho^*_{water}}{\rho^*_{ice}}\frac{df^*_{ice}}{dx^*_3}\frac{d\delta^*_{ice}}{dt^*}, \tag{2.19}$$

where the ice surface normals are

$$(n^*_1, n^*_2, n^*_3) = \left(\frac{\partial f^*_{ice}}{\partial x^*_1}, -1, \frac{\partial f^*_{ice}}{\partial x^*_3}\right)\left[\left(\frac{\partial f^*_{ice}}{\partial x^*_1}\right)^2 + 1 + \left(\frac{\partial f^*_{ice}}{\partial x^*_3}\right)^2\right]^{-1/2}. \tag{2.20}$$

(For details on the Stefan condition and the kinematic condition at the ice/water interface, see Appendix C)

2.3 Non-dimensionalization

The equations for air, water and ice are non-dimensionalized using the free-stream conditions in the airflow. The velocities are non-dimensionalized using $v^*_i = V_\infty v_i$ where V_∞ is the freestream velocity in the airflow. The spatial coordinates are non-dimensionalized using $x^*_i = x_i L$ where L is a characteristic length such as the chord length of an airfoil or it's nose radius of curvature. Pressure is written as $P^* = P_\infty + \rho_\infty V^2_\infty P$. The Reynolds number and the Mach number are given by $Re = \rho_\infty V_\infty L/\mu_\infty$ and $M_\infty = V_\infty/a_\infty$ respectively, where $a_\infty = \sqrt{\gamma R T_\infty}$ is the speed of sound in the air freestream. Also, the Prandtl number is $\Pr = c^*_{p,air}\mu^*_{air}/k^*_{air} = 0.7$, and the ratio of specific heats is $\gamma = c^*_{p,air}/c^*_{v,air} = 1.4$. To handle the different phases, the ratios of various dimensional constants in these phases are introduced. The ratios of air/water density

and ice/water density are written as $D_{aw} = \rho_\infty/\rho^*_{water}$ and $D_{iw} = \rho^*_{ice}/\rho^*_{water}$, respectively. The ratio of viscosity in air and water is given by $M = \mu^*_{water}(T_\infty)/\mu_\infty$. Similarly, the ratios of specific heat in air/water and air/ice are given by $C_{aw} = c^*_{p,air}/c^*_{p,water}$ and $C_{ai} = c^*_{p,air}/c^*_{ice}$. The thermal conductivity ratios are evaluated at the reference temperature of the free-stream i.e. $K_{wa} = k^*_{water}/k^*_{air}$ and $K_{iw} = k^*_{ice}/k^*_{water}$. Again using the free-stream temperature, non-dimensional water and ice thermal conductivities are written as $k_{water}(T) = k^*_{water}/k^*_{water}(T_\infty)$ and $k_{ice}(T) = k^*_{ice}/k^*_{ice}(T_\infty)$ respectively. The ice surface is held at freezing temperature of water given by $T_{freezing} = T^*_{freezing}/T_\infty$. A surface tension parameter is defined by $\sigma = \sigma^*/(\mu_\infty V_\infty)$, where σ^* is the surface tension of water. A non-dimensional Gibbs-Thomson parameter is introduced as $\varepsilon = \gamma^*_{g,ice/water}/(\rho^*_{ice} H^*_{ice/water} L)$. A Stefan number is introduced for the non-dimensional rate of growth of the ice surface and is given by $Ste = c^*_{ice} T_\infty / L^*_{water/ice}$. Using these parameters, the governing equations for airflow, water and ice are rewritten below in non-dimensional form.

2.4 Non-dimensional equations

Air After non-dimensionalization, the continuity equation becomes

$$\frac{\partial \rho}{\partial t} + \frac{\partial}{\partial x_j}(\rho v_j) = 0, \tag{2.21}$$

Using the expression for the shear stress, the momentum equation is obtained as

$$\begin{aligned}\rho\left[\frac{\partial v_i}{\partial t} + v_j\frac{\partial v_i}{\partial x_j}\right] = &-\frac{\partial P}{\partial x_i} - \frac{2}{3}Re^{-1}\frac{\partial}{\partial x_i}\left(\mu_{air}\frac{\partial v_k}{\partial x_k}\right)\\ &+Re^{-1}\frac{\partial}{\partial x_j}\left[\mu_{air}\left(\frac{\partial v_i}{\partial x_j} + \frac{\partial v_j}{\partial x_i}\right)\right].\end{aligned} \tag{2.22}$$

The energy equation becomes

$$\rho\left[\frac{\partial T}{\partial t}+v_j\frac{\partial T}{\partial x_j}\right]=-(\gamma-1)\rho T\frac{\partial v_k}{\partial x_k}-\frac{2}{3}\gamma(\gamma-1)M_\infty^2Re^{-1}\mu_{air}\frac{\partial v_k}{\partial x_k}\frac{\partial v_m}{\partial x_m}$$
$$+\gamma(\gamma-1)M_\infty^2Re^{-1}\mu_{air}\frac{\partial v_i}{\partial x_j}\left(\frac{\partial v_i}{\partial x_j}+\frac{\partial v_j}{\partial x_i}\right)+Re^{-1}\frac{\partial}{\partial x_j}\left(\frac{\gamma\mu_{air}}{\mathrm{Pr}}\frac{\partial T}{\partial x_j}\right), \tag{2.23}$$

where Pr is the Prandtl number defined earlier, and $\mu_{air}=\mu^*_{air}/\mu_\infty$. The equation of state is the non-dimensional ideal gas law, given by

$$1+\gamma M_\infty^2P=\rho T. \tag{2.24}$$

Water The mass conservation inside water is given by the continuity equation,

$$\frac{\partial v_j}{\partial x_j}=0. \tag{2.25}$$

The non-dimensional momentum equation is obtained as

$$\frac{\partial v_i}{\partial t}+v_j\frac{\partial v_i}{\partial x_j}=-D_{aw}\frac{\partial P}{\partial x_i}+\frac{1}{Re}MD_{aw}\frac{\partial}{\partial x_j}\left[\mu_{water}\left(\frac{\partial v_i}{\partial x_j}+\frac{\partial v_j}{\partial x_i}\right)\right], \tag{2.26}$$

and the energy equation becomes

$$\frac{\partial T}{\partial t}+v_j\frac{\partial T}{\partial x_j}=(\gamma-1)\frac{1}{Re}D_{aw}C_{aw}\mu_{water}MM_\infty^2\frac{\partial v_i}{\partial x_j}\left(\frac{\partial v_i}{\partial x_j}+\frac{\partial v_j}{\partial x_i}\right)$$
$$+D_{aw}C_{aw}Re^{-1}\frac{\partial}{\partial x_j}\left(\frac{\mu_{air}K_{wa}}{\mathrm{Pr}}\frac{\partial T}{\partial x_j}\right). \tag{2.27}$$

Air/water interface The expressions for the shear stress inside airflow and water are used to rewrite the non-dimensional equation for stress balance, which becomes

$$\left[-P\delta_{ij} + Re^{-1}M\mu_{water}\left(\frac{\partial v_i}{\partial x_j} + \frac{\partial v_j}{\partial x_i}\right)\right]_{water} n_j = \left[-P\delta_{ij} - \frac{2}{3}Re^{-1}\mu_{air}\frac{\partial v_k}{\partial x_k}\delta_{ij} + Re^{-1}\mu_{air}\left(\frac{\partial v_i}{\partial x_j} + \frac{\partial v_j}{\partial x_i}\right)\right]_{air} n_j - Re^{-1}\sigma\kappa_{water}n_i, \quad (2.28)$$

where the curvature of the water surface is given by

$$\kappa_{water} = -\frac{\partial^2 f_{water}}{\partial x_1 \partial x_1}\left[1 + \left(\frac{\partial f_{water}}{\partial x_1}\right)^2\right]^{-3/2} - \frac{\partial^2 f_{water}}{\partial x_3 \partial x_3}\left[1 + \left(\frac{\partial f_{water}}{\partial x_3}\right)^2\right]^{-3/2},$$

and the water surface normals are

$$(n_1, n_2, n_3) = \left(-\frac{\partial f_{water}}{\partial x_1}, 1, -\frac{\partial f_{water}}{\partial x_3}\right)\left[\left(\frac{\partial f_{water}}{\partial x_1}\right)^2 + 1 + \left(\frac{\partial f_{water}}{\partial x_3}\right)^2\right]^{-1/2}.$$

The uniform mass deposition of water onto the ice surface gives

$$\frac{d\delta_{water}}{dt} = LWC_s\left[v_{1,d}\frac{\partial f_{water}}{\partial x_1} + v_{3,d}\frac{\partial f_{water}}{\partial x_3} + |v_{2,d}|\right] \times \left[\left(\frac{\partial f_{water}}{\partial x_1}\right)^2 + 1 + \left(\frac{\partial f_{water}}{\partial x_3}\right)^2\right]^{-1/2}, \quad (2.29)$$

where $LWC_s = LWC_s/\rho^*_{water}$. The heat transfer balance at the air/water interface yields

$$\left[\frac{\partial T}{\partial x_j}\right]_{air} n_j = K_{wa}\left[\frac{\partial T}{\partial x_j}\right]_{water} n_j + \frac{Re\,\mathrm{Pr}\,[T_{water} - T_{impact}]}{D_{aw}C_{aw}\mu_{air}}\frac{d\delta_{water}}{dt}, \quad (2.30)$$

where $T_{impact} = T_{drops} + (\gamma - 1)C_{aw}M^2_\infty V_{i,drop}V_{i,drop}/2$.

Ice The equation for heat conduction within the ice is rewritten as

$$\frac{\partial T}{\partial t} = Re^{-1}\frac{D_{aw}}{D_{iw}}C_{ai}\frac{\partial}{\partial x_k}\left[\frac{\mu_{air}}{\mathrm{Pr}}K_{wa}\frac{k_{ice}}{k_{water}}K_{iw}\frac{\partial T}{\partial x_k}\right]. \tag{2.31}$$

The upper ice surface at the water/ice interface is held at the freezing temperature of water. Ice at the airfoil surface is influenced by heat conduction within the airfoil surface. For now, the airfoil is assumed to be at a constant known temperature.

Water/Ice interface In non-dimensional form, the Gibbs-Thomson effect dictating the temperature at the ice/water interface is given by

$$T_{water} = T_{ice} = T_{freezing}\left(1 - \varepsilon\kappa_{ice}\right), \tag{2.32}$$

where the ice surface curvature is

$$\kappa_{ice} = -\frac{\partial^2 f_{ice}}{\partial x_1 \partial x_1}\left[1+\left(\frac{\partial f_{ice}}{\partial x_1}\right)^2\right]^{-3/2} - \frac{\partial^2 f_{ice}}{\partial x_3 \partial x_3}\left[1+\left(\frac{\partial f_{ice}}{\partial x_3}\right)^2\right]^{-3/2}. \tag{2.33}$$

The Stefan condition for the growth of the ice surface is given by

$$\left[\frac{\partial T}{\partial x_j}\right]_{water} n_j = \frac{k_{ice}K_{iw}}{k_{water}}\left[\frac{\partial T}{\partial x_j}\right]_{ice} n_j - \frac{\mathrm{Pr}}{\mu_{air}}\frac{1}{K_{wa}C_{ai}}\frac{Re}{D_{aw}Ste}\frac{d\delta_{ice}}{dt}. \tag{2.34}$$

The kinematic condition for the ice surface is found to be

$$n_2\frac{d\delta_{ice}}{dt} = D_{iw}\frac{df_{ice}}{dt} + n_1\frac{df_{ice}}{dx_1}\frac{d\delta_{ice}}{dt} + n_3\frac{df_{ice}}{dx_3}\frac{d\delta_{ice}}{dt}, \tag{2.35}$$

where the surface normals of the ice surface are

$$(n_1, n_2, n_3) = \left(-\frac{\partial f_{water}}{\partial x_1}, 1, -\frac{\partial f_{water}}{\partial x_3}\right)\left[\left(\frac{\partial f_{water}}{\partial x_1}\right)^2 + 1 + \left(\frac{\partial f_{water}}{\partial x_3}\right)^2\right]^{-1/2}.$$

2.5 Perturbation parameters

Among the various non-dimensional parameters introduced in the equations, it becomes necessary to identify the important parameters which determine the nature of the governing equations in each phase. For example, in the air it is assumed that

$$Re = \frac{\rho_\infty V_\infty L}{\mu_\infty} \gg 1, \qquad M_\infty = \frac{V_\infty}{a_\infty} \ll 1.$$

The low Mach number limit is selected to be consistent with a small temperature perturbation between the free-stream and the ice surface, which is defined to be

$$\mathcal{T} = |\Delta T^*|/T^*_{freezing} \ll 1.$$

Here, the non-dimensional freezing temperature on the ice surface is $T_{freezing} = T^*_{freezing}/T_\infty = [1 - \Delta T^*/T^*_{freezing}]^{-1}$ where $\Delta T^* = T^*_{freezing} - T_\infty$. The liquid water content (LWC) is the mass of supercooled water droplets present in air and is usually on the order of 0.5 g/m^3, non-dimensionalised by the water density. Similarly, the parameters related to the water film are taken to be

$$M = \frac{\mu^*_{water}(T_\infty)}{\mu_\infty} \gg 1, \quad LWC = \frac{LWC^*}{\rho^*_{water}} \ll 1.$$

The following relationship is assumed by Rothmayer [47] in order to obtain a least degenerate shear stress and heat flux balance at the air/water interface for situations giving a strong interaction between the three media:

$$(M, K_{wa}) = (\mathcal{M}, \mathcal{K}) D_{aw}^{-1/2} \gg 1, \tag{2.36}$$

where $\mathcal{M}$ and $\mathcal{K}$ are termed the film inertia parameters. For aircraft icing applications, $\mathcal{M}$ and $\mathcal{K}$ typically range between 1 and 5 (see Rothmayer [48]). These parameters are then used to identify the key length scales, time scales and velocity scales which influence the evolution of the airflow, the water film and the ice surface. Other ratios, such as $K_{iw} = k^*_{ice}/k^*_{water}$, remain almost constant for the same conditions. The subsequent section outlines a parameter space which identifies the typical behavior of the multiphase problem of ice growth with respect to the effect of heat transfer from airflow, ice height and droplet impacts etc.

2.6 Parameter space

A low Mach number Prandtl boundary layer theory for aircraft icing has been developed by Rothmayer [48]. This model focuses on the water film transport, the role of droplet distributions and the formation of ice structures wetted by thin water films. Some effects such as evaporation, sublimation and condensation are not being considered in this model. The aircraft icing problem is considered as shown in Fig 2.1. This section summarises the key features of this parameter space. The rationale for most of the scales from Fig. 2.2 will be discussed in subsequent sections. The path of water droplets coming onto the surface of the wing is affected by the airflow. The local mass accumulation of water due to these droplets along with the shear stress of the airflow which drives the water mass along the ice surface determines the thickness of the water film. The ice surface is assumed to be at the freezing temperature of water. The temperature of the airfoil surface and the heat conduction within the accumulating ice as well as the heat flux from the water film influence further growth of the ice surface. In order to illustrate the relative importance of the various effects, such as heat flux from airflow, heat conduction within water and ice, a parameter space is constructed for the boundary layer theory (see Rothmayer [48]). In Fig. 2.2, key effects of air heat flux (as

dictated by the ambient air temperature $\mathcal{T}$), liquid water content (LWC) and ice height (f_{ice}) are used to identify different regimes for ice growth. When the rate of water mass being deposited is less than the rate of the ice growth then rime ice is obtained, and this happens when f_{ice} is small in Fig. 2.2. In addition, early phases of ice accretion are strongly influenced by the heat conduction within ice (i.e. from the airfoil surface). After thicker ice sheets form, the ice tends to insulate the water/ice interface from the airfoil. The heat flux due to droplet impacts also affects the ice growth when the liquid water content becomes large. The heat flux from the airflow is dictated by the air temperature perturbation, $\mathcal{T}$. After considering the non-dimensional Navier-Stokes equations given in the previous section, it is found that the heat flux from airflow and the heat flux due to water droplet impacts are in balance when $LWC \sim \mathcal{O}(Re^{-1/2}D_{aw})$ (see Rothmayer [48]). The insulating effect of the ice height is first achieved when $f_{ice} \sim \mathcal{O}(Re^{-1/2}D_{aw}^{-1/2})$ for $LWC \ll Re^{-1/2}D_{aw}$ and $f_{ice} \sim \mathcal{O}(LWC^{-1}Re^{-1}D_{aw}^{1/2})$ for $LWC \gg Re^{-1/2}D_{aw}$ (again, see Rothmayer [48]). For all ice thicknesses, when the rate of water mass deposition is less the rate of the ice growth (i.e. when $LWC \ll Re^{-1/2}D_{aw}\mathcal{T}$), rime ice is formed. This is called the Ludlam limit. For the current study, the temperature perturbation, $\mathcal{T}$, the liquid water content, LWC, and the ice height, f_{ice}, are chosen such that the heat flux from air and droplet impacts are in balance and the ice height is at the boundary where ice first begins to have an insulating effect, i.e. $f_{ice} \sim \mathcal{O}(Re^{-1/2}D_{aw}^{-1/2})$ and at location ($\bigcirc$) in Fig. 2.2. It should be noted that another position in the parameter space (highlighted by $\square$) is used for the multiple scales stagnation line theory of Rothmayer [47]. However, aircraft icing conditions with realistic amounts of water mass deposition used in this study are located at ($\bigcirc$) in Fig. 2.2 when the ice is uniformly wetted by a thin water film.

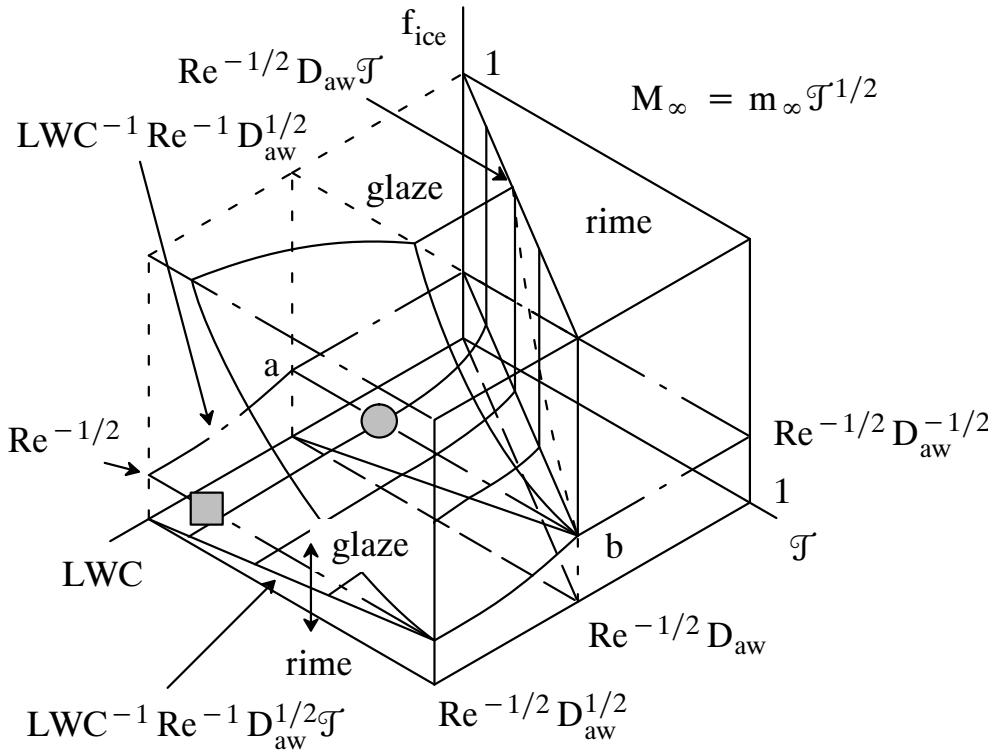

Figure 2.2 Parameter space for aircraft icing : the heat flux from the airflow is determined by the temperature perturbation $\mathcal{T}$, the ice thickness f_{ice} dictates the heat flux within ice and LWC determines the mass of water mass deposited onto the ice surface (which sets the water film thickness). Lack of sufficient water in case of increased cooling leads to rime ice and glaze ice forms when the ice surface is saturated with water.

CHAPTER 3. INSTABILITY OF STAGNATION LINE ICING

3.1 Key factors influencing roughness formation

Phase change and solidification often involves interfacial instabilities. This is seen in metal solidification as well as formation of snow flakes. The role of this interfacial instability for an ice surface is being studied to predict natural ice roughness formation. For aircraft icing, ice roughness formation is influenced by three main effects, namely the air heat flux, the ice height (which effects the ice heat flux) and the local changes in the freezing temperature of water due to curvature effects. If the air temperature is lower than the freezing temperature of water, a local increase in ice height leads to more cooling from the airflow which causes the ice to freeze faster. (see Fig 3.1). When the air temperature is greater than the freezing temperature of water, a local increase in ice height leads to more heating from from the airflow which causes the ice to melt more quickly. Usually, an airfoil in a cold airstream will be at a temperature lower than the freezing temperature of water. Strong heat conduction within the ice due to the thinness of the ice sheet stabilizes the ice surface. As the ice height increases, the stabilizing effect of the heat flux within the ice decreases. In addition to the role of the heat transfer within air and ice, local changes occur in the freezing temperature of the ice surface due to surface curvature, called the Gibbs-Thomson effect. A local growth in the ice surface leads to a larger positive curvature of the ice surface, which, in turn, lowers the local freezing temperature of water (see Eq. 2.32 in Section 2.4 and Fig. 3.2). This change in

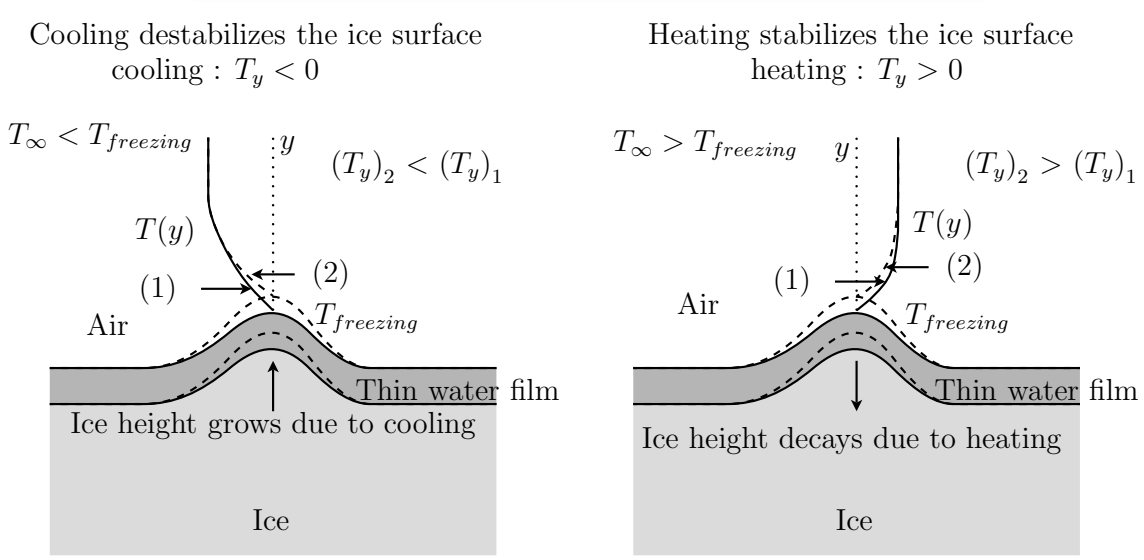

Figure 3.1 Effect of the heat flux from the airflow over the ice surface.

the freezing temperature of water leads to a weaker heat flux within ice which causes the local ice height to grow more slowly (see Fig 3.2). A local depression in the ice surface leads to a larger negative curvature of the ice surface, which increases the local freezing temperature of water. This produces a temperature on the ice surface which is further from the cold airfoil temperature and leads to a stronger local heat flux within the ice, which causes the local ice height to grow more rapidly. In general, the Gibbs-Thomson effect stabilizes the ice surface on sufficiently small scales. A combination of the effects mentioned above influence the typical shapes and wavelengths of the disturbances which lead to the formation of ice roughnesses.

3.2 Overview of the stagnation icing problem

The ice accretion near the stagnation line shows numerous interesting features such as roughness elements (see Fig. 3.3), a smooth zone beyond which these roughness elements form, and large water beads. These roughness elements and water beads are

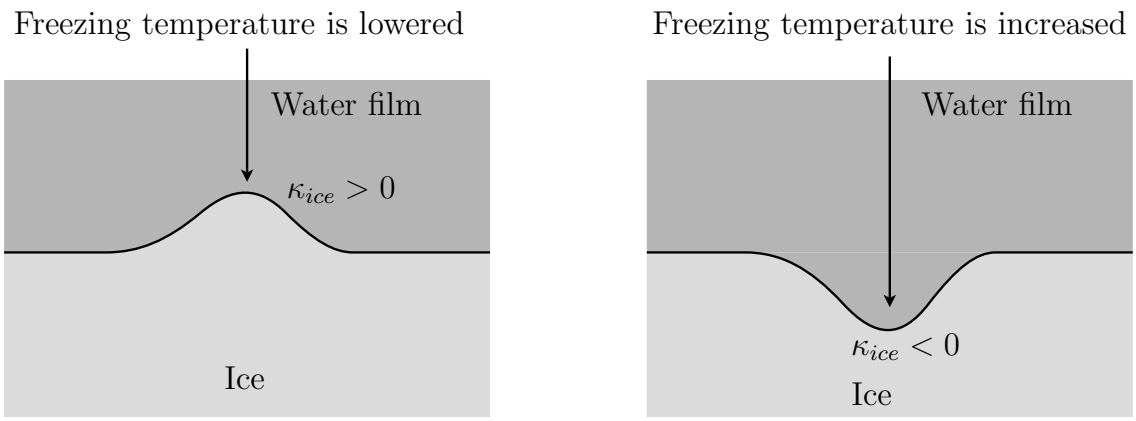

Figure 3.2 Effect of the Gibbs-Thomson effect on the local freezing temperature of the ice surface.

often on the scale of the boundary layer height, in the sense that their diameters and heights are approximately the same as the boundary layer thickness. Recent studies have linked the large complex structures found in the later stages of ice accretion to these roughness elements. Previous computations of ice roughness formation via ice surface instabilities have all looked at roughness height scales smaller than the boundary layer height on a single time scale, namely the ice growth time scale. However, the airflow, the water film and the ice all experience distinctly different time scales. In order to resolve these issues, Rothmayer [47] proposed a multiple scales approach which incorporates the interaction between all the three phases (at point □ in Fig. 2.2). Air, water and ice are all considered to have length scales of $\mathcal{O}(Re^{-1/2})$ in all spatial dimensions. The airflow experiences the fastest time scale followed by the water film and then the ice surface evolution. The averaged effect of the shear stress and the heat transfer of the airflow is transmitted into the water film. The water film is a full viscous Navier-Stokes problem. The heat transfer through the water film is averaged on the water time scale and that heat flux drives the ice growth. The interaction between the water film and

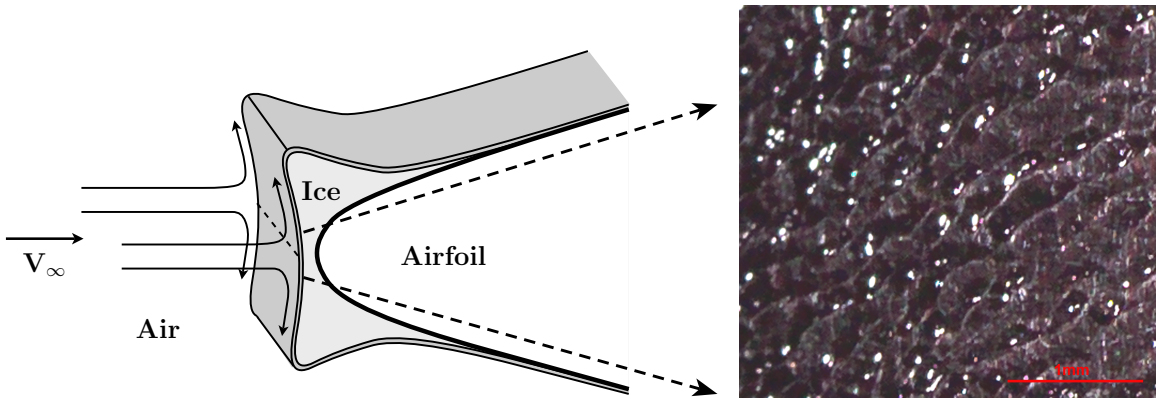

Figure 3.3 (a) Simplified ice surface on an airfoil. (b) Early roughness formation of the ice surface near a stagnation line (see Vargas and Tsao [2], provided by Vargas and reproduced with permission).

the airflow leads to changes in the heat flux experienced by the ice surface underneath the water film, which changes the rate of growth of the ice surface. This model allows for the inclusion of roughness elements on the scale of the air boundary layer thickness. Since the roughness element sizes commonly seen in icing experiments have dimensions which are close to the boundary layer thickness, this model is suitable for studying ice roughness formation. However, for realistic amounts of water mass deposition onto the ice surface, the water film thickness is smaller than the $\mathcal{O}(Re^{-1/2})$ thickness assumed by Rothmayer [47] (see Fig. 2.2). Hence, it is necessary to modify the model of Rothmayer [47] for the thin water film experienced in most conditions of aircraft icing (at point ◯ in Fig. 2.2).

3.3 Assumptions and scalings for stagnation line icing

The ice surface on the wing is idealized as a flat surface close to the stagnation line. It is assumed that this ice surface is uniformly covered by a thin water film. The ice surface has a temperature $T^*_{freezing} = 273.15\,\mathrm{K}$. The airflow is considered to be a

compressible high-Reynolds number and low Mach number limit where the Reynolds number and Mach number of the flow are defined in Section 2.5. It is found that the viscous effects due to Mach number heating become important when

$$M_\infty = m_\infty \mathcal{T}^{1/2}. \tag{3.1}$$

At low Mach numbers, the airflow becomes incompressible at leading order, with a stagnation flow boundary layer in air of height $\mathcal{O}(Re^{-1/2})$. The key perturbation parameters for the present problem are Re, $\mathcal{T}$ and D_{aw}. The water film thickness is small and this results in the water-film related parameters such as M and σ not being needed in the final formulation for the stability analysis.

3.4 Expansions for stagnation line icing

Air In order to estimate the relative magnitude of flow variables in the airflow and the water as well as the temperature in ice, it is necessary to use the perturbation parameters along with the non-dimensional equations in Section 2.4. In a typical boundary layer over an airfoil, the boundary layer height is $y \sim Re^{-1/2}$. The streamwise distance is $x \sim 1$. However, near the stagnation region, $x \ll 1$ and $x \sim y$, which gives $x \sim Re^{-1/2}$. Considering the continuity equation in the airflow (Eq. 2.21), it is seen that

$$\begin{aligned} u \sim x, \qquad & v \sim y, \\ \Rightarrow u \sim Re^{-1/2}, \qquad & v \sim Re^{-1/2}. \end{aligned}$$

From the x-momentum equation, a balance between the pressure and the convective terms yields

$$\frac{u^2}{x} \sim \frac{P}{x}, \qquad \Rightarrow P \sim u^2 \sim Re^{-1}.$$

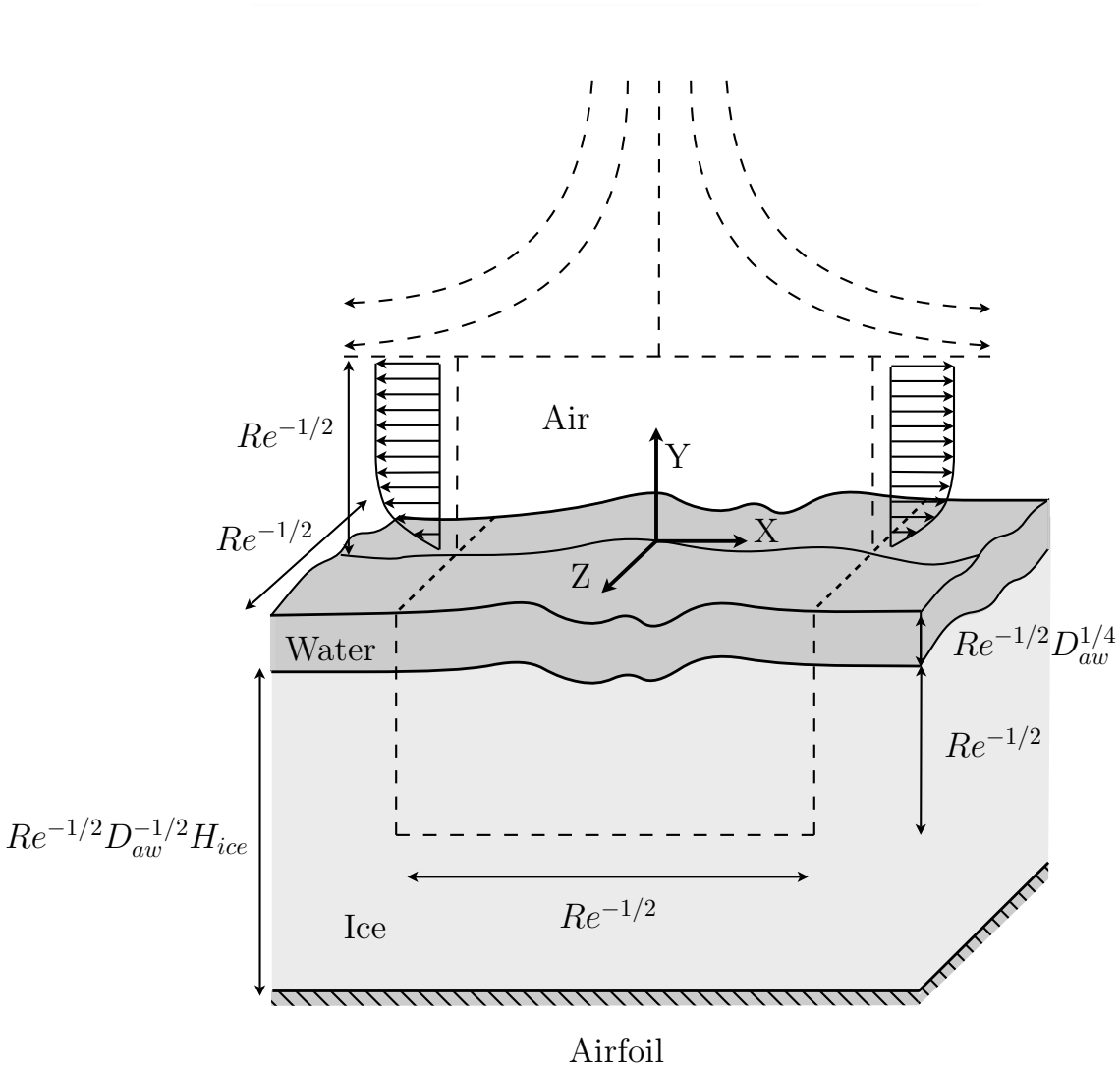

Figure 3.4 Scales and geometry of the thin-film stagnation line icing problem (at point ◯ in Fig 2.2). Shown here for shallow ice roughness. Note that in the nonlinear stagnation line problem, the ice surface height is the size of the boundary layer, i.e. $f_{ice} \sim Re^{-1/2}F_{ice}$.

The free-stream temperature is considered to be close to the freezing temperature of water. Hence, the temperature within the airflow is expressed in terms of a small perturbation $\mathcal{T}$ given in Section 2.5. Using Eq. 3.1, the non-dimensional ideal gas relation (Eq. 2.24) gives

$$\rho \sim \mathcal{T}.$$

The spanwise direction is also taken to be $z \sim Re^{-1/2}$. Hence, the spanwise velocity is $w \sim Re^{-1/2}$.

The Stefan condition for the ice growth is initially dominated by the heat flux within the ice. As the ice accretion progresses, the heat flux from the airflow and the heat flux within the water film come to influence the ice growth. This happens when $f_{ice} \sim Re^{-1/2} D_{aw}^{-1/2}$ ($\bigcirc$ in Fig. 2.2). The rationale for this selection of ice thickness is discussed later. Below this ice thickness, the heat flux from the cold airfoil dominates the ice growth. Above this thickness, the ice insulates the surface of the ice from the airfoil beneath it (see Rothmayer [48, 47] and Otta and Rothmayer [52]). Hence, the leading order ice height is given by $Re^{-1/2} D_{aw}^{-1/2} H_{ice}$ for the stagnation line shown in Fig. 3.4.

Summarizing, the length scales and the velocities in air are given by

$$t = \tau_1, \quad (x, y, z) = (0, Re^{-1/2} D_{aw}^{-1/2} H_{ice}, 0) + Re^{-1/2}(X, Y, Z),$$
$$(u, v, w) \sim Re^{-1/2}(U, V, W) + Re^{-1/2}\mathcal{T}(\hat{U}, \hat{V}, \hat{W}) + \dots ,$$

and the expansions for pressure, density and temperature are

$$p \sim p_0 + Re^{-1} P + \dots \quad , \qquad (\rho, T) \sim 1 + \mathcal{T}(R, \hat{T}) + \dots .$$

Notice that the air has constant density and temperature at leading order, which lead

to incompressible equations in air.

Water The water film is formed by a uniform deposition of water from the droplets impacting the ice surface (see Gent *et al* [9] and Rothmayer [48]). A brief review of some of these scaling arguments is given below. Using two-dimensional order of magnitude estimates and assuming $\mathcal{O}(1)$ velocity of the impacting water droplets, equating the impacting water mass flux to the mass flux inside the water film in kg/s gives

$$LWC^* V_d^* (dx^* dz^*) \sim \mathcal{O}\left((\rho^*_{water} u^*_{water} (dz^* h^*_{film}) \right),$$

which yields, upon non-dimensionalization and using a unit depth in the spanwise direction,

$$LWC V_d dx \sim \mathcal{O}\left(u_{water} h_{film} \right). \tag{3.2}$$

Here, $LWC = LWC^*/\rho^*_{water}$ is the non-dimensional liquid water content defined earlier in Section 2.4, and in the stagnation region, $dx \sim \mathcal{O}(Re^{-1/2})$. From a balance of the shear stress at the air/water interface,

$$\mu^*_{water} \left[\frac{\partial u^*}{\partial y^*} \right]_{water} = \mu^*_{air} \left[\frac{\partial u^*}{\partial y^*} \right]_{air} \quad \Rightarrow u^*_{water} \sim \mathcal{O}\left(\frac{\mu^*_{air}}{\mu^*_{water}} \frac{u^*_{air}}{y^*_{air}} h^*_{film} \right).$$

After non-dimensionalization, the shear stress balance yields

$$u_{water} \sim \mathcal{O}\left(\frac{1}{M} \frac{u_{air}}{y_{air}} h_{film} \right),$$

where M is the viscosity ratio. Considering the order of magnitude of various terms and remembering that $u_{air} \sim \mathcal{O}(Re^{-1/2})$ in the stagnation region, it is found that

$$u_{water} \sim \mathcal{O}\left(\frac{1}{M}\frac{Re^{-1/2}}{Re^{-1/2}}h_{film}\right), \qquad \Rightarrow u_{water} \sim \mathcal{O}\left(M^{-1}h_{film}\right),$$

where h_{film} is the non-dimensional thickness of the water film. Using this equation in the expression 3.2 for the mass flux balance at the air/water interface derived earlier, it is found that

$$h_{film} \sim \mathcal{O}\left(LWC^{1/2}Re^{-1/4}M^{1/2}\right), \qquad \Rightarrow h_{film} \sim \mathcal{O}\left(LWC^{1/2}Re^{-1/4}D_{aw}^{-1/4}\right),$$

when $M \sim \mathcal{O}(D_{aw}^{-1/2})$. To account for both air heat flux and cooling from droplet impacts, it is necessary to evaluate the water film thickness for a particular liquid water content. This happens when the non-dimensional mass density of water in the airflow is taken to be (see Rothmayer [48], also location (◯) in Fig. 2.2)

$$LWC = Re^{-1/2}D_{aw}\mathfrak{L}.$$

The reader is referred to Rothmayer [48] for details. The liquid water content (LWC) then sets the film height in the stagnation region, which becomes $\mathcal{O}(Re^{-1/2}D_{aw}^{1/4})$. The length scales in the water film are then taken to be

$$(x, y, z) = (0, Re^{-1/2}D_{aw}^{-1/2}H_{ice}, 0) + (Re^{-1/2}X,\ Re^{-1/2}D_{aw}^{1/4}Y,\ Re^{-1/2}Z).$$

Using a stress match at the air/water interface (see Eq. 2.28), the leading order water velocity parallel to the ice surface is found to be $\mathcal{O}(Re^{-1/2}D_{aw}^{3/4})$. The water film experiences three time scales: the air time scale, an intermediate time scale in the water due to the applied air shear stress and the time scale for water accumulation and transport,

obtained from the ratio of the increment in film thickness and the liquid water content. The two time scales within the water, other than the air time scale, are found to be

$$t = D_{aw}^{-1/2}\tau_2, \qquad t = D_{aw}^{-3/4}\tau_3.$$

The time scale at $\mathcal{O}(D_{aw}^{-3/4})$ is the primary time scale within the water, since it is involved in water transport and the water film evolves on this time scale. While the pressure scaling within air is $\mathcal{O}(Re^{-1})$, the pressure within the water is found to be $\mathcal{O}(Re^{-1}D_{aw}^{-1/4})$ in order to balance the water surface tension. Since the leading order temperature perturbation within air is $\mathcal{O}(\mathcal{T})$ and $K_{wa} \sim \mathcal{O}(D_{aw}^{-1/2})$, a balance of the heat flux at the air/water interface yields

$$\frac{\mathcal{T}}{Re^{-1/2}} \sim D_{aw}^{-1/2}\frac{T}{Re^{-1/2}D_{aw}^{1/4}}, \qquad \Rightarrow T \sim D_{aw}^{3/4}\mathcal{T}.$$

The final expansions for the velocities, pressure and temperature in the water film are found to be

$$\begin{aligned}
(u,w) &\sim Re^{-1/2}D_{aw}^{3/4}(\hat{U},\hat{W}) + Re^{-1/2}D_{aw}^{5/4}(\tilde{U}_1,\tilde{W}_1) && (3.3)\\
&\quad + Re^{-1/2}D_{aw}^{3/2}(\tilde{U}_2,\tilde{W}_2) + \dots, \\
v &\sim Re^{-1/2}D_{aw}\hat{V} + Re^{-1/2}D_{aw}^{3/2}\tilde{V}_1 + Re^{-1/2}D_{aw}^{7/4}\tilde{V}_2 + \dots, && (3.4)\\
P &\sim Re^{-1}D_{aw}^{-1/4}P + Re^{-1}D_{aw}^{1/4}\tilde{P}_1 + Re^{-1}D_{aw}^{1/2}\tilde{P}_2 + Re^{-1}D_{aw}^{3/4}\tilde{P}_3 && (3.5)\\
&\quad + Re^{-1}D_{aw}\tilde{P}_4 + \dots, \\
T &\sim 1 \mp \mathcal{T} + \mathcal{T}^2 + D_{aw}^{3/4}\mathcal{T}\hat{T} + D_{aw}^{5/4}\mathcal{T}\tilde{T}_1 + D_{aw}^{3/2}\mathcal{T}\tilde{T}_2 + \dots. && (3.6)
\end{aligned}$$

The $\mathcal{O}(Re^{-1/2}D_{aw}^{1/4})$ water film thickness is small compared to the ice thickness and the air boundary layer thickness, and the final expansions for the water film height and the

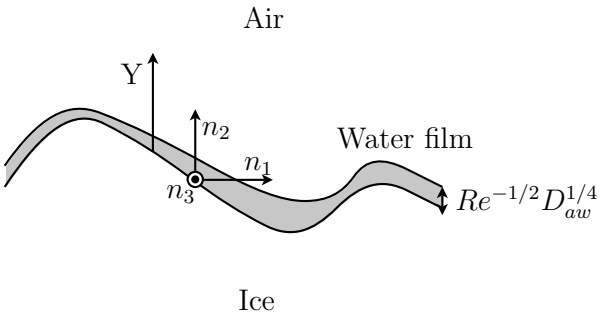

Figure 3.5 Surface normals.

incremental water film thickness are found to be

$$\begin{aligned}(f_{water}, \delta_{water}) \sim\ & (Re^{-1/2}D_{aw}^{-1/2}H_{ice}, 0) + (Re^{-1/2}F_{ice}, 0) \\ & + Re^{-1/2}D_{aw}^{1/4}(F_{water}, \Delta_{water}) + Re^{-1/2}D_{aw}^{1/2}(\tilde{F}_{1,water}, \tilde{\Delta}_{1,water}) \\ & + Re^{-1/2}D_{aw}^{3/4}(\tilde{F}_{2,water}, \tilde{\Delta}_{2,water}) + Re^{-1/2}D_{aw}(\tilde{F}_{3,water}, \tilde{\Delta}_{3,water}) + \dots .\end{aligned}$$

Assuming single valued surfaces at the start of the instability of a flat ice sheet, the leading order surface normals found using the ice height $f_{ice} \sim Re^{-1/2}D_{aw}^{-1/2}H_{ice} + Re^{-1/2}F_{ice} + \dots$ are $(n_1, n_2, n_3) = (-\partial_X F_{ice}, 1, -\partial_Z F_{ice})\ [(\partial_X F_{ice})^2 + (\partial_Z F_{ice})^2 + 1]^{-1/2}$. These normals become the leading order terms in the expansions for the surface normals on both the water film and ice surfaces (in Eqs. 2.28, 2.29 and 2.30).

Ice In order to accommodate temperature changes near the ice surface which vary on the same spatial scales as the air boundary layer, i.e. $\mathcal{O}(Re^{-1/2})$, the length scales inside the ice are the same as those in the airflow, i.e. $(x, y, z) = (0, Re^{-1/2}D_{aw}^{-1/2}H_{ice}, 0) + Re^{-1/2}(X, Y, Z)$. Since the leading order temperature perturbation within water is $\mathcal{O}(D_{aw}^{3/4}\mathcal{T})$, a balance of the heat flux at the water/ice interface yields

$$\frac{D_{aw}^{3/4}\mathcal{T}}{Re^{-1/2}D_{aw}^{1/4}} \sim \frac{T}{Re^{-1/2}}, \qquad \Rightarrow T \sim D_{aw}^{1/2}\mathcal{T}.$$

Note that this equation also follows from a balance with the air heat flux $\mathcal{O}(\mathcal{T}Re^{1/2})$, using the fact that the heat flux is constant through the thin water film and $K_{wa} \sim \mathcal{O}(D_{aw}^{-1/2})$. The temperature expansion within the ice is then found to be

$$T \sim 1 \mp \mathcal{T} + \mathcal{T}^2 + D_{aw}^{1/2}\mathcal{T}\hat{T} + D_{aw}\mathcal{T}\tilde{T} + \dots ,$$

where the higher order term $D_{aw}\mathcal{T}$ is obtained from a similar heat flux balance at the water/ice interface as mentioned above. It becomes necessary to consider terms in the expansion for the ice height which are related to the two water time scales mentioned earlier and which also appear in the Stefan condition for ice growth (to be discussed later in the Section 3.5, see also Eq. 2.34). Including these terms, the final ice height expansions become

$$\begin{aligned}(f_{ice}, \delta_{ice}) \sim (Re^{-1/2}D_{aw}^{-1/2}H_{ice}, 0) + Re^{-1/2}(F_{ice}, \Delta_{ice}) \\ +Re^{-1/2}D_{aw}^{1/4}\mathcal{T}(\tilde{F}_{1,ice}, \tilde{\Delta}_{1,ice}) + Re^{-1/2}D_{aw}^{1/2}\mathcal{T}(\tilde{F}_{2,ice}, \tilde{\Delta}_{2,ice}) + \dots .\end{aligned}$$

From the Stefan condition (Eq. 2.34) which controls the time scale for ice growth, and using $K_{wa} \sim \mathcal{O}(D_{aw}^{-1/2})$, it is found that

$$\frac{D_{aw}^{3/4}\mathcal{T}}{Re^{-1/2}D_{aw}^{1/4}} \sim \frac{1}{K_{wa}}\frac{Re}{D_{aw}}\frac{Re^{-1/2}}{t}, \qquad \Rightarrow t \sim D_{aw}^{-1}\mathcal{T}^{-1}.$$

Therefore, the time scale for the ice growth is given by

$$t = D_{aw}^{-1}\mathcal{T}^{-1}\tau_4.$$

It should be noted that the time scales of air at $\mathcal{O}(1)$, water at $\mathcal{O}(D_{aw}^{-1/2}, D_{aw}^{-3/4})$ and ice at $\mathcal{O}(D_{aw}^{-1}\mathcal{T}^{-1})$ are all well separated when $D_{aw} \ll 1$ and $\mathcal{T} \ll 1$, i.e. $1 \ll D_{aw}^{-1/2} \ll D_{aw}^{-3/4} \ll D_{aw}^{-1}\mathcal{T}^{-1}$.

3.5 Equations for stagnation line icing

The time scales discussed above are combined into the single multiple scales expansion,

$$\partial_t \sim \partial_{\tau_1} + D_{aw}^{1/2}\partial_{\tau_2} + D_{aw}^{3/4}\partial_{\tau_3} + D_{aw}\mathcal{T}\partial_{\tau_4} + \dots . \tag{3.7}$$

In this section, $<>_i$ refers to averages over each time scale, where the index $i = 1, 2, 3, 4$ is used to denote the time scales listed previously and $<>_{i,j}$ and $<>_{i,j,k}$ are averages over successive time scales.

Air Using the expansions for the velocities in air (given in Section 3.4), the continuity equation in air becomes incompressible and is given at leading order by

$$U_X + V_Y + W_Z = 0. \tag{3.8}$$

The momentum equation in air also become incompressible, leading to

$$\begin{aligned} U_{\tau_1} + UU_X + VU_Y + WU_Z &= -P_X + U_{XX} + U_{YY} + U_{ZZ}, & (3.9)\\ V_{\tau_1} + UV_X + VV_Y + WV_Z &= -P_Y + V_{XX} + V_{YY} + V_{ZZ}, & (3.10)\\ W_{\tau_1} + UW_X + VW_Y + WW_Z &= -P_Z + W_{XX} + W_{YY} + W_{ZZ}. & (3.11) \end{aligned}$$

The ideal gas law, given by $1 + \gamma M_\infty^2 P = \rho T$, simplifies to $\gamma m_\infty^2 P = R + \hat{T}$. Since the flow is incompressible at leading order, it becomes necessary to consider higher order terms for the velocities in the energy equation (for example, see Stewartson [53]). When the expansion for velocities are substituted and the leading and higher order continuity

equations and the ideal gas law are used, the energy equation in air ultimately gives

$$\hat{T}_{\tau_1} + U\hat{T}_X + V\hat{T}_Y + W\hat{T}_Z = \mathrm{Pr}^{-1}\left[\hat{T}_{XX} + \hat{T}_{YY} + \hat{T}_{ZZ}\right]. \tag{3.12}$$

The above equations give an unsteady Navier-Stokes problem on the $\mathcal{O}(1)$ air time scale.

Water Starting from Eq. 2.26 and considering all the time scales for the water film i.e. the first three terms of Eq. 3.7, the leading order x-momentum equation becomes

$$\frac{\partial \hat{U}}{\partial \tau_1} = -\frac{\partial P}{\partial X} + \mathcal{M}\frac{\partial^2 \hat{U}}{\partial Y^2},$$

and the leading order energy equation (Eq. 2.27) within the water film is found to be

$$\frac{\partial \hat{T}}{\partial \tau_1} = \frac{C_{aw}\mathcal{K}}{\mathrm{Pr}}\frac{\partial^2 \hat{T}}{\partial Y^2}.$$

The water is assumed to be incompressible and averages of the leading order equations yield

$$-\langle P_X\rangle_1 + \mathcal{M}\left\langle \hat{U}_{YY}\right\rangle_1 = 0\,, \tag{3.13}$$

$$\left\langle \hat{T}_{YY}\right\rangle_1 = 0\,. \tag{3.14}$$

Any further averaging with respect to the water time scale will preserve the form of these equations. Therefore, averaging over the air time scale leads to an averaged Couette-Poiseuille flow as well as a pure conduction problem within the water film. Because the water film thickness at $\mathcal{O}(Re^{-1/2}D_{aw}^{1/4})$ is much smaller than the $\mathcal{O}(Re^{-1/2})$ air boundary layer thickness, it does not exert a leading order effect on the airflow. Also, because the averaged thermal problem in the water film is pure conduction, the water film acts as a passive transmitter of heat flux from the air to the ice.

Air/Water Interface The ice surface beneath the water film experiences the heat flux from the airflow at the air/water interface through the water film. In order to estimate the heat flux at the ice surface from the water film, it becomes necessary to consider the heat flux balance at the air/water interface. As mentioned earlier, the temperature in the airflow is given by $T \sim 1 + \mathcal{T}\hat{T} + \ldots$. The heating due to the mass deposition of droplets may be taken into account by using a temperature expansion of the form

$$(T_{impact}, T_{drops}) \sim 1 + \mathcal{T}(\hat{T}_{impact}, \hat{T}_{drops}) + \ldots .$$

Note that this equation assumes that the water droplets are at some known temperature which is proportional to the difference between the air freestream temperature and the freezing temperature. Also note that the impact heating is $\mathcal{O}(\mathcal{T})$ since $M_\infty^2 \sim \mathcal{O}(\mathcal{T})$ and the droplets have approximately the same velocity magnitude as the freestream.

A sample derivation is outlined below which uses the multiple scales approach to arrive at an averaged growth of the water film. This approach is also used later to evaluate the heat flux at the air/water interface which is experienced by the ice surface due to the thin purely conducting water film. From the kinematic condition (Eq. 2.29) for the water film, the equations for the increment in the water surface thickness become

$$\partial_{\tau_1}\Delta_{water} = 0, \qquad \partial_{\tau_1}\tilde{\Delta}_{1,water} = 0,$$

$$< \partial_{\tau_2}\Delta_{water} >_1 + \underline{< \partial_{\tau_1}\tilde{\Delta}_{2,water} >_1} = 0,$$

$$< \partial_{\tau_3}\Delta_{water} >_{1,2} + \underline{< \partial_{\tau_2}\tilde{\Delta}_{1,water} >_{1,2}} + \underline{< \partial_{\tau_2}\tilde{\Delta}_{1,water} >_{1,2}} = \mathcal{L}(\beta_{CE}\dot{\Delta}_{water}/V_{drop}),$$

$$< \partial_{\tau_3}\Delta_{water} >_{1,2} = \mathcal{L}(\beta_{CE}\dot{\Delta}_{water}/V_{drop}),$$

where brackets are the averaging over a time scale given by the subscript number. In addition, $\dot{\Delta} = [V_{1,drop} n_1 + V_{3,drop} n_3 + |V_{2,drop}|]$ and $(n_1, n_2, n_3) = (-F_{ice,X}, 1, -F_{ice,Z}) \left[F_{ice,X}^2 + F_{ice,Z}^2 + 1\right]^{-1/2}$. The surface normals for the water film are given by

$$\begin{aligned} n_{1,w} &\sim n_1 - D_{aw}^{1/4} \partial_X F_{water} n_2 + (1/2) D_{aw}^{1/2} \partial_X F_{ice} [(n_2)^3 G_w] + \mathcal{O}(D_{aw}^{3/4}), \\ n_{2,w} &\sim n_2 - (1/2) D_{aw}^{1/2} [(n_2)^3 G_w] + \mathcal{O}(D_{aw}), \end{aligned}$$

where $G_w = [(\partial_X F_{water})^2 + (\partial_X F_{water})^2]$. $n_{3,w}$ is similar to $n_{1,w}$ in form. The averaging process assumes that changes in higher order terms such as $\partial_{\tau_1} \tilde{\Delta}_{2,water}$ (the underlined terms in the above equations) are bounded, which implies that $< \partial_{\tau_1} \tilde{\Delta}_{2,water} >_1 = 0$. This means that the water accumulation and the mean motion of the water film occurs only on the $D_{aw}^{-3/4}$ time scale, while the perturbations on faster time scales do not contribute to this mean motion. The multiples scales approach is used again for the heat fluxes at the air/water interface. Using the expansions for the temperature in air and water and averaging over the air time scale and the time scale in the water film due to shear stress, the heat flux balance at the air/water interface then reduces to

$$\left\langle \left(\frac{\partial \hat{T}}{\partial X_j} \right)_{air} n_j \right\rangle_{1,2} = \left\langle \mathcal{K} \left(\frac{\partial \hat{T}}{\partial Y} \right)_{water} \right\rangle_{1,2} + \frac{\mathrm{Pr}}{C_{aw}} \left[\mp 1 - \hat{T}_{impact} \right] \mathcal{L} \beta_{CE}, \qquad (3.15)$$

where $n_j = (n_1, n_2, n_3)$, $X_j = (X, Y, Z)$ in air, $\hat{T}_{impact} = \hat{T}_{drops} + (\gamma - 1) C_{aw} m_\infty^2 V_{i,drop}$ $V_{i,drop}/2$ and C_{aw} is the ratio of the specific heats of air and water. Similarly, the kinematic condition at the air/water interface reduces to

$$\left\langle \hat{V}_{water} \right\rangle_{1,2} + \mathcal{L} \beta_{CE} = \frac{dF_{water}}{d\tau_3} + \left\langle \hat{U}_{water} \right\rangle_{1,2} \frac{dF_{water}}{dX} + \left\langle \hat{W}_{water} \right\rangle_{1,2} \frac{dF_{water}}{dZ}.$$

The heat transfer within the water film primarily occurs along the y-direction (see Fig. 3.5). Note that both heat flux balance and the kinematic condition are now at the longer

water film time scale at $\mathcal{O}(D_{aw}^{-3/4})$. Here, water droplets are assumed have a temperature close to T_∞. The heat addition due to the impact of the droplets is modeled using the collection efficiency of water droplets β_{CE} which measures the relative rate at which a location on the ice surface collects water droplets (see Gent *et al* [9] for details). β_{CE} usually varies between 0 and 0.8 and is constant because of the assumption of uniform local deposition of droplets near the stagnation line. This is a common approach for modeling the mass deposition of water droplets in aircraft icing. A more detailed analysis of droplet trajectories and impacts is beyond the scope of the present study. Since the current work seeks to study the ice surface stability on the slower ice time scale, the averaged constant heat flux from the air through the conducting water film is of primary interest. This is a valid assumption as long as a dryout of the water film does not occur.

Ice The ice growth described later in this section by the Stefan condition is influenced by both the heat fluxes from the water film and the ice at the ice surface. In order to evaluate the heat flux within the ice at the ice surface, it is essential to consider several effects inside the ice. The ice surface growth is influenced by the Gibbs-Thomson effect which produces small changes in the freezing temperature of the ice surface which depend on the local surface curvature. The temperature at the ice surface, in non-dimensional form, is given by

$$T_{water} = T_{ice} = T_{freezing}\left(1 - \varepsilon\kappa_{ice}\right),$$

where $\varepsilon = \gamma^*_{g,ice/water}/(\rho^*_{ice}H^*_{ice/water}L) = Re^{-1/2}D_{aw}^{1/2}\mathcal{T}E \ll 1$ is the non-dimensional Gibbs-Thomson parameter discussed in Section 2.4 and the curvature of the ice surface is $\kappa_{ice} = -\partial_x^2 f_{ice}[1 + (\partial_x f_{ice})^2]^{-3/2}\ -\partial_z^2 f_{ice}[1 + (\partial_z f_{ice})^2]^{-3/2}$. The ice has two regions: a passive core governed by a one-dimensional heat conduction problem where the mean ice thickness is at $\mathcal{O}(Re^{-1/2}D_{aw}^{-1/2})$, and a region near the ice surface where the temperature

responds to local changes in the shape of the ice surface at a thickness of $\mathcal{O}(Re^{-1/2})$ (see Fig. 3.4). Using the coordinate $y = Re^{-1/2}D_{aw}^{-1/2}\hat{Y}$, the temperature profile within the core of the ice is found to be

$$T_{ice} = 1 + \mathcal{T}\hat{T}_1(\hat{Y}) + \mathcal{T}^2\hat{T}_2(\hat{Y}) + \dots , \tag{3.16}$$

where $\hat{T}_1 = \frac{\mp 1 - \hat{T}_{airfoil}}{H_{ice}}\hat{Y} + \hat{T}_{airfoil}$, $\hat{T}_2 = \frac{(M_0+K_0)}{2}\left[\mp 1 - \hat{T}_{airfoil}\right]^2\left(1 - \frac{\hat{Y}}{H_{ice}}\right)\frac{\hat{Y}}{H_{ice}} + \frac{\hat{Y}}{H_{ice}}$ and $\hat{T}_{airfoil}$ is the temperature of the airfoil surface. The air viscosity and the thermal conductivities for water and ice are given by

$$(\mu_{air},\, k_{water},\, k_{ice}) = 1 + \mathcal{T}\hat{T}_1(M_0, k'_{water}(\mp 1), k'_{ice}(\mp 1)) + \mathcal{O}(\mathcal{T}^2).$$

The coefficients $M_0 = \mu'_{air}(\mp 1)$ and $K_0 = k'_{ice}(\mp 1) - k'_{water}(\mp 1)$ are the rate of change of viscosity and thermal conductivities with temperature at the ice surface. Near the ice surface, the length scales are $(x, y, z) = (0, Re^{-1/2}D_{aw}^{-1/2}H_{ice}, 0) + Re^{-1/2}(X, Y, Z)$. The energy equation in the ice near the water/ice interface then reduces to

$$\hat{T}_{XX} + \hat{T}_{YY} + \hat{T}_{ZZ} = 0.$$

Stefan condition The air time scale, the two water time scales and the ice growth time scale must all be considered in the Stefan condition for the ice growth when using a multiple scales approach. The averaging process explained earlier for the water film growth is used here for the growth of the ice surface.

The ice surface is assumed to be at a later stage of ice accretion when $f_{ice} \sim Re^{-1/2}D_{aw}^{-1/2}H_{ice} + Re^{-1/2}F_{ice} + \dots$ and the heat flux in the airflow, the thin water film and the heat flux in ice are of the same order of magnitude. Using the scalings for the ice height, the time scale for the ice surface, the kinematic condition at the water/ice interface and the averaging over the air/water time scales, the expansions for the surface

normals on the ice surface are given by

$$\begin{aligned} n_{1,ice} &\sim n_1 - D_{aw}^{1/4}\mathcal{T}\partial_X\tilde{F}_{1,ice}n_2 - D_{aw}^{1/2}\mathcal{T}\partial_X\tilde{F}_{2,ice}n_2 + (1/2)D_{aw}^{1/2}\mathcal{T}^2\partial_X F_{ice}[(n_2)^3 G_{1,ice}] \\ &\quad +\mathcal{O}(D_{aw}^{3/4}\mathcal{T}^2), \\ n_{2,ice} &\sim n_2 - (1/2)D_{aw}^{1/2}\mathcal{T}^2[(n_2)^3 G_{1,ice}] + \mathcal{O}(D_{aw}\mathcal{T}^2), \end{aligned}$$

where $G_{1,ice} = [(\partial_X\tilde{F}_{1,ice})^2 + (\partial_X\tilde{F}_{1,ice})^2]$. $n_{3,ice}$ is similar to $n_{1,ice}$ in form. Similarly, the equation for the increment in the ice thickness from the Stefan condition yields trivial solutions at leading order, given by

$$\begin{aligned} \partial_{\tau_1}\Delta_{ice} = 0, \quad &\Rightarrow \quad \Delta_{ice} = \Delta_{ice}(\tau_2, \tau_3, \tau_4), \\ \partial_{\tau_2}\Delta_{ice} = 0, \quad &\Rightarrow \quad \Delta_{ice} = \Delta_{ice}(\tau_3, \tau_4), \end{aligned}$$

and

$$\partial_{\tau_3}\Delta_{ice} = 0, \quad \Rightarrow \quad \Delta_{ice} = \Delta_{ice}(\tau_4).$$

Similarly, $\tilde{\Delta}_{1,ice} = \tilde{\Delta}_{1,ice}(\tau_3, \tau_4)$ and $\tilde{\Delta}_{2,ice}(\tau_2, \tau_3, \tau_4)$. The Stefan condition gives

$$\left(\frac{\partial\hat{T}}{\partial Y}\right)_{water} = \frac{k_{ice}}{k_{water}}K_{iw}\left(\frac{\partial\hat{T}}{\partial X_j}\right)_{ice} n_j - \frac{\mathrm{Pr}_{air}}{\mu_{air}}\frac{1}{\mathcal{K}C_{ai}}Ste^{-1}(\partial_{\tau_4}\Delta_{ice} + \partial_{\tau_3}\tilde{\Delta}_{1,ice} + \partial_{\tau_2}\tilde{\Delta}_{2,ice}).$$

Δ_{ice}, $\tilde{\Delta}_{1,ice}$ and $\tilde{\Delta}_{2,ice}$ are not functions of the air time scale. When averaged over the air time scale and the two water time scales, the Stefan condition becomes

$$\begin{aligned} \left\langle\left(\frac{\partial\hat{T}}{\partial Y}\right)_{water}\right\rangle_{1,2,3} &= \left\langle\frac{k_{ice}}{k_{water}}K_{iw}\left(\frac{\partial\hat{T}}{\partial X_j}\right)_{ice} n_j\right\rangle_{1,2,3} \\ &\quad -\frac{\mathrm{Pr}}{\mu_{air}}\frac{1}{\mathcal{K}C_{ai}Ste}\left[\langle\partial_{\tau_4}\Delta_{ice}\rangle_{2,3} + \left\langle\partial_{\tau_3}\tilde{\Delta}_{1,ice}\right\rangle_{2,3} + \left\langle\partial_{\tau_2}\tilde{\Delta}_{2,ice}\right\rangle_{2,3}\right]. \end{aligned}$$

Observing that $\partial_{\tau_3}\tilde{\Delta}_{1,ice}$ and $\partial_{\tau_2}\tilde{\Delta}_{2,ice}$ are bounded in these time scales and Δ_{ice} is not a function of these time scales, the final Stefan condition becomes

$$\left\langle \left(\frac{\partial \hat{T}}{\partial Y}\right)_{water} \right\rangle_{1,2,3} = \left\langle \frac{k_{ice}}{k_{water}} K_{iw} \left(\frac{\partial \hat{T}}{\partial X_j}\right)_{ice} n_j \right\rangle_{1,2,3} - \frac{\mathrm{Pr}}{\mu_{air}} \frac{1}{\mathcal{K}Ca_i} Ste^{-1} \partial_{\tau_4} \Delta_{ice}.$$

From the kinematic condition, at the leading order,

$$\partial_{\tau_1}\Delta_{ice} = 0 = D_{iw}\partial_{\tau_1}F_{ice} + n_1\frac{\partial F_{ice}}{\partial X}\partial_{\tau_1}F_{ice} + n_3\frac{\partial F_{ice}}{\partial Z}\partial_{\tau_1}F_{ice}.$$

Since $D_{iw} + n_1\frac{\partial F_{ice}}{\partial X} + n_3\frac{\partial F_{ice}}{\partial Z} \neq 0$ for all cases,

$$\partial_{\tau_1}F_{ice} = 0.$$

Similarly, for other higher order terms, the kinematic condition for the ice surface yields $\partial_{\tau_1}\tilde{F}_{1,ice} = 0$, $\partial_{\tau_2}F_{ice} = 0$, $\partial_{\tau_1}\tilde{F}_{2,ice} = 0$, $\partial_{\tau_3}F_{ice} = 0$, $\partial_{\tau_2}\tilde{F}_{1,ice} = 0$. Considering the kinematic condition at order of the Stefan condition for the ice growth, the equation for the evolution of the ice surface is found to be

$$\begin{aligned} &n_2(\partial_{\tau_4}\Delta_{ice} + \partial_{\tau_3}\tilde{\Delta}_{1,ice} + \partial_{\tau_2}\tilde{\Delta}_{2,ice}) = D_{iw}(\partial_{\tau_4}F_{ice} + \partial_{\tau_3}\tilde{F}_{1,ice} + \partial_{\tau_2}\tilde{F}_{2,ice}) \\ &+n_1\frac{\partial F_{ice}}{\partial X}(\partial_{\tau_4}F_{ice} + \partial_{\tau_3}\tilde{F}_{1,ice} + \partial_{\tau_2}\tilde{F}_{2,ice}) + n_3\frac{\partial F_{ice}}{\partial Z}(\partial_{\tau_4}F_{ice} + \partial_{\tau_3}\tilde{F}_{1,ice} + \partial_{\tau_2}\tilde{F}_{2,ice}). \end{aligned}$$

In this equation, terms such as $d\tilde{F}_{2,ice}/d\tau_2$, $d\tilde{F}_{1,ice}/d\tau_3$ are assumed to bounded over the time scales chosen for averaging (see Rothmayer [47] for details) which yields

$$n_2(\partial_{\tau_4}\Delta_{ice}) = D_{iw}\partial_{\tau_4}F_{ice} + n_1\frac{\partial F_{ice}}{\partial X}\partial_{\tau_4}F_{ice} + n_3\frac{\partial F_{ice}}{\partial Z}\partial_{\tau_4}F_{ice}.$$

This kinematic condition is used in subsequent sections along with the Stefan condition for the growth of the ice surface for linearized stability analysis of this ice surface.

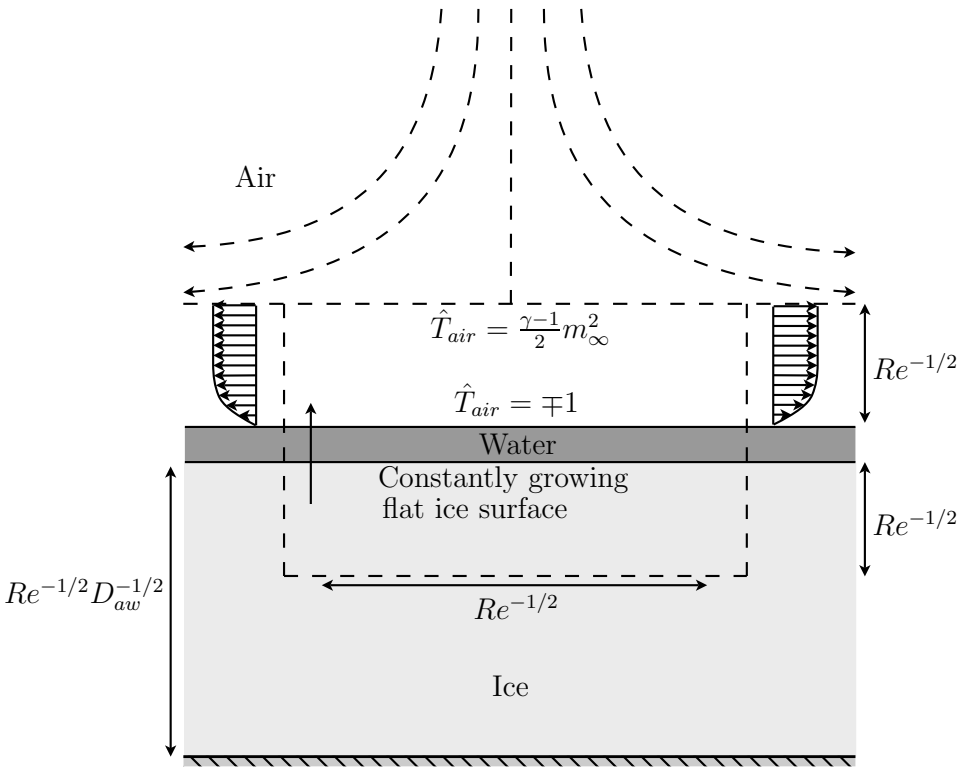

Figure 3.6 Hiemenz flow over a flat undisturbed ice surface.

3.6 Hiemenz flow

Near the leading edge stagnation line of Fig. 3.3, the undisturbed ice surface is taken to be flat. Matching the stagnation region to a thin airfoil with a parabolic leading edge shows that the inviscid stagnation line stream-function in non-dimensional form becomes $\psi = axy$, where the strength of the stagnation flow 'a' is the non-dimensional nose radius of curvature. The coordinate transformation is then written as $(x, y) = (0, Re^{-1/2} D_{aw}^{-1/2} H_{ice}) + Re^{-1/2} a^{-1/2} (\xi, \eta)$, where Re is the chord-based Reynolds number (see Fig. 3.6). The viscous stream-function becomes $\psi = Re^{-1} \bar{\psi}$, where $\bar{\psi} = \xi f(\eta)$. Since the velocities within the stagnation flow are $\mathcal{O}(Re^{-1/2})$, viscous dissipation does not affect the temperature in the boundary layer at the leading order. As a result, the temperature is dependent only on the heating due to conduction through the boundary layer from the inviscid stagnation temperature. The ice surface is held at the freezing

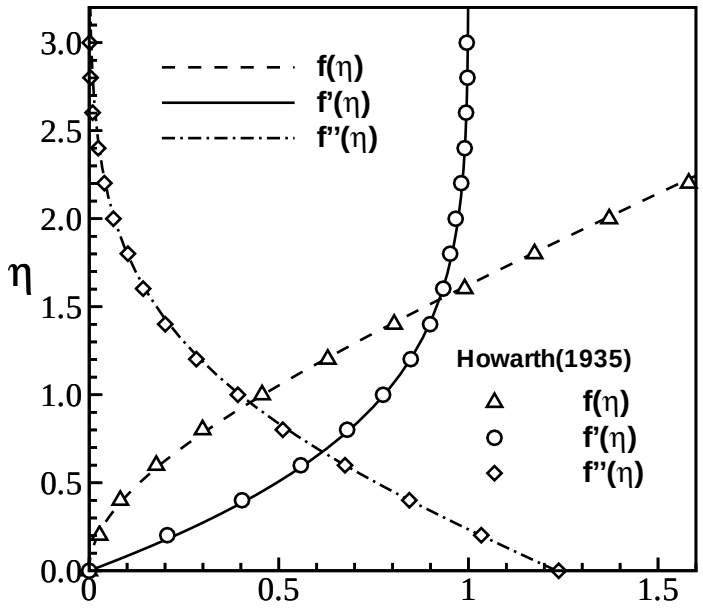

Figure 3.7 The solution for the Hiemenz flow. The solutions of Howarth are taken from Schlichting [3].

temperature. Therefore, the boundary conditions for the energy equation do not have any streamwise dependence, and the temperature within the boundary layer is only a function of the normal coordinate η.

The Hiemenz solution in the transformed (ξ, η) coordinates (see Schlichting [3]) is found from

$$f'''(\eta) + f(\eta) f''(\eta) + 1 - f'(\eta)^2 = 0 \tag{3.17}$$

and the low Mach number Hiemenz energy equation becomes

$$\mathrm{Pr}^{-1} \hat{T}_{H,\eta\eta} + f(\eta) \hat{T}_{H,\eta} = 0. \tag{3.18}$$

Here, the stagnation pressure is given by $P_0 = P_H + af(\eta)^2/2 + af'(\eta) + a\xi^2/2$, and the boundary conditions at the ice surface are $f(0) = 0$ and $f'(0) = 0$. At the edge of

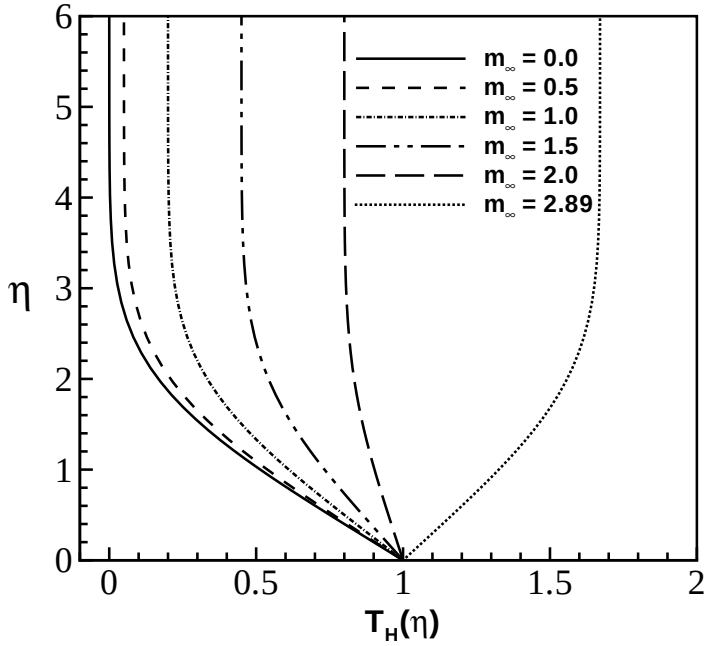

Figure 3.8 Temperature solution in air for the Hiemenz flow.

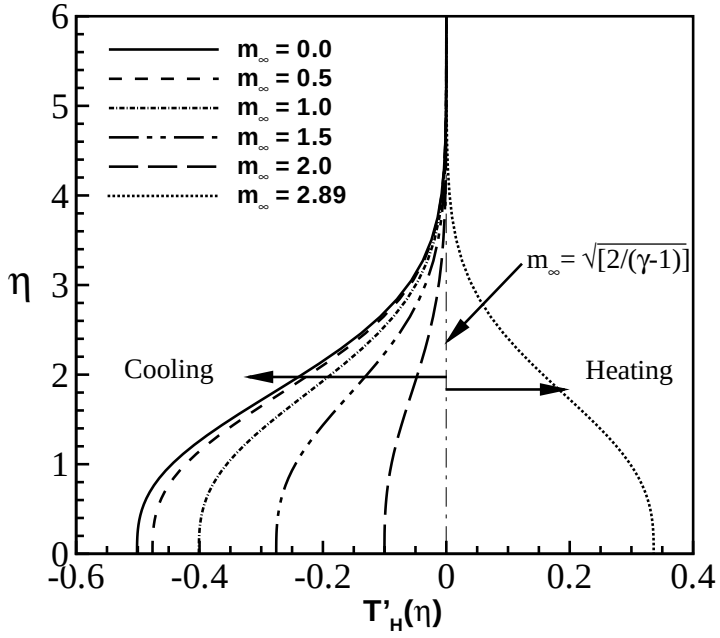

Figure 3.9 Heat flux profiles in air for the Hiemenz flow.

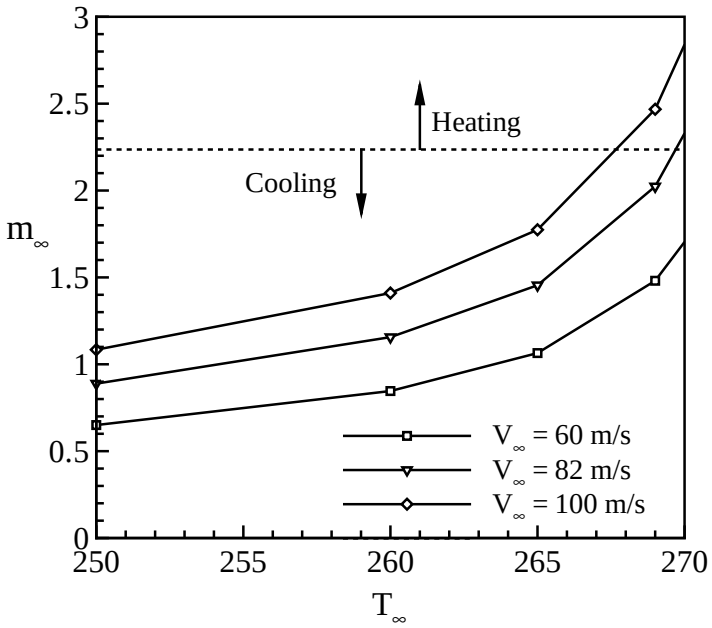

Figure 3.10 Change in m_∞ with free-stream velocity and temperature (see Section 3.9).

the boundary layer a velocity match to the inviscid flow is imposed using $f''(\infty) = 1$. Similarly, the temperature at the ice surface is kept at the freezing temperature of water using $\hat{T}_H(0) = 1$. At the edge of the boundary layer, the temperature is matched with the inviscid stagnation temperature $\hat{T}_H(\infty) = (\gamma - 1)\, m_\infty^2/2$. Inside the ice and away from the interface (see Section 3.5), the energy equation is found to be a one-dimensional heat conduction problem, i.e.

$$\hat{T}_{S,\eta\eta} \;=\; 0$$

and the boundary condition is $\hat{T}_{S,\eta}(-\infty) = (\mp 1 - \hat{T}_{airfoil})/\bar{H}_{ice}$ where $H_{ice} \sim a^{-1/2}\bar{H}_{ice}$.

The Hiemenz solution is used to obtain the streamwise as well as vertical velocities within the boundary layer which are then used in the linearized stability analysis for the ice surface, discussed in the next section (Section 3.7). The solution of the streamfunction in Eq. 3.17 gives the streamwise as well as vertical velocity within the air boundary

layer. In Fig. 3.7, good agreement is seen with previous results for the streamfunction and its derivatives in the normal coordinate. The boundary layer thickness for the Hiemenz flow is approximately 2.0 (see Fig. 3.7). As the temperature at the edge of the air boundary layer increases toward the inviscid stagnation temperature, the temperature within the boundary layer increases as shown in Fig. 3.8. In Fig 3.9, the heat flux from the airflow at the ice surface changes from cooling to heating as the scaled Mach number m_∞ increases to the point where the inviscid stagnation temperature becomes larger than the freezing temperature of the ice surface. This change from cooling to heating happens with a change in freestream temperature and velocity which gives a corresponding scaled Mach number m_∞ and this is shown in Fig. 3.10 (also see Eq. 3.1). This change in air heat flux affects the stability of the ice surface.

3.7 Formulation of the stability analysis

The multiple scales analysis results in an ice growth problem which is dependent only on the ice time scale . It is also seen that the effect of the airflow is averaged over the air time scale, which implies that any small fluctuation in the air does not contribute to the heat transfer into the ice. For an almost flat surface $n_2 \gg (n_1 F_{ice,X}, n_3 F_{ice,Z})$ since $(F_{ice,X}, F_{ice,Z}) \ll 1$, $(n_1, n_3) = (F_{ice,X}, F_{ice,Z})$ and $n_2 = 1$ which gives

$$\partial_{\tau_4} \Delta_{ice} = D_{iw} \partial_{\tau_4} F_{ice}.$$

The averaged Stefan condition then for the growth of the ice surface becomes

$$D_{iw} \frac{dF_{ice}}{d\tau_4} = \frac{\mathcal{K} C_{ai} Ste}{\mathrm{Pr}} \left[K_{iw} \left\langle \left(\frac{\partial \hat{T}}{\partial X_j} \right)_{ice} n_j \right\rangle_{1,2,3} - \left\langle \left(\frac{\partial \hat{T}}{\partial Y} \right)_{water} \right\rangle_{1,2,3} \right],$$

where $C_{ai} = c^*_{p,air}/c^*_{ice}$, $D_{iw} = \rho^*_{ice}/\rho^*_{water}$, $K_{iw} = k^*_{ice}(T_\infty)/k^*_{water}(T_\infty)$, $Ste = c^*_{ice}T_\infty/L^*_{water/ice}$ and $L^*_{water/ice}$ is the latent heat of fusion for ice. The leading order flat ice surface is only a function of τ_4 and grows at a constant velocity V_0 given later in this section. The coordinates are then written as

$$\begin{aligned}(x,y,z) &= (0, Re^{-1/2}D_{aw}^{-1/2}H_{ice}, 0) + Re^{-1/2}(X, V_0\tau_4 + Y, Z) \\ &= (0, Re^{-1/2}D_{aw}^{-1/2}a^{-1/2}\bar{H}_{ice}, 0) + Re^{-1/2}a^{-1/2}(\xi, \bar{V}_0\bar{\tau}_4 + \eta, \zeta),\end{aligned}$$

where $\bar{\tau}_4 = a\tau_4$ and $\bar{V}_0 = a^{-1/2}V_0$. The averaged Stefan condition for ice growth at leading order gives the baseline ice surface velocity

$$\bar{V}_0 = \frac{\partial \bar{f}_{ice}}{\partial \bar{\tau}_4} = \frac{\mathcal{K}C_{ai}Ste}{\Pr D_{iw}}\left[K_{iw}\left\langle\left(\hat{T}_{S,\eta}\right)_{ice}\right\rangle_{1,2,3} - \left\langle(T_\eta)_{water}\right\rangle_{1,2,3}\right], \tag{3.19}$$

where $\left\langle(T_\eta)_{water}\right\rangle_{1,2,3} = (1/\mathcal{K})\hat{T}'_H(0) - (\mathcal{L}\Pr)/(\mathcal{K}a^{1/2}C_{aw})\ [\mp 1 - \hat{T}_{impact}]\beta_{CE}\bar{V}_{drop}$, and the droplet velocity in y-direction is $\bar{V}_{drop} = |v_{2,d}|\,/\,|v_d|$ and $|v_d| = \sqrt{v_{1,d}^2 + v_{2,d}^2 + v_{3,d}^2}$. The equations for the airflow and the ice remain unchanged due to Galilean invariance between inertial reference frames of a Hiemenz flow, with $U_H = aXf'(\eta) = \sqrt{a}\xi f'(\eta)$ and $V_H = -\sqrt{a}f(\eta)$. The airflow is a small perturbation on this Hiemenz flow:

$$\begin{aligned}&\left\langle\{U,V,W,P,\hat{T}\}\right\rangle_{1,2,3} \sim \{U_H(\xi,\eta), V_H(\xi,\eta), 0, P_H(\xi,\eta), T_H(\eta)\} \\ &+\varepsilon\{a^{1/2}\bar{U}(\xi,\eta,\bar{\tau}_4), a^{1/2}\bar{V}(\xi,\eta,\bar{\tau}_4), a^{1/2}\bar{W}(\xi,\eta,\bar{\tau}_4), a\bar{P}(\xi,\eta,\bar{\tau}_4), \bar{T}(\xi,\eta,\bar{\tau}_4)\}e^{i\bar{\beta}\zeta} + \ldots .\end{aligned}$$

where $\bar{\beta} = a^{-1/2}\beta$ and β is the spanwise wave number in Z. The temperature inside ice and the ice height are taken to be

$$\left\langle\{\hat{T}_{ice}, f_{ice}\}\right\rangle_{1,2,3} \sim \{T_S(\eta), F_{ice}(\bar{\tau}_4)\} + \varepsilon\{\bar{T}(\xi,\eta,\bar{\tau}_4), a^{-1/2}\bar{F}_{ice}(\xi,\bar{\tau}_4)\}e^{i\bar{\beta}\zeta} + \ldots .$$

The equations for the perturbation quantities in the transformed coordinates are then found to be

$$\begin{aligned}
\xi f'(\eta)\bar{U}_\xi + \bar{U} f'(\eta) - f(\eta)\bar{U}_\eta + \bar{V}\xi f''(\eta) &= -\bar{P}_\xi + \bar{U}_{\xi\xi} + \bar{U}_{\eta\eta} - \bar{\beta}^2\bar{U}, \quad (3.20)\\
\xi f'(\eta)\bar{V}_\xi - f(\eta)\bar{V}_\eta - \bar{V} f'(\eta) &= -\bar{P}_\eta + \bar{V}_{\xi\xi} + \bar{V}_{\eta\eta} - \bar{\beta}^2\bar{V}, \quad (3.21)\\
-2f'(\eta)\bar{U}_\xi - 2\xi f''(\eta)\bar{V}_\xi + 2f'(\eta)\bar{V}_\eta &= \bar{P}_{\xi\xi} + \bar{P}_{\eta\eta} - \bar{\beta}^2\bar{P}, \quad (3.22)\\
\xi f'(\eta)\bar{T}_\xi - f(\eta)\bar{T}_\eta + \bar{V}T'_H &= \mathrm{Pr}^{-1}(\bar{T}_{\xi\xi} + \bar{T}_{\eta\eta} - \bar{\beta}^2\bar{T}). \quad (3.23)
\end{aligned}$$

The Poisson equation for the perturbation pressure is found using the continuity equation and the z-momentum equation. When solving the above linearized equations for the airflow, the boundary conditions at the edge of the boundary layer are

$$\bar{U} = 0, \quad \bar{V} = 0, \quad \bar{T} = 0, \quad \bar{P} = 0.$$

The boundary conditions for the linearized airflow at the ice surface become independent of the stagnation strength parameter 'a' and may be written as

$$\bar{U}(\xi, 0, \bar{\tau}_4) = -\xi f''(0)\bar{F}_{ice}(\xi, \bar{\tau}_4), \quad (3.24)$$

$$\bar{V}(\xi, 0, \bar{\tau}_4) = f'(0)\bar{F}_{ice}(\xi, \bar{\tau}_4) = 0, \quad (3.25)$$

$$\bar{T}(\xi, 0, \bar{\tau}_4) = -\hat{T}'_H(0)\bar{F}_{ice}(\xi, \bar{\tau}_4), \quad (3.26)$$

with $\bar{W}(\xi, 0, \bar{\tau}_4) = 0$. To enforce the continuity equation for the perturbation quantities, the pressure is specified using the following boundary condition evaluated at $\eta = 0$

$$0 = -\bar{P}_\eta + \bar{V}_{\eta\eta}. \quad (3.27)$$

Within the ice, the equation for the perturbation temperature becomes

$$\bar{T}_{\xi\xi} + \bar{T}_{\eta\eta} - \bar{\beta}^2 \bar{T} \;=\; 0. \tag{3.28}$$

At the water/ice interface, the perturbation temperature of the ice is found from the Gibbs-Thomson relation to be

$$\bar{T}\left(\xi, 0, \bar{\tau}_4\right) = -\bar{F}_{ice}\left(\xi, \bar{\tau}_4\right) T_{S,\eta}(0) + \bar{E}\bar{F}_{ice,\xi\xi}\left(\xi, \bar{\tau}_4\right) - \bar{E}\bar{\beta}^2 \bar{F}_{ice}\left(\xi, \bar{\tau}_4\right). \tag{3.29}$$

The scaled Gibbs-Thomson parameter used for the ice surface temperature is given by $\varepsilon = a^{-1/2} Re^{-1/2} D_{aw}^{1/2} \mathcal{T} \bar{E}$. A farfield decay condition for each variable, such as $T_\xi(\xi = \pm\infty, \eta, \bar{\tau}_4) = 0$ for temperature, is used to numerically update the boundary values. Within ice, a similar decay condition is used at $\eta = -\infty$ for temperature. The Stefan condition for the perturbation problem is found to be

$$D_{iw} \frac{\partial \bar{F}_{ice}}{\partial \bar{\tau}_4} \;=\; \frac{\mathcal{K} C_{ai} Ste}{\mathrm{Pr}} \left[K_{iw} \left\langle \left(\bar{T}_\eta\right)_{ice} \right\rangle_{1,2,3} - \left\langle \left(\bar{T}_\eta\right)_{water} \right\rangle_{1,2,3} \right],$$

where the heat flux in water is $\left\langle \left(\bar{T}_\eta\right)_{water} \right\rangle_{1,2,3} = (1/\mathcal{K}) \left(\bar{T}_\eta\right)_{air} - (\mathcal{L}\mathrm{Pr})/(\mathcal{K} a^{1/2} C_{aw})$ $[\mp 1 - \hat{T}_{impact}] \beta_{CE} \left[\bar{U}_{drop} \bar{F}_{ice,\xi} + i\bar{\beta} \bar{W}_{drop} \bar{F}_{ice} \right]$. The droplet velocities are given by $\bar{U}_{drop} = v_{1,d} / |v_d|$and $\bar{W}_{drop} = v_{3,d} / |v_d|$. The parameter '$a$' remains in the equations as a part of the term for water droplet impacts. Since the objective of this study is to compute the growth rates of the unstable ice surface for the non-parallel Hiemenz flow without simplifications, i.e. including coefficients of the form $\xi f(\eta)$, the evolution of the ice surface is computed as an initial value problem. The temporal growth computed from the Stefan condition is used to obtain a numerical estimate of the growth rate.

3.8 Numerical solution

A second order accurate central difference scheme is used to solve the airflow and the heat conduction equation within ice in order to obtain heat fluxes at the ice interface. Fictitious time stepping within the airflow and the ice is used to stabilize the solution when grid stretching is used. A pressure-correction approach with marker-and-cell method is used at the ice surface for pressure. A second order finite difference expression is used for Eq. 3.27 at the ice surface with a second order one-sided difference for $\bar{P}_\eta$ and a central difference expression for $\bar{V}_{\eta\eta}$. Continuity is enforced by taking $i\bar{\beta}\bar{W} = 0$ at the ice surface, which leads to $\bar{U}_\xi + \bar{V}_\eta = 0$. A third order finite difference expression for $\bar{V}_\eta$ and a second order central difference for $\bar{U}_\xi$ is then used for continuity. The boundary condition for pressure at the ice surface is specified by combining these conditions and eliminating the velocity at a fictitious point within the ice surface (see Tannehill *et al* [54], for example). The airflow and the energy equation in ice are both computed in a quasi-steady manner with the perturbed ice surface as an input. A third-order TVD Runge-Kutta scheme is then used to compute the temporal evolution of the ice surface.

3.9 Parameter space

The inputs required for the solution of the initial value problem of Section 3.7 are the scaled Mach number m_∞, the film inertia parameter $\mathcal{K}$, the Gibbs-Thomson parameter $\bar{E}$, the scaled ice height $\bar{H}_{ice}$, the ice/water conductivity ratio K_{iw}, the specific heat ratios C_{ai}, C_{aw} and the scaled Stefan number Ste. In order to estimate these input parameters, it becomes necessary to select a set of conditions which are representative of aircraft icing. Starting from these conditions, the parameters such as m_∞ may be varied in order to assess their effect on the stability of the stagnation line. These parameters are computed from free-stream conditions as well as known properties of water and ice. Some key physical properties, such as the surface tension of water, the density and latent

heat capacity of ice, are

$$\sigma^* = 7.56 \times 10^{-2}\,\mathrm{N/m},\ \rho^*_{ice} = 917\,\mathrm{kg/m^3},\ H^*_{ice/water} = 3.333 \times 10^5\,\mathrm{m^2/s^2(J/kg)}.$$

For air, the specific heat ratio and the Prandtl number are $\gamma = 1.4$ and $\mathrm{Pr} = 0.72$, respectively. Based on observations of the change in the heat flux within the Hiemenz flow due to m_∞ (see Fig. 3.9), a base condition is selected close to $m_\infty = \sqrt{2/(\gamma-1)}$ which divides the heat flux from air between cooling for $m_\infty < \sqrt{2/(\gamma-1)}$ and heating for $m_\infty > \sqrt{2/(\gamma-1)}$. A suitable set of free-stream conditions, wing chord length and base ice height are

$$T_\infty = 269\,\mathrm{K},\ V_\infty = 82\,\mathrm{m/s},\ P_\infty = 1.01325 \times 10^5\,\mathrm{Pa},\ C^* = 0.63\,\mathrm{m},\ f^*_{ice} = 11\,\mathrm{cm}.$$

Here the wing is chosen to be a NACA 0012 airfoil with chord length C^* and a nose radius of curvature $0.01586 \times C^*$ i.e. $a = 0.01586$ (see Abbott and Doenhoff [55]) . Given the above values, the non-dimensional parameters are found to be

$$Re = 4.847 \times 10^6, \quad M_\infty = 0.2494, \quad \sigma = 54.2589, \quad \mathfrak{T} = 0.0152, \quad D_{aw} = 0.00131.$$

The Reynolds number is calculated based on the chord length and is large, consistent with the high Reynolds number limit. The conductivity ratio of ice and water, the specific heat ratios of air and ice, and air and water, as well as the Stefan number are

$$K_{iw} = 4.021, \quad C_{ai} = 0.4808, \quad C_{aw} = 0.241, \quad Ste = 1.6892.$$

Since free-stream conditions such as T_∞ only vary within a small range for the aircraft icing problem, the parameters K_{iw}, C_{ai}, C_{aw} and Ste remain approximately constant. In the present formulation, the water film acts only as a passive conducting medium. Since

the film thickness is asymptotically smaller than $\mathcal{O}(Re^{-1/2})$, the surface tension of the water film does not appear in the ice stability computations. The film inertia parameter $\mathcal{M}(= 4.411)$ influences the shape of the water film, but does not affect the ice shape and does not appear in the computations. This is different from the computations of Tsao and Rothmayer [41, 42, 43, 44] and Rothmayer [45], which include the role of film thickness. For computing the Gibbs-Thomson parameter $\varepsilon = \gamma^*_{ice/water}/(\rho^*_{ice} H^*_{ice/water} L)$, the non-dimensionalising length L should be taken with respect to the same length scale as the Reynolds number. The appropriate length scale is the nose radius of curvature, where $a^{1/2}Re^{1/2}$ is the nose radius based Reynolds number. The scaled parameters such as the film inertia parameters needed for the stability computations are found to be

$$m_\infty = 2.0235,\ \mathcal{K} = 0.8597,\ \bar{E} = 0.0113,\ \bar{H}_{ice} = 100.5309.$$

Starting from these baseline values, the parameters given above are varied over a range of values to study their effect on the ice surface stability.

3.10 Results and discussion

A grid is selected for the linearized computations in both air and ice, such as the one for airflow shown in Fig. 3.11. The effect of the wave number $\bar{\beta}$ is evaluated by computing the linearized problem over a range of wave numbers. In all calculations, the scaled temperature $\hat{T}_{airfoil}$ is fixed to be 0, which implies a cold airfoil which is fixed at the free-stream temperature. A sample of a typical grid independence check for the linearized computations is made by comparing the solution of the normalised perturbation ice surface at $\bar{\tau}_4 = 5.2$ in Fig 3.12. Typical grid sizes are $n_x = 121 \leftrightarrow 401$, $n_y = 51 \leftrightarrow 61$ for the linearized airflow and $n_x = 121 \leftrightarrow 401$, $n_y = 101$ for the ice with uniform grid stretching in the y-direction. The domain sizes are typically

$\xi = [-15, 15] \leftrightarrow \xi = [-25, 25]$ and $\eta = [0 : 10]$ for the airflow.

An initial condition for the ice shape is specified (as in Fig. 3.12) and the linearized airflow as well as the heat conduction within the ice are computed, and these are used to obtain the heat fluxes within the air and ice to compute the evolution of the ice shape with time. A typical solution for the ice shape for $m_\infty = 0.0$, $\bar{E} = 0.0113$, $\bar{H}_{ice} = 100.53$ is shown in Fig. 3.13 where the non-parallel growth of the ice surface is seen. The local growth rate of this ice surface with streamwise location ξ is shown in Fig. 3.14, which also exhibits this non-parallel behavior. It becomes necessary to define the global growth rate for given input conditions while taking into account this non-parallel growth of the ice surface, where the growth rate is defined at the spatial peak of the disturbance (as shown in Fig. 3.14), i.e.

$$\omega = \left| \frac{\partial \bar{F}_{ice}}{\partial \bar{\tau}_4} \right| / \left| \bar{F}_{ice} \right| .$$

Typical values of the linearized primitive variables $\bar{U}$, $\bar{V}$, $\bar{P}$ and $\bar{T}$ are shown in Fig. 3.15, which are normalized with respect to the maximum for each variable. The values of the temperature $\bar{T}$ as well as the vertical velocity $\bar{V}$ and the pressure $\bar{P}$ are symmetric in magnitude and opposite in sign with respect to the stagnation line which is at $\xi = 0$. The values of the streamwise velocity $\bar{U}$ are symmetric about the stagnation line.

In Fig. 3.16, multiple sinusoidal disturbances are used as the initial condition for the ice surface. Here, the domain size in ξ is $[-35, 35]$. It is seen that initially the outermost roughnesses grow while the roughnesses decay at the center of the disturbance field. The outermost perturbation on the ice surface grows with time, and gradually propagates both towards and away from the stagnation line. The observed diameters of the perturbations at maximum growth rate are $\mathcal{O}(Re^{-1/2})$. In a topview of the roughness field at $\bar{\tau}_4 = 12.4$ (Fig. 3.17), the typical diameter of these roughesses is about 4.0, about twice the boundary layer thickness for the Hiemenz flow. These dimensions qualitatively

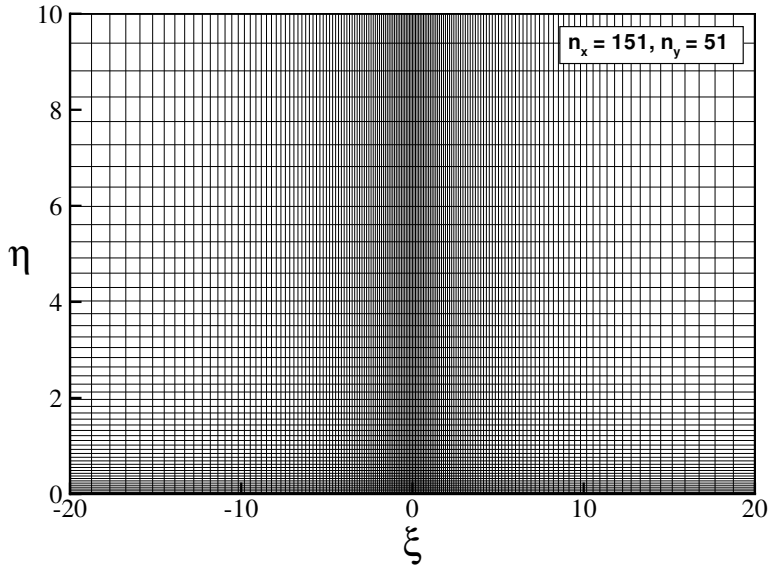

Figure 3.11 A typical grid used for the linearized computations in air.

agree with experimentally observed values of the roughness diameters (see Anderson, Hentschel and Ruff [1]).

A 6th order polynomial in $\bar{\beta}$ is fit to the growth rates using least squares for constant m_∞ and $\bar{E}$. If the 6th order polynomial is given by

$$p(\bar{\beta}) \quad = \quad a_0 + a_1\bar{\beta} + a_2\bar{\beta}^2 + a_3\bar{\beta}^3 + a_4\bar{\beta}^4 + a_5\bar{\beta}^5 + a_6\bar{\beta}^6,$$

the coefficients are given in Table 3.1 and the resulting polynomials are shown in Fig. 3.18. The zero growth rate wave numbers $\bar{\beta}_0$ computed from these curve fits are then used to create a neutral curve using a polynomial in powers of m_∞^2 (see Fig. 3.19), which is found to be

$$\bar{\beta}_0(m_\infty) = 3.4501 - 0.4192m_\infty^2 + 0.0288m_\infty^4 - 0.0188m_\infty^6.$$

The increase in the scaled Mach number m_∞ produces a stabilizing effect on the

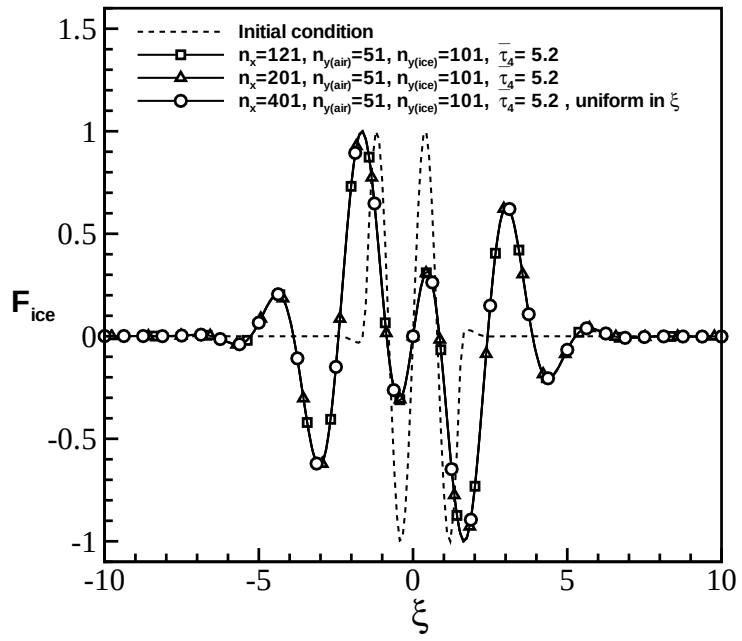

Figure 3.12 A typical grid independence check for the perturbation ice surface. F_{ice} is normalized with respect to maximum height.

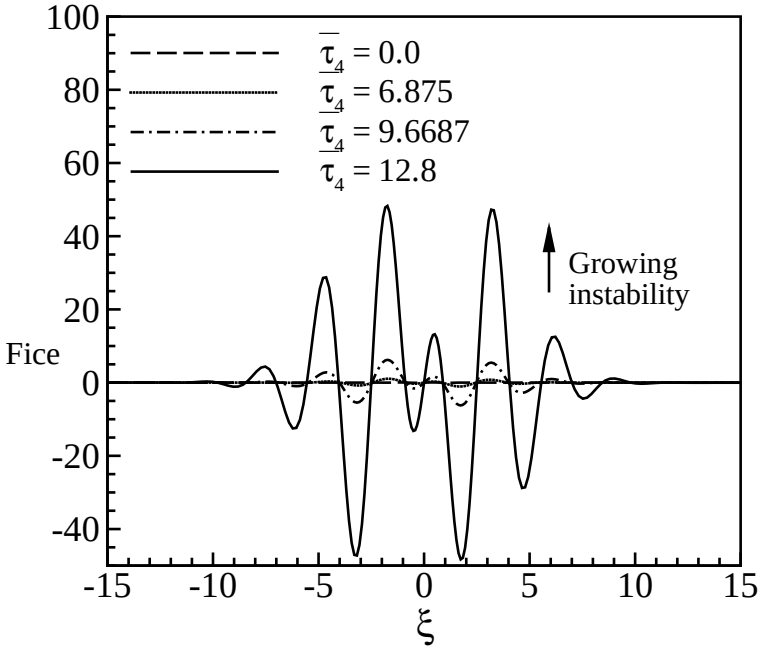

Figure 3.13 Typical growth of the ice surface, showing the non-parallel behavior.

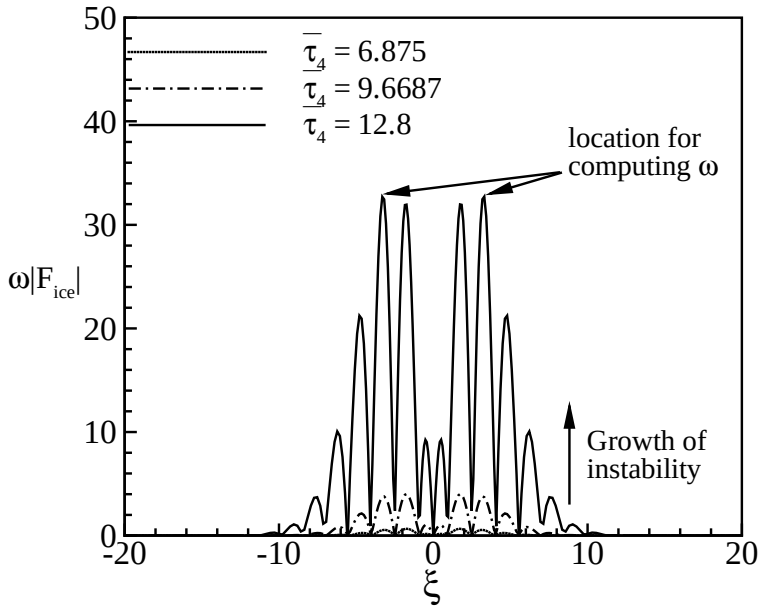

Figure 3.14 Typical speed of the ice surface growth, showing the non-parallel behavior.

Table 3.1 Coefficients of the curve fit for growth rate with wave number for different values of m_∞.

m_∞	a_6	a_5	a_4	a_3	a_2	a_1	a_0
0	0.0002	-0.0006	-0.0082	-0.0241	0.1633	-0.1654	0.7556
1	-0.0011	0.0189	-0.1187	-0.2711	-0.2454	-0.0801	0.5049
1.5	-0.0010	0.0157	-0.0875	0.1518	-0.0933	0.0157	0.2675
2.0235	-0.0006	0.0078	-0.0337	0.0078	-0.0051	-0.0051	0.0228

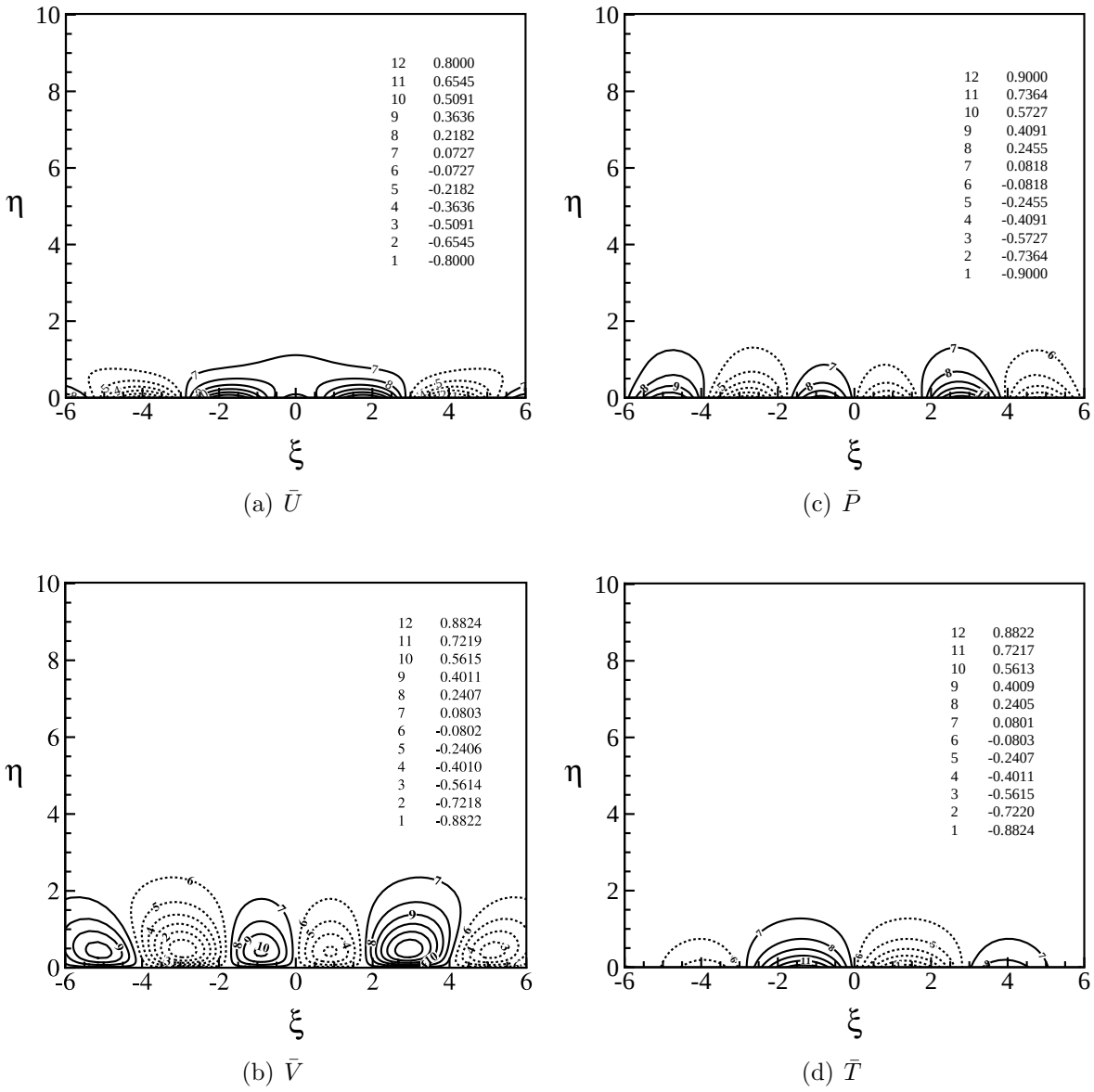

Figure 3.15 Linearized primitive variables at $\bar{\tau}_4 = 31.8$ for $m_\infty = 0.0$, $\bar{\beta} = 1.5708$ (a) streamwise velocity, $\bar{U}$, (b) vertical velocity, $\bar{V}$, (c) pressure, $\bar{P}$, and (d) temperature, $\bar{T}$.

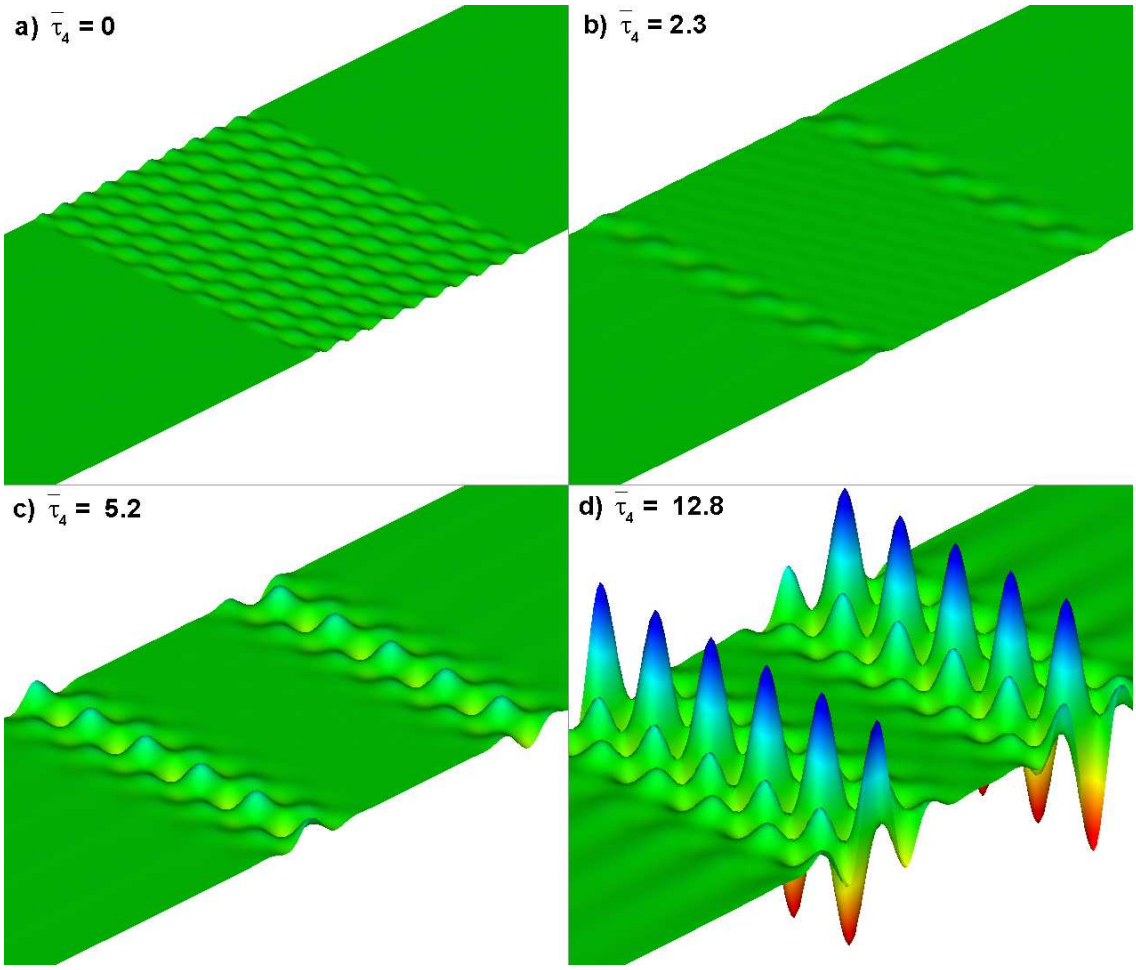

Figure 3.16 Typical temporal evolution of the ice surface instability. The outermost disturbance grows the fastest and the disturbances display a strong dependence on ξ.

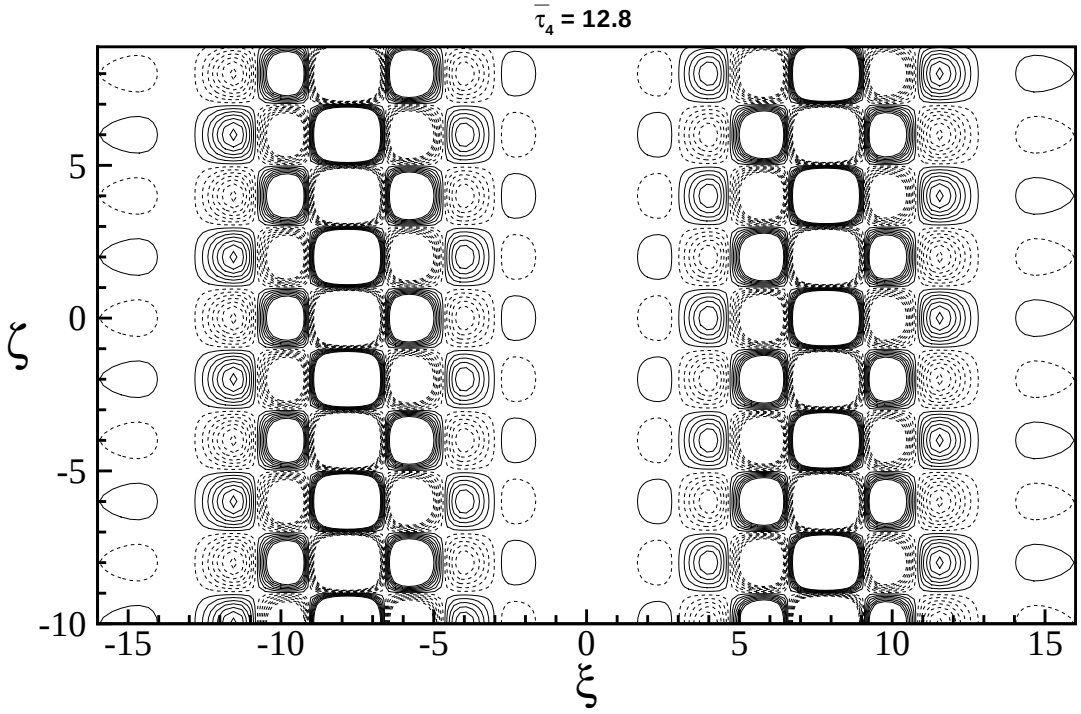

Figure 3.17 Top view of the ice surface height at $\bar{\tau}_4 = 12.8$ (from Fig 3.16). The solid lines are positive contour values and the dashed lines are negative contour values.

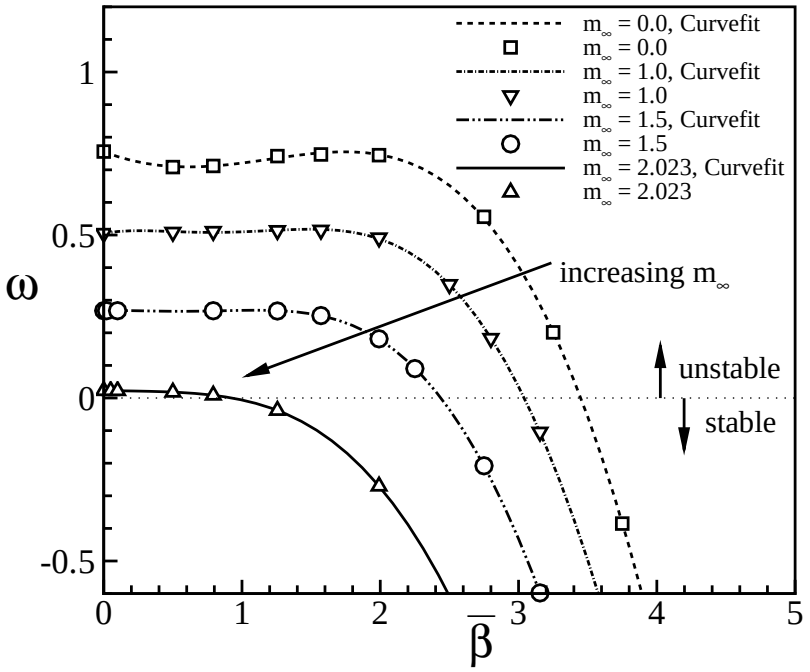

Figure 3.18 Typical dependence of the computed growth rate on m_∞ with $\bar{E} = 0.0113$.

disturbances. Increasing m_∞ corresponds to an increase in the subfreezing stagnation total temperature. As m_∞ increases and the free-stream stagnation temperature becomes closer to freezing, the reduced heat flux from the air has a stabilizing effect on the ice surface (see Figs. 3.10 and 3.18). In Fig. 3.19, the zero growth wave number $\bar{\beta}_0$ is plotted against the scaled Mach number m_∞. It may be seen that the wave number $\bar{\beta}_0$ has a strong dependence on the Mach number. At low Mach numbers, the disturbances are predominantly three-dimensional and higher Mach numbers lead to predominantly two-dimensional disturbances as indicated by the values of $\bar{\beta}_0$ in Fig. 3.19. The Gibbs-Thomson parameter $\bar{E}$ also suppresses instabilities in the ice surface (see Fig 3.20). An increase in $\bar{E}$ leads to more stable and two-dimensional disturbances.

In the low Mach number stagnation flow of this study, the heat flux does not vary with streamwise distance. However, in the boundary layer formulation of Rothmayer [48] (also see Otta and Rothmayer [56]), a cooling effect of the heat flux from airflow

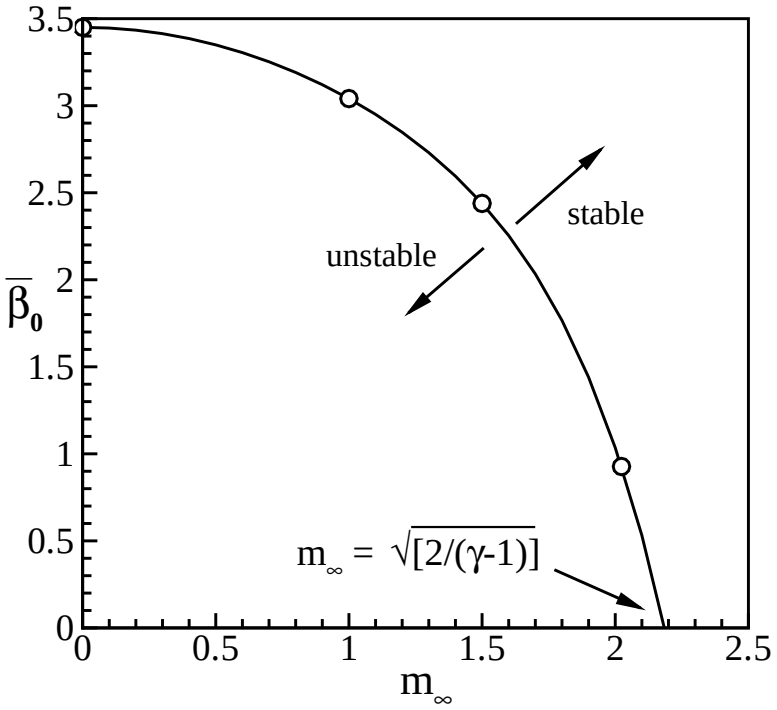

Figure 3.19 A typical neutral curve for stability showing the dependence on the parameter m_∞.

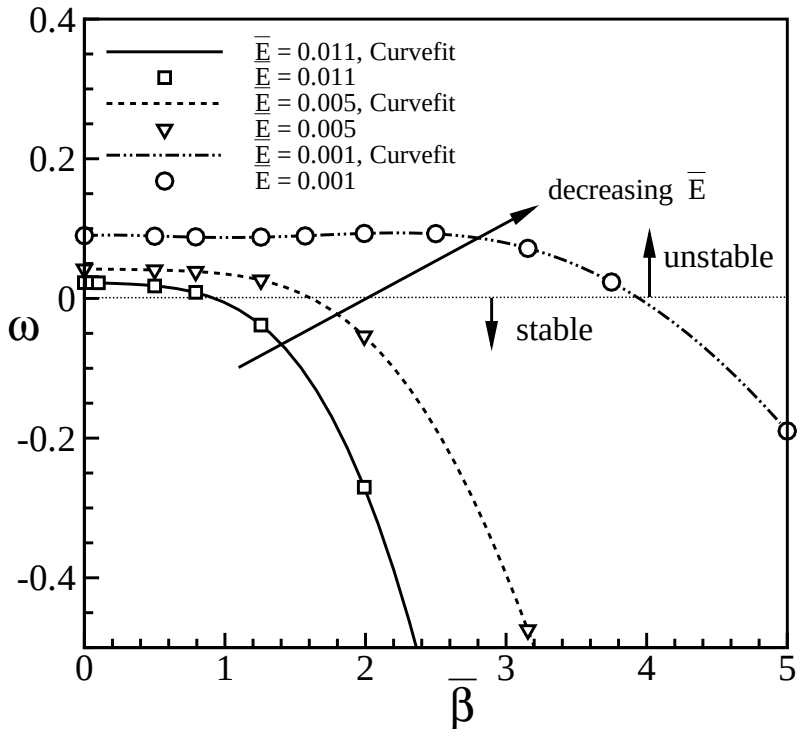

Figure 3.20 Typical dependence of computed growth rate on $\bar{E}$ with $m_\infty = 2.0235$.

occurs with streamwise distance. In the present formulation, smaller m_∞ with a higher cooling heat flux increases the instability of the ice surface.

CHAPTER 4. ICE SURFACE INSTABILITIES IN SWEPT WING ATTACHMENT LINE FLOW

4.1 Overview of swept wing icing

The attachment line flow over a swept wing consists of the flow along the attachment line, i.e. in the spanwise direction of the wing, as well as flow outward from the attachment line. Ice accretion in this swept wing attachment line flow is different from unswept ice accretion. As the sweep angle increases, the ice formation over swept wings becomes more and more three-dimensional. High sweep angles eventually produce complex ice structures which make the ice formation discontinuous along the span of the wing. These ice structures are called "scallops", "cups" or "lobster tails" (see Vargas [57]). This situation is different from ice formation on unswept wings, which is primarily two-dimensional along the span of the wing. Since these three-dimensional ice shapes strongly affect the airflow near the leading edge, it is important to understand the mechanisms which produce both the ice roughness elements and the larger ice shapes which eventually emerge from the roughness. So far, experiments have been the main source of information about these processes.

The first observations of the differences between unswept and swept wing ice formations came from the study of Von Glahn and Gray [58]. They observed that while the unswept glaze ice accretion was similar in different spanwise locations, glaze ice accretion for swept wings was broken up in the spanwise direction, producing a row of "nested cups". Later experiments on ice accretion over swept wings made similar

observations about the discontinuous nature of these swept wing ice scallop formations. While conducting experiments aimed at developing an empirical correlation for ice accretion prediction, Blair [59] and Shah [60] observed that scallops are a defining feature in swept wing ice formation. Wilder [61] observed that the spacing between the scallops was larger for glaze ice accretions than for rime ice accretions. For fixed sweep angle, this separation decreased as the ice accretions tended towards rime, and eventually led to ice accretions without scallops for strongly rime cases. These observations were later confirmed by experiments in 1990s.

The question that needs to be answered is : what are the differences between the underlying physical processes for swept and unswept wing ice accretion which leads to formation of scallops and strongly three dimensional ice shapes for swept wings? In 1996, Vargas and Reshotko [34, 35, 36] conducted a series of experiments for ice formation over swept wings in the NASA Glenn Icing Research Tunnel. This was the most extensive study undertaken for ice accretion over swept wings and led to some important observations (see Vargas [57] for a review of these studies). Vargas and Reshotko [34, 35, 36] showed that scallop formation is governed by local effects on roughness elements. The final ice structures depend on the interactions between the initial roughness elements. In the study of Vargas and Tsao [2], for example, it was directly observed that the larger scale glaze feathers grew out of the initial glaze roughness elements. The ice formation consists of two separate zones - the attachment line zone with roughness elements and the ice feather zone relatively far away from the attachment line, which starts at a certain distance d_{cr} from the attachment line and beyond which the ice feathers are seen to occur. Ice feathers are long thin structures which start from a nucleation site on the surface and gradually grow into the airflow. These feathers can be both rime or glaze, depending on the flow conditions. The critical distance d_{cr} is found to be an important parameter in determining whether scallops form. Three different ice formations are observed : complete scallops (see Fig. 4.1), incomplete scallops (where

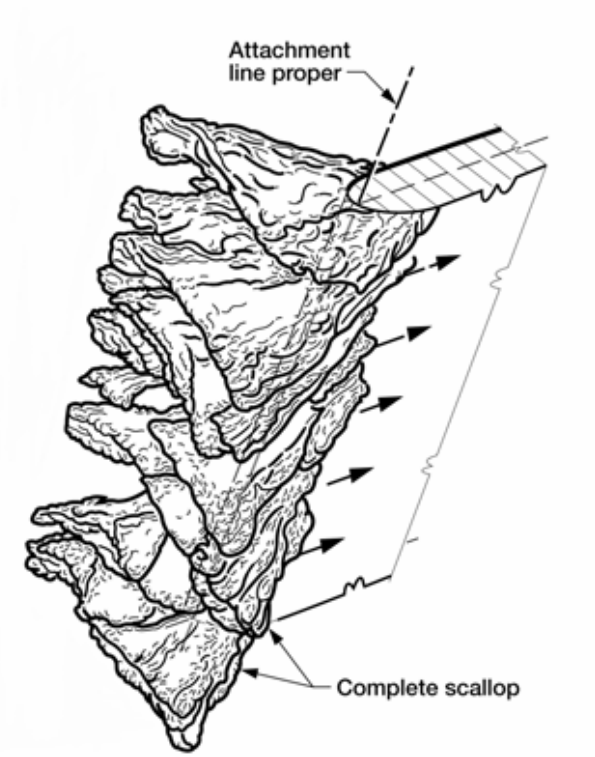

Figure 4.1 Scallop formation on a swept wing (reproduced from Vargas, Tsao and Rothmayer [4] with permission).

there is a partial formation of the spanwise discontinuous structures), and no-scallops (where the ice feathers are covered by ice growth in the attachment line zone). When the critical distance is zero, the ice surface is completely covered with glaze ice feathers. These ice feathers lead to ridges and eventually scallops or incomplete scallop formation depending on flow conditions. Lower sweep angles witness a lack of scallop formation or incomplete scallop formation. As the sweep angle increases, the critical distance d_{cr} decreases rapidly and the physical processes leading to scallop formation become more dominant. It should be noted that modeling these strongly nonlinear effects is beyond the scope of the present study.

While experiments for ice accretion advance the understanding of the icing physics, it is equally important to have theoretical models for predicting swept wing ice accretion. In 1993, Hedde and Guffond [62] published results for one such approach to model

scallop formation. This is so far the only attempt at predicting scallop formation. In this model, there are two separate phases namely, scallop initiation and macroscopic growth. The initiation is modeled by assuming complete freezing of droplets on impact. The modeling of the macroscopic growth assumes that there are regions of high heat transfer with complete freezing of droplets and regions of low heat transfer where there is residual water. The spacing of the scallops is explained by the shadowing of the droplet trajectories. The experiments so far have suggested that scallops form from feathers and roughness elements (see Vargas [57]). However, the shadowing effect of droplet trajectories may play a significant role in the later stages of scallop formation. Reshotko, Vargas and Reed [63] investigated the possible influence of cross-flow instability on the formation of scallops. Growth rates of the cross-flow instability with sweep angle were superimposed with the change in the critical distance. The rapid decrease of the critical distance beyond a sweep angle of 25^o followed the trends of rapid increase in growth rate of the cross-flow instability. However, the studies of Hedde and Guffond [62] and Reshotko, Vargas and Reed [63] do not include the details of the ice surface growth. In order to eventually develop modeling capability for swept wing ice formations, it is important to understand the properties of the interaction between the ice surface and the airflow in order to explain the formation of roughnesses and the ice structures which grow out of these roughnesses.

The present chapter extends the formulation given in Section 3.5 to include cross flow with small sweep angles in order to study the instability of an ice surface near the attachment line of a swept wing for the conditions of in-flight glaze icing, where the roughness size in all three spatial dimensions is $\mathcal{O}(Re^{-1/2})$ (see Figs. 4.2 and 4.3).

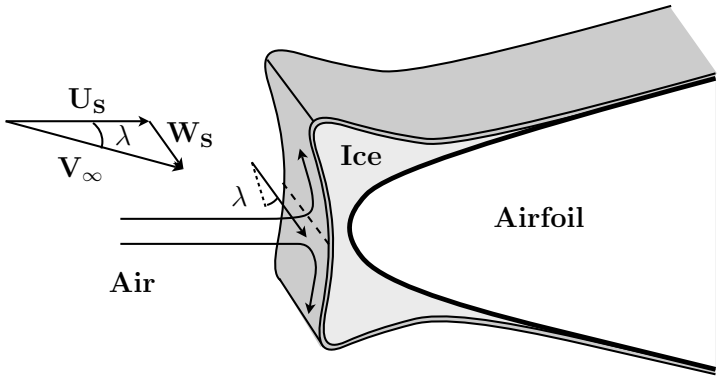

Figure 4.2 Simplified ice surface on an airfoil showing the sweep angle, λ.

4.2 Assumptions and scalings for swept wing stagnation icing

For the swept stagnation flow shown in Fig. 4.2, the free-stream velocity is split into a velocity component normal to the attachment line, U_S, and a velocity component parallel to the attachment line, W_S. The components of the velocity may be written in terms of the sweep angle as $U_S = V_\infty \cos\lambda$, and $W_S = V_\infty \sin\lambda$. As the sweep angle increases, W_S increases and so does its effect on the airflow and the ice surface behavior. In the small sweep angle limit, as $\lambda \to 0$, the velocity components are given as $U_S = V_\infty$ and $W_S \backsimeq V_\infty \lambda$. Since the velocities in the stagnation region near the leading edge of the wing are $\mathcal{O}(Re^{-1/2})$, it becomes necessary to consider the attachment line flow for small sweep angles $\lambda \ll 1$. In particular, the velocity magnitude along the attachment line is $\mathcal{O}(\lambda)$, and for this velocity to interact with the $\mathcal{O}(Re^{-1/2})$ velocity in the stagnation region the sweep angle must be $\lambda \sim \mathcal{O}(Re^{-1/2})$.

4.3 Swept wing stagnation line icing model

The stagnation line icing model for the swept wing is similar in structure to the stagnation line icing when the flow along the attachment line is absent and differs from this model only due to the flow along the attachment line. Therefore, the expansions

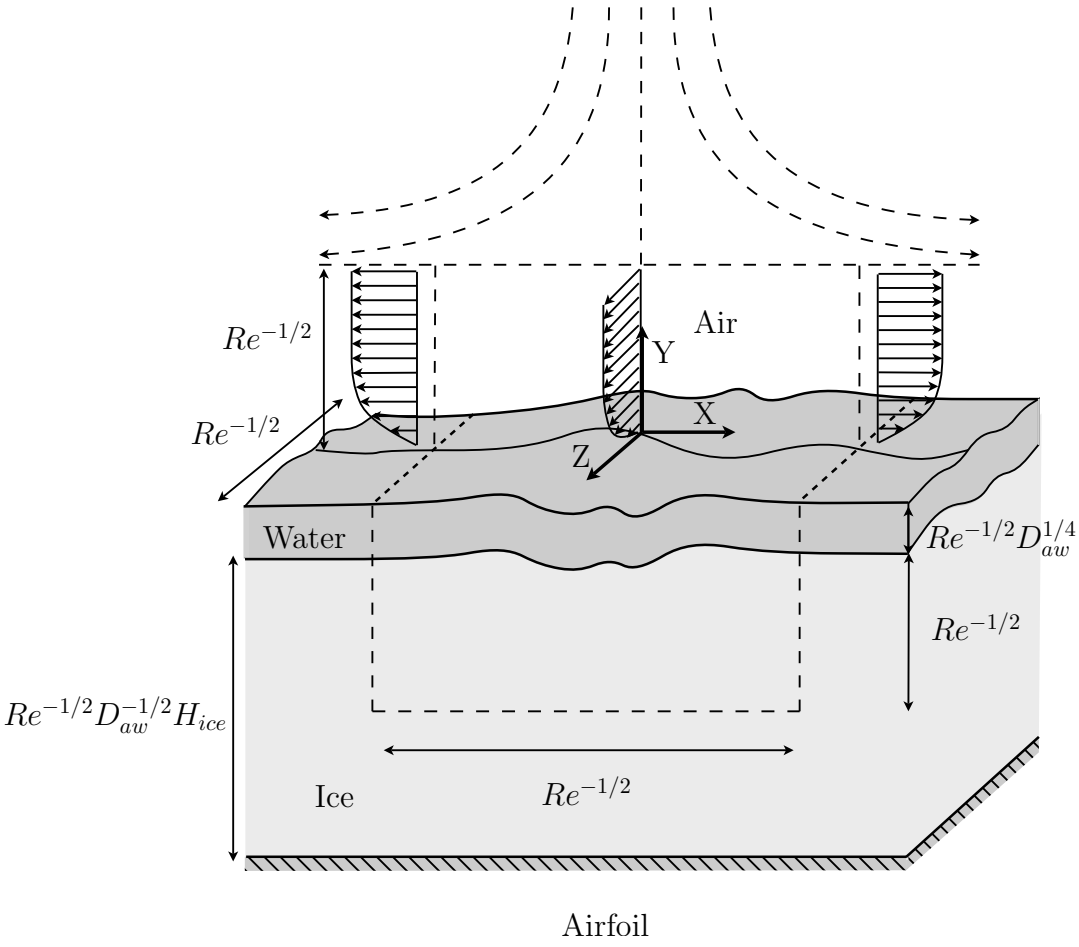

Figure 4.3 Scales and geometry of the swept wing attachment line flow.

for the airflow, the water film and the ice are identical to the expansions mentioned in Section 3.4, where a thin water film uniformly covers the ice surface. The coordinate system for the airflow and the ice is given by

$$(x, y, z) = (0, Re^{-1/2} D_{aw}^{-1/2} H_{ice}, 0) + Re^{-1/2}(X, Y, Z).$$

The leading order Hiemenz flow along the attachment line is given by $W_H(\eta)$. The streamwise and vertical velocities, pressure and temperature of the Hiemenz flow are given by $U_H(\eta), V_H(\eta)$, $P_H(\xi, \eta)$, and $T_H(\eta)$, respectively (see Section 3.6). As noted above, the flow along the attachment line is controlled by the sweep angle, which is

$$\lambda = Re^{-1/2}\Lambda. \tag{4.1}$$

The inviscid slip velocity at the edge of the boundary layer (the component of the free-stream velocity along the spanwise direction) then becomes

$$W_H(\infty) = \Lambda.$$

As in case of stagnation line icing, the water film is purely conducting and passively transmits the heat flux between the air and ice, so long as the ice is completely wetted (see Eq. 3.14). This also implies that the computation of the airflow and the heat conduction within ice is enough to study the evolution of the ice surface. For details on the multiple scales analysis as well as the final equations for the airflow, the heat conduction within ice and the Stefan condition describing the growth of the ice surface, see Section 3.5. In the multiple scales model with a thin water-film , the averages are given by $<>_{i,j}$ and $<>_{i,j,k}$ where the indices $i = 1, 2, 3$ denote the time scales in air and water (details on the multiple scales analysis as well as the final equations for the airflow may be found in Section 3.5 and 3.5). The conclusions of this multiple scales model is

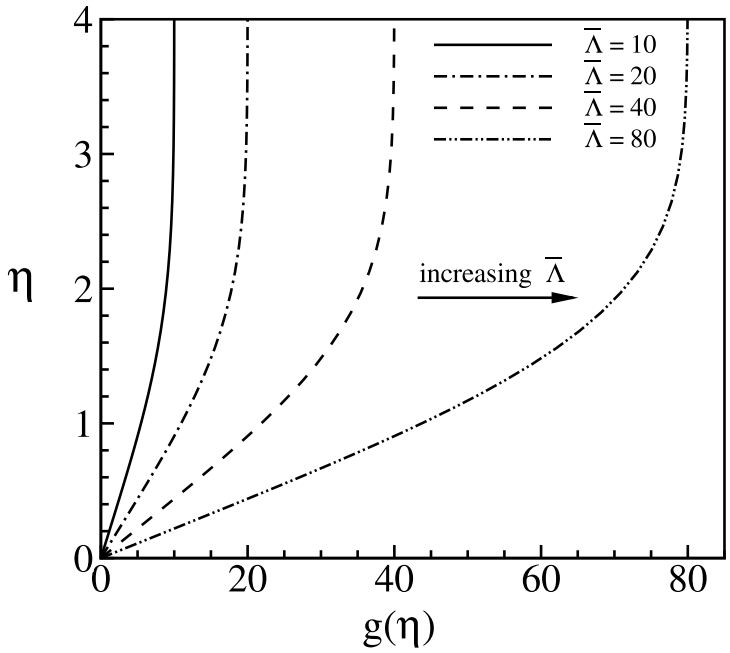

Figure 4.4 Solution for the velocity along the attachment line.

then applied to swept wing stagnation flow to construct the linearized flow equations for stability analysis of the ice surface (see Section 4.5).

4.4 Swept wing Hiemenz flow

Near the attachment line at the leading edge of the wing, the airflow consists of a stagnation flow in a plane normal to the attachment line and flow along the attachment line (see Fig. 3.6 where the flow along the attachment line is into the plane of the surface). The coordinate transformation for this airflow to the stagnation region of a parabolic leading edge is given by $(X, Y, Z) = a^{-1/2}(\xi, \eta, \zeta)$, where a is the nose radius of curvature of the airfoil. The solution of this airflow is obtained by considering the stagnation flow as in Section 3.6. The solution for the streamwise as well as the vertical velocities are obtained using Eq. 3.17. The equation for the energy equation in air also remains the same and is given by 3.18. The spanwise velocity in air, $W_H(\eta) = \sqrt{a}g\,(\eta)$,

is obtained from

$$g''(\eta) + f(\eta)\, g'(\eta) = 0, \tag{4.2}$$

for which the boundary conditions are $g(0) = 0$, $g(\infty) = a^{-1/2}\Lambda = \bar{\Lambda}$. This scaled sweep angle parameter $\bar{\Lambda}$ is related to the sweep angle seen by the attachment line λ through $\bar{\Lambda} = Re^{1/2}a^{1/2}\lambda$. As the sweep angle increases, the velocity component for the flow along the attachment line increases (see Fig 4.4). The heat conduction within the ice sheet also remains the same as in Section 3.6.

4.5 Stability analysis

The evolution of the ice surface is computed as an initial value problem for small perturbations where the leading order ice surface is growing uniformly due the heat flux from the airflow and the heat flux within ice (also see Section 3.7). The leading order ice growth is given by Eq. 3.19 over which the solution for the swept wing Hiemenz flow is obtained (see previous section 4.4). The airflow is a small perturbation on this Hiemenz flow:

$$\begin{aligned}\left\langle \{U, V, W, P, \hat{T}\} \right\rangle_{1,2,3} &\sim \{U_H(\xi,\eta), V_H(\xi,\eta), W_H(\eta), P_H(\xi,\eta), T_H(\eta)\} \\ &+\varepsilon\{a^{1/2}\bar{U}(\xi,\eta,\bar{\tau}_4), a^{1/2}\bar{V}(\xi,\eta,\bar{\tau}_4), a^{1/2}\bar{W}(\xi,\eta,\bar{\tau}_4), a\bar{P}(\xi,\eta,\bar{\tau}_4), \bar{T}(\xi,\eta,\bar{\tau}_4)\}e^{i\bar{\beta}\zeta} + \dots,\end{aligned}$$

where $\bar{\beta} = a^{-1/2}\beta$ and β is the spanwise wave number in Z. This is different from the stagnation line flow in Section 3.7 only because $W_H(\eta) > 0$. The temperature inside ice and the ice height are taken to be

$$\left\langle \{\hat{T}_{ice}, f_{ice}\} \right\rangle_{1,2,3} \sim \{T_S(\eta), F_{ice}(\bar{\tau}_4)\} + \varepsilon\{\bar{T}(\xi,\eta,\bar{\tau}_4), a^{-1/2}\bar{F}_{ice}(\xi,\bar{\tau}_4)\}e^{i\bar{\beta}\zeta} + \dots.$$

The continuity equation is given by

$$\bar{U}_\xi + \bar{V}_\eta + i\bar{\beta}\bar{W} = 0.$$

The equations for the perturbation quantities in the transformed coordinates are found to be

$$\begin{aligned}
\xi f'(\eta)\bar{U}_\xi + \bar{U}f'(\eta) - f(\eta)\bar{U}_\eta + \bar{V}\xi f''(\eta) & \\
+i\bar{\beta}g(\eta)\bar{U} &= -\bar{P}_\xi + \bar{U}_{\xi\xi} + \bar{U}_{\eta\eta} - \bar{\beta}^2\bar{U}, \qquad (4.3)\\
\xi f'(\eta)\bar{V}_\xi - f(\eta)\bar{V}_\eta - \bar{V}f'(\eta) + i\bar{\beta}g(\eta)\bar{V} &= -\bar{P}_\eta + \bar{V}_{\xi\xi} + \bar{V}_{\eta\eta} - \bar{\beta}^2\bar{V}, \qquad (4.4)\\
\xi f'(\eta)\bar{W}_\xi - f(\eta)\bar{W}_\eta + \bar{V}g'(\eta) + i\bar{\beta}g(\eta)\bar{W} &= -i\bar{\beta}\bar{P} + \bar{W}_{\xi\xi} + \bar{W}_{\eta\eta} - \bar{\beta}^2\bar{W}, \qquad (4.5)
\end{aligned}$$

where the effect of sweep comes into play through $g(\eta)$. The energy equation becomes

$$\xi f'(\eta)\bar{T}_\xi - f(\eta)\bar{T}_\eta + \bar{V}T'_H + i\bar{\beta}g(\eta)\bar{T} = \mathrm{Pr}^{-1}(\bar{T}_{\xi\xi} + \bar{T}_{\eta\eta} - \bar{\beta}^2\bar{T}). \qquad (4.6)$$

The Poisson equation for the perturbation pressure is derived using the continuity equation and z-momentum equation and is found to be

$$-2f'(\eta)\bar{U}_\xi - 2\xi f''(\eta)\bar{V}_\xi + 2f'(\eta)\bar{V}_\eta - i2\bar{\beta}g'(\eta)\bar{V} = \bar{P}_{\xi\xi} + \bar{P}_{\eta\eta} - \bar{\beta}^2\bar{P}. \qquad (4.7)$$

The remaining equations are the same as those used for the unswept stagnation line, but are listed here for completeness. In order to solve the above linearized equations for the airflow, the boundary conditions at the edge of the boundary layer are taken to be

$$\bar{U} = 0, \quad \bar{V} = 0, \quad \bar{T} = 0, \quad \bar{P} = 0.$$

The boundary conditions for the linearized perturbation air momentum equations at the ice surface are

$$\bar{U}\left(\xi,0,\bar{\tau}_4\right) = -\xi f''\left(0\right)\bar{F}_{ice}\left(\xi,\bar{\tau}_4\right), \tag{4.8}$$

$$\bar{V}\left(\xi,0,\bar{\tau}_4\right) = f'\left(0\right)\bar{F}_{ice}\left(\xi,\bar{\tau}_4\right) = 0, \tag{4.9}$$

$$\bar{W}\left(\xi,0,\bar{\tau}_4\right) = -g'(0)\bar{F}_{ice}\left(\xi,\bar{\tau}_4\right), \tag{4.10}$$

and the boundary condition for the energy equation becomes

$$\bar{T}\left(\xi,0,\bar{\tau}_4\right) = -\hat{T}'_H\left(0\right)\bar{F}_{ice}\left(\xi,\bar{\tau}_4\right). \tag{4.11}$$

The boundary condition for pressure is given by

$$0 = -\bar{P}_\eta + \bar{V}_{\eta\eta}. \tag{4.12}$$

Within the ice, the equation for the perturbation temperature becomes

$$\bar{T}_{\xi\xi} + \bar{T}_{\eta\eta} - \bar{\beta}^2\bar{T} \;\; = \;\; 0. \tag{4.13}$$

At the water/ice interface, the perturbation temperature inside the ice is found to be

$$\bar{T}\left(\xi,0,\bar{\tau}_4\right) = -\bar{F}_{ice}\left(\xi,\bar{\tau}_4\right)T_{S,\eta}(0) + \bar{E}\bar{F}_{ice,\xi\xi}\left(\xi,\bar{\tau}_4\right) - \bar{E}\bar{\beta}^2\bar{F}_{ice}\left(\xi,\bar{\tau}_4\right), \tag{4.14}$$

where the scaled Gibbs-Thomson parameter is the same as in Section 3.7. After examining the Stefan condition, it is found that the ice time scale can be transformed to give $\bar{\tau}_4 = a\tau_4$. The Stefan condition for the perturbation problem is then found to be

$$D_{iw}\frac{\partial\bar{F}_{ice}}{\partial\bar{\tau}_4} \;\; = \;\; \frac{\mathcal{K}C_{ai}Ste}{\mathrm{Pr}}\left[K_{iw}\left(\bar{T}_\eta\right)_{ice} - \left(\bar{T}_\eta\right)_{water}\right], \tag{4.15}$$

where the heat flux in water is given by $\left(\bar{T}_\eta\right)_{water} = \frac{1}{\mathcal{K}}\left(\bar{T}_\eta\right)_{air} - \frac{\mathcal{L}\mathrm{Pr}}{\mathcal{K}a^{1/2}C_{aw}}\left[\mp 1 - \hat{T}_{impact}\right]\beta_{CE}$ $\left[\bar{U}_{drop}\bar{F}_{ice,\xi} + i\bar{\beta}\bar{W}_{drop}\bar{F}_{ice}\right]$.

In the absence of the sweep velocity, the real and imaginary mode shapes may be found separately and it suffices to compute the linearized equations for real mode shapes. However, the presence of the sweep velocity makes it necessary to compute both the real and imaginary mode shapes in a coupled manner. Furthermore, it is not possible to remove the sweep angle parameter $\bar{\Lambda}$ from the linearized equations for the airflow as can be done for the stagnation strength parameter a.

4.6 Numerical Solution

The linearized equations for the airflow are solved using a central difference scheme, which is second order accurate in η and fourth order accurate in ξ. Similarly, the Laplace equation for heat conduction within ice is solved using a second order accurate scheme. A higher order finite difference expression is chosen for terms in the equations with a coefficient of ξ such that second order accuracy is preserved with the chosen domain. This also implies that the domain size is limited by the largest ξ and its influence on the finite difference scheme. Using the fourth order central difference scheme, the expression for $\bar{U}_\xi$ is

$$\frac{\partial \bar{U}}{\partial \xi} = \frac{1}{12\Delta\xi}\left(\bar{U}_{i+2,j} - 8\bar{U}_{i+1,j} + 8\bar{U}_{i-1,j} - \bar{U}_{i-2,j}\right).$$

For the pressure-correction approach with marker-and-cell method at the ice surface, a second order finite difference expression is used for Eq. 4.12 at the ice surface with a second order one-sided difference for $\bar{P}_\eta$ and a central difference expression for $\bar{V}_{\eta\eta}$. Continuity is enforced by taking $i\bar{\beta}\bar{W}\left(\xi, 0\right) = -i\bar{\beta}g'(0)\bar{F}_{ice}$ at the ice surface, which leads to $\bar{U}_\xi + \bar{V}_\eta = i\bar{\beta}g'\left(0\right)\bar{F}_{ice}$ where a third order finite difference expression for $\bar{V}_\eta$ and

a fourth order central difference for $\bar{U}_\xi$ is used. The boundary condition for pressure at the ice surface is specified by combining these conditions and eliminating the velocity at a fictitious point within the ice surface, which becomes

$$-\frac{-3\bar{P}_{i,1}+4\bar{P}_{i,2}}{2\Delta\eta}+\frac{[J_3+3J_1]}{\Delta\eta^2}\bar{V}_{i,2}=\frac{-\bar{P}^g_{i,3}}{2\Delta\eta}+J_1\frac{\frac{1}{2}\bar{V}^g_{i,3}}{\Delta\eta^2}$$
$$-\frac{3J_1\left(\bar{U}^g_{i+2,j}-8\bar{U}^g_{i+1,j}+8\bar{U}^g_{i-1,j}-\bar{U}^g_{i-2,j}\right)}{12\Delta\xi\Delta\eta}+\frac{3J_1}{\Delta\eta}i\bar{\beta}g'(0)\,\bar{F}^g_{ice},$$

where g denotes the guess values for each ξ location and J_1, J_2, J_3 are the factors for grid stretching in η for $j = 1, 2, 3$ (see Appendix A). The airflow and the energy equation in the ice are both computed in a quasi-steady manner with the perturbed ice surface as an input which are then used to evaluate the heat fluxes at the ice surface. A third-order TVD Runge-Kutta scheme is then used to compute the evolution of the ice surface using the Stefan condition.

4.7 Parameter space for swept wing stagnation line icing

The inputs required for the solution of the initial value linearized stability analysis (see Section 4.5) are the scaled Mach number m_∞, the scaled sweep angle parameter $\bar{\Lambda}$, the Gibbs-Thomson parameter $\bar{E}$, the scaled ice height $\bar{H}_{ice}$, the film inertia parameter $\mathcal{K}$, the ice/water conductivity ratio K_{iw}, the specific heat ratios C_{ai}, C_{aw} and the scaled Stefan number Ste. The main new parameter in this section is the scaled sweep angle parameter $\bar{\Lambda}$. A set of free-stream conditions corresponding to in-flight aircraft swept wing icing as well as known properties of water and ice are used to estimate these input parameters. Some key physical properties, such as the surface tension of water, the density and latent heat capacity of ice, the specific heat ratio and the Prandtl number of air are the same as in Section 3.9. The flow conditions are chosen for a baseline solution to correspond to typical in-flight and experimental conditions for swept wing icing (see

Vargas and Reshotko [34]). A suitable baseline set of free-stream conditions, wing chord length and ice height are

$$T_\infty = 269.26\,\mathrm{K},\ V_\infty = 67.05\,\mathrm{m/s},\ P_\infty = 1.01325\times 10^5\,\mathrm{Pa},\ C^* = 0.38\,\mathrm{m},\ f^*_{ice} = 4.9\,\mathrm{cm}.$$

A wing with a NACA 0012 airfoil section is chosen as the reference for all of the attachment line solutions. This baseline solution also requires a sweep angle where a small angle assumption can be made. In experiments, sweep angle usually varies between 0^o and 45^o. Therefore, the base sweep angle is taken to be 5^o. Given the above values, the non-dimensional parameters are found to be

$$Re = 1.944\times 10^6,\quad M_\infty = 0.2038,\qquad \mathcal{T} = 0.0142,\quad D_{aw} = 0.00131.$$

The Reynolds number is calculated based on the NACA 0012 chord length, and is large, consistent with the high Reynolds number limit. The thermal conductivity ratio of ice and water, the specific heat ratios of air and ice, and air and water, as well as the Stefan number are

$$K_{iw} = 4.021,\quad C_{ai} = 0.481,\quad C_{aw} = 0.241,\quad Ste = 1.689.$$

For the range of variation for free-stream conditions such as T_∞, the parameters K_{iw}, $C_{ai}, C_{aw}$and Ste remain approximately constant. The Gibbs-Thomson parameter ε is computed as in Section 3.9. The scaled parameters needed for the stability computations are found to be

$$m_\infty = 1.7082,\ \mathcal{K} = 0.853,\ \bar{E} = 0.014,\ \bar{H}_{ice} = 51.90,$$

and

$$\bar{\Lambda} = 15.424.$$

Starting from these baseline values, the parameters given above are varied over a range of values to study their effect on the ice surface instability in the swept wing stagnation flow.

4.8 Results and discussion

The effect of the wave number $\bar{\beta}$ is evaluated by computing the linearized problem over a range of wave numbers. The sweep angle parameter $\bar{\Lambda}$ is changed as well to investigate the role of the airflow along the attachment line. The scaled Mach number m_∞ is changed to study the effect of heating in the presence of the attachment line flow. In all calculations, the scaled temperature $\hat{T}_{airfoil}$ is fixed to be 0, which implies a cold airfoil which is fixed at the free-stream temperature. An initial perturbation ice shape is used to start the computations. The ice surface evolves to give the ice shape $\bar{F}_{ice}(\bar{\tau}_4, \xi, \bar{\beta})$. The growth rates are obtained from these linearized computations, in which the growth rate ω is defined at the location ξ where $\left|\partial \bar{F}_{ice}(\bar{\tau}_4, \xi, \bar{\beta})/\partial \bar{\tau}_4\right|$ is maximum and

$$\omega = \left|\frac{\partial \bar{F}_{ice}}{\partial \bar{\tau}_4}(\bar{\tau}_4, \xi, \bar{\beta})\right| / \left|\bar{F}_{ice}(\bar{\tau}_4, \xi, \bar{\beta})\right|.$$

The ice height $\bar{F}_{ice}(\bar{\tau}_4, \xi, \bar{\beta})$ has both real and imaginary components, which are included to allow for the changes in the mode shape due to the influence of the flow along the attachment line.

A typical computation for the initial value starts with the ice shape $\bar{F}_{ice}(\bar{\tau}_4 = 0, \xi)$ as shown in Fig. 4.5. This ice height is used an input for the computation of the linearized airflow and the heat conduction within ice. After the computation of the

linearized problem, the heat fluxes in the airflow and within ice are computed, which are then used in the Stefan problem to advance the ice shape. Sufficient time is allowed in the computation to allow the development of the ice shape from the initial ice shape. A typical solution after long time is shown in Fig. 4.5. Different grid sizes as well as domain sizes are chosen to check for grid independence of the solutions (Fig. 4.5). A three-dimensional ice shape $\bar{F}_{ice}(\bar{\tau}_4, \xi, \zeta)$ is constructed from the two-dimensional ice shape $\bar{F}_{ice}(\bar{\tau}_4, \xi, \bar{\beta})$. One such ice shape is shown in Fig. 4.6 where the sweep angle parameter is $\bar{\Lambda} = 40$, $\bar{H}_{ice} = 100.53$, $m_\infty = 0.0$ and $\bar{\beta} = 0.750$. Typical grid sizes are $n_x = 201 \leftrightarrow 301$, $n_y = 51 \leftrightarrow 61$ for the linearized airflow and $n_x = 201 \leftrightarrow 301$, $n_y = 101$ for the ice with uniform grid stretching in the y-direction. The domain sizes are taken to be large enough to avoid any influence of the boundaries and are typically between $\xi = 55 \leftrightarrow 75$. There is a formation of ridges as well as smaller roughness elements which are part of these ridges. A higher sweep angle parameter $\bar{\Lambda} = 80$, is also used to check for grid independence over the range of wave numbers under consideration, which is shown in Fig. 4.7. The grid solution (o) in Fig. 4.7 uses $n_x = 201$, $n_y = 51$ for the linearized airflow with a domain of $\xi = [-55, 55]$ and $\eta = [0 : 10]$, and $n_x = 201$, $n_y = 101$ for the ice with a domain of $\xi = [-55, 55]$ and $\eta = [0 : -5]$. The other grid solution uses a larger domain with $\xi = [-75, 75]$ with $n_x = 301$. A grid with $n_x = 201$, $n_y = 51$ for the linearized airflow and $n_x = 201$, $n_y = 101$ for the ice with uniform normal coordinate grid stretching is used for all computations afterwards where the domain for the airflow is $\xi = [-55, 55]$ and $\eta = [0 : 10]$ and the domain for ice is $\xi = [-55, 55]$ and $\eta = [0 : -5]$.

Four key parameters influence the development of ice surface instabilities in swept wing stagnation icing: the sweep angle parameter, the thickness of the main ice sheet, the Gibbs-Thomson effect (which locally changes the ice surface temperature) and the heat flux from the airflow. While increase in sweep angle parameter and thickness of the main ice sheet increase the instability of the ice surface, increased heating from the airflow and the Gibbs-Thomson effect decrease this instability. The combination of all

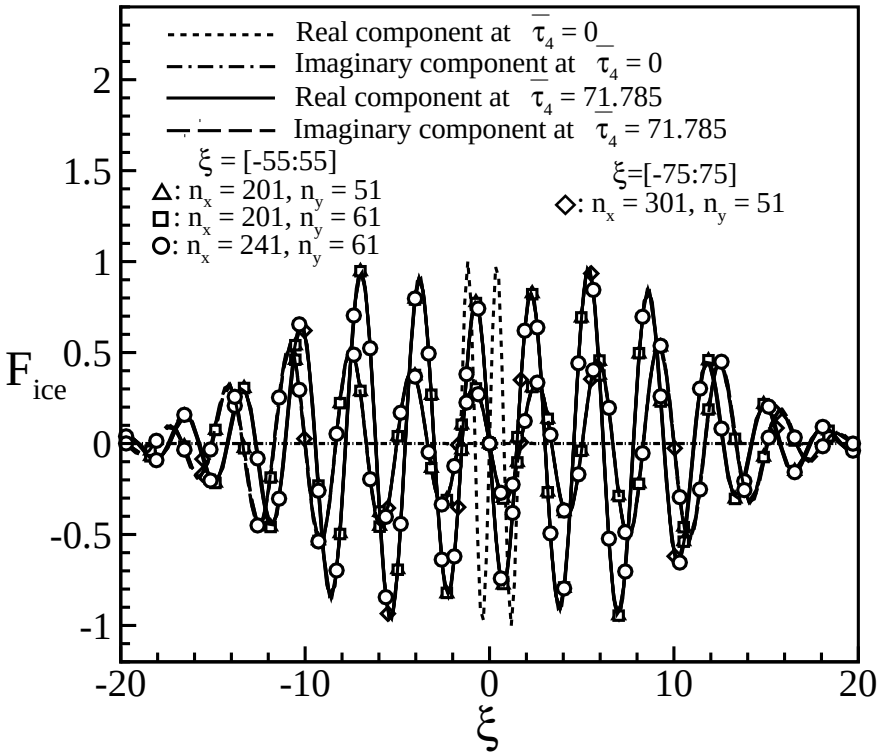

Figure 4.5 A typical solution for the linearized stability problem showing real and imaginary components of the initialized ice shape as well as the ice shape at $\bar{\tau}_4 = 71.875$. $\bar{\Lambda} = 40.0$, $m_\infty = 0.00$, $\bar{E} = 0.0113$, $\bar{\beta} = 0.750$, $H_{ice} = 100.53$. In ice, $n_y = 101$, with uniform grid stretching.

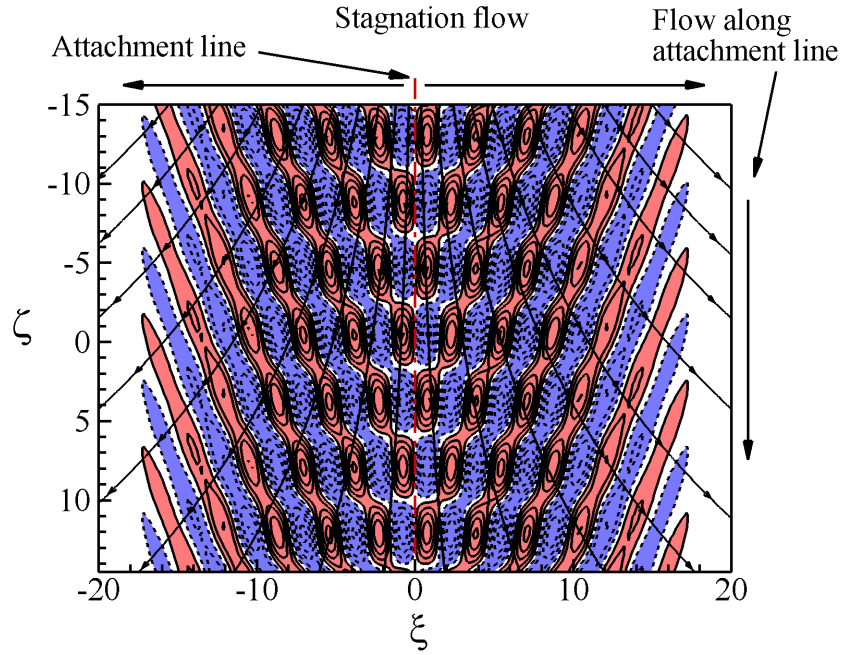

(a)

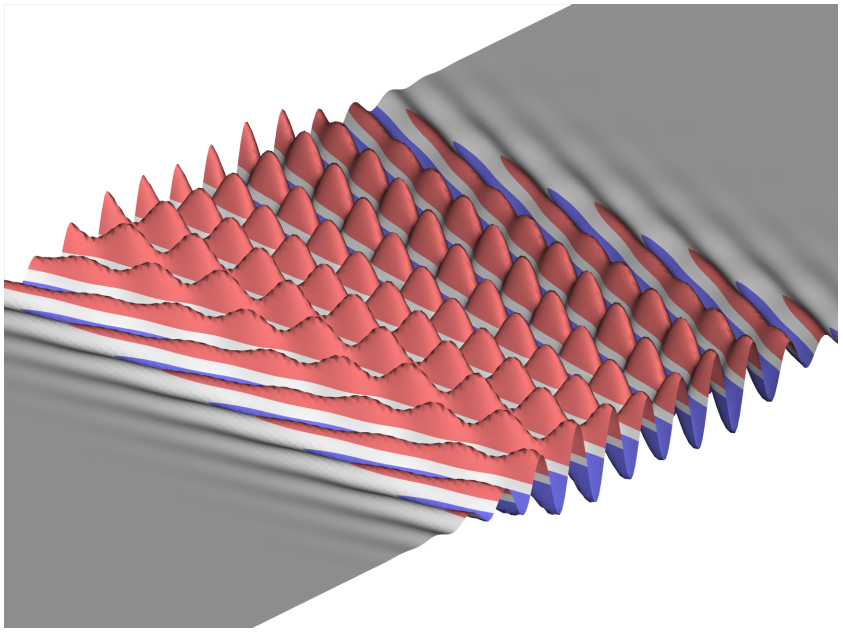

(b)

Figure 4.6 Ice surface shape at time $\bar{\tau}_4 = 71.875$ for $\bar{\Lambda} = 40.0$, $m_\infty = 0.0$ and $\bar{\beta} = 0.750$: (a) Topview - Arrows indicate primary airflow direction. Also shown are limiting surface streamlines of the primary airflow. $\xi = 0$ is the attachment line. (b) Three-dimensional view.

these effects changes the growth rate as well as the roughnesses which evolve from the instability.

Increase in sweep angle leads to a stronger contribution of the flow along the attachment line (compared with the flow along the stagnation line) to the growth rate of the instability. This amplifies the heat flux in the linearized airflow for a fixed heat flux in the base flow. This increased heat flux causes a faster growth of the peaks and the troughs of the perturbed ice surface and leads to larger growth rates of roughness shapes (see Fig. 4.8). The increased heat flux from the linearized airflow also results in a larger range of wave numbers where the ice surface becomes unstable.

The thickness of the main ice sheet affects the heat flux within ice close to the ice surface. When the ice sheets are thinner, this heat flux is larger. This increased heat flux within the main ice sheet tends to force a decrease in the growth rate of the peaks of the perturbed ice surface. This stabilizing effect of the height of main ice sheet is seen in Fig. 4.11.

The Gibbs-Thomson effect changes the ice surface temperature due to the changes in surface curvature (see Section 3.1). Since this effect includes curvature, it strongly influences the selection of specific wavelengths for the streamwise direction ξ for a given spanwise wave number $\bar{\beta}$. The role of Gibbs-Thomson effect in decreasing the growth rates of the ice surface instability is seen in Fig. 4.9.

Increased cooling from the air heat flux increases growth rate of the perturbed ice surface. As the stagnation temperature approaches the freezing temperature of water, the cooling heat flux from the airflow decreases. This in turn leads to a reduced heat flux from the linearized airflow and a resulting decrease in the growth rate of the ice surface. The stabilizing effect of increased heating due to an increase in scaled Mach number is seen in Fig. 4.10.

The above mentioned effects on the growth rates also lead to a change in the roughness shapes near the maximum growth rate. For a given sweep angle, increased stability

of the perturbed ice surface leads to growth of roughnesses which are more circular in cross-sectional shape. As the ice surface becomes more unstable, long thin roughnesses are seen, which are oriented somewhat normal to the local limiting streamlines (see Fig. 4.18).

For $\bar{\beta}$ close to 0, roughnesses having the largest growth rate are long and thin, and oriented perpendicular to the limiting surface stream lines of the stagnation flow with no sweep. These roughnesses have similar growth rates, a case seen earlier in ice surface instability studies. This behavior changes as the sweep angle increases. The roughnesses become oriented approximately normal to the limiting streamlines of the swept wing stagnation flow. These roughnesses also merge together to form streaks, unlike the pure stagnation line icing problem where the roughnesses are regularly aligned in a checker-board pattern (see Fig. 4.17). For unswept wings, a large number of sinusoidal disturbances are given which result in the growth of the outermost roughnesses in the beginning (see Fig. 4.16(a)). The roughnesses then grow to occupy the region between the stagnation line and the outermost roughnesses (see Fig. 4.16(b)) and eventually reach an equilibrium shape with growth everywhere on the surface with maximum height at the stagnation line. A similar behavior is also seen for the swept wing stagnation flow, however with a significant difference. The outermost roughnesses show the formation of ridges early in the instability (see Fig. 4.16(c)). Eventually, ridge formation with overlying roughness elements is seen (see Fig. 4.16(d)). Also noticeable is a two-zone behavior with the inner ridges aligned with the flow and outer ridges aligned against the flow. The outer ridges move outward from the attachment line. It is suggested that as the outer ridges keep moving away from the attachment line, the inner ridges align themselves approximately normal to limiting streamlines of the airflow.

A strong cooling case is chosen to study the change in roughness patterns for given wave numbers $\bar{\beta}$ with increasing sweep angle parameter $\bar{\Lambda}$. Here, $m_\infty = 0$, $\bar{H}_{ice} = 100.53$, $\bar{E} = 0.0113$. Three sweep angle parameters chosen are $\bar{\Lambda} = 20, 40, 80$. The typical

roughness shapes are seen in Figs. 4.12 through 4.14. The roughnesses are initially aligned with the flow for smaller wave numbers as for $\bar{\beta} = 0.5625$ and $\bar{\Lambda} = 20$ (see Fig. 4.12(a)). As the spanwise wave number slowly increases for $\bar{\Lambda} = 20$, the orientation of the roughnesses change and they become perpendicular to the limiting streamlines near the attachment line (see Fig. 4.12(c)). The formation of ridges with smaller roughness elements is also seen in this figure. Here, the growth rate of these roughness shapes are similar for $\bar{\Lambda} = 20$. For $\bar{\Lambda} = 40$, the growth rate of the roughnesses increases with increasing wave number, i.e. the growth rate for $\bar{\beta} = 1.125$ is greater than the growth rate for $\bar{\beta} = 0.5625$. This is also associated with a stronger evidence of formation of ridge-like shapes. As the sweep angle increases to $\bar{\Lambda} = 80$, the process of ridge formation becomes stronger along with an increase in growth rate for increasing wave numbers and elongated roughness shapes. The smaller roughness elements merge into these ridges and the orientation of the roughnesses approximately normal to the limiting streamlines happens for smaller spanwise wave numbers (see Figs. 4.12(b) and 4.13(b)). For even larger sweep angles, the process of the change in orientation as well as the merging of the small roughnesses into ridges happens at even lower spanwise wave numbers and only the long, thin ridge-like roughnesses oriented perpendicular to the limiting streamlines remain prominent over most spanwise wave numbers (see Figs. 4.14(a) through 4.14(c)).

A comparison of the present computational approach for roughnesses is made with one of the recent swept wing icing experiments at ONERA (see Presteau *et al.* [5]) which shows the roughnesses along the attachment line of a glaze ice accretion in Fig. 4.21(a). Near the attachment line, there are ridges of length 3 mm with width 1 mm. Here, the flow conditions are given by $V_\infty = 35$ m/s, $T_\infty = -5^o C$ and $\lambda = 30^o$. For the longer ice accretion time of 12 minutes, a thick ice sheet is assumed with $f_{ice} \backsimeq 4.9$cm. A chord length of 63.3 cm is taken. This yields the scaled parameters $m_\infty = 0.79$, $\bar{\Lambda} = 86.5$, $\bar{H}_{ice} = 29.3$, $\bar{E} = 0.0061$. The growth rates for different wave numbers for this case are shown in Fig. 4.20. For the roughness at the maximum growth,

the roughness pattern is show in Fig. 4.21(b). These elongated ridge-like shapes are about 1 mm in length and .5 mm in width, similar to the ridges in the icing experiments (Presteau *et al.* [5]). The roughness pattern near the attachment line in Fig. 4.21(a) is chaotic. However, these roughnesses are clearly orientated approximately perpendicular to the surface streamlines near the attachment line, forming upward pointing elongated "U" and "V" shapes. In the present computation (Fig. 4.21(b)), the roughnesses are also aligned approximately perpendicular to the surface limiting streamlines and the size of these roughnesses are similar in magnitude to the roughnesses seen in the experiment. It must be stressed that this comparison cannot be made more exact because the roughnesses seen in the experiment have not been quantified, some critical parameters in the experiment are unknown, and (as will be discussed later) the roughness prediction may require more detailed modeling. However, it is encouraging that the general elongated roughness elements are similar to those observed in experiments.

As the sweep angle increases, the maximum growth rate also increases. The orientation of the roughness at this maximum growth rate is approximately perpendicular to the limiting streamlines of the swept wing stagnation flow. The range of spanwise wave numbers $\bar{\beta}$ for which the instability is seen, also increases. As the physical sweep angle λ becomes $\mathcal{O}(1)$, the corresponding sweep angle parameter $\bar{\Lambda}$ used in the present formulation becomes large. The limiting streamlines for this case become almost parallel to the attachment line. As the range of wave numbers increases with increase in sweep angle, the spanwise wave number for the maximum growth rate becomes such that roughnesses become almost perpendicular to the attachment line. This implies that for a fixed Gibbs-Thomson parameter $\bar{E}$, the increase in sweep angle leads to a decreasing influence of the Gibbs-Thomson effect.

Given the typical roughness patterns seen in the linearized computations and the ice shapes seen in later stages in experiments, a mechanism for the spanwise discontinuous structures called "scallops" is suggested here. Initially, the flow conditions determine the

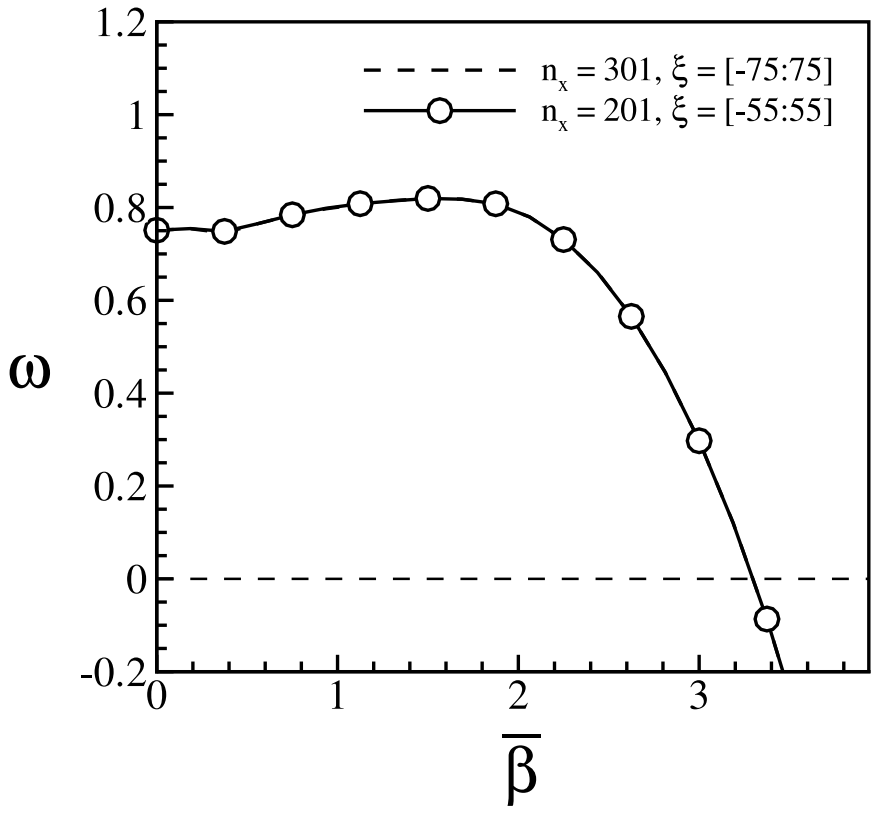

Figure 4.7 Grid independence for growth rates for the case : $\bar{\tau}_4 = 71.875$, $\bar{\Lambda} = 80.0$, $m_\infty = 0.0$, $\bar{E} = 0.0113$, $H_{ice} = 100.53$.

formation of ice surface instabilities, which align themselves to form ridges approximately perpendicular to surface limiting streamlines (see Fig. 4.19). These instabilities grow till they effect a finite change in the airflow. This leads to greater cooling near the front of the roughnesses which causes roughnesses to grow into the airflow. Eventually, due to water trapping and local cooling, these roughnesses merge to larger ice shapes orientated against the airflow. The large scale structures seen much later in the ice accretion process could also involve droplet shadowing and its effect on the mass of water locally available for accretion.

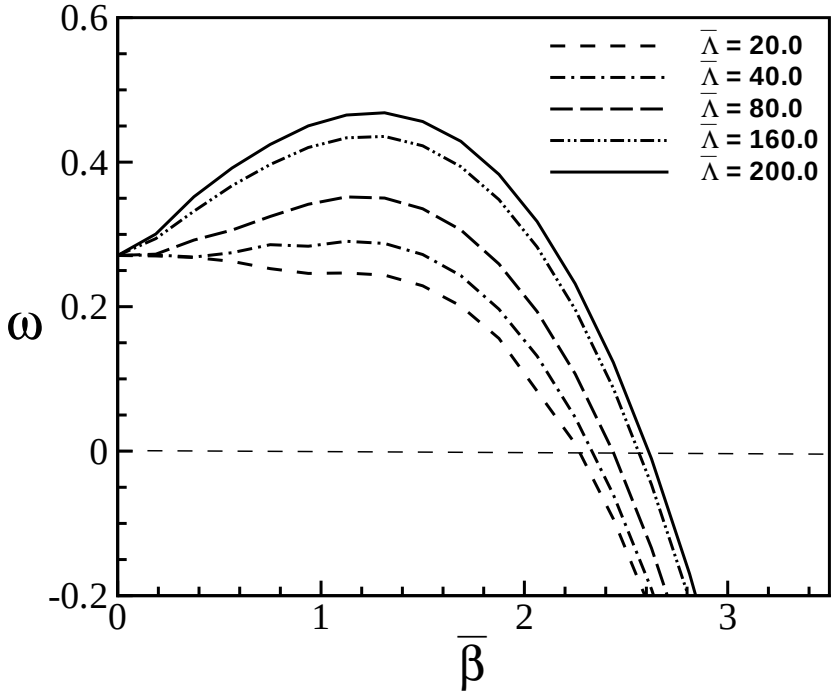

Figure 4.8 Growth rates with changing sweep angle parameter $\bar{\Lambda}$. $\bar{\tau}_4 = 71.875$, $m_\infty = 1.5$, $\bar{E} = 0.0113$, $H_{ice} = 100.53$.

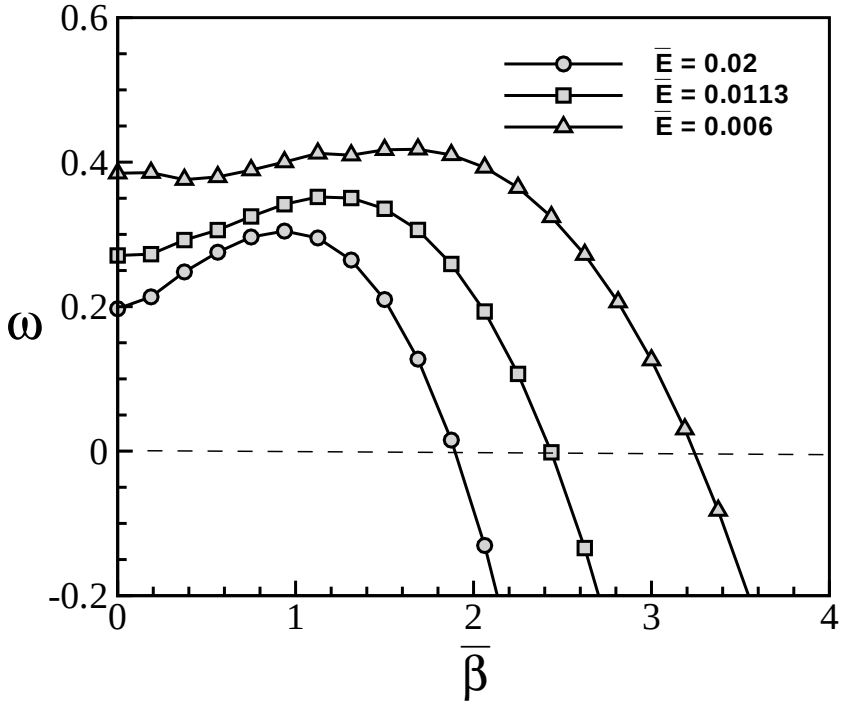

Figure 4.9 Growth rates with changing Gibbs-Thomson parameter $\bar{E}$. $\bar{\tau}_4 = 71.875$, $m_\infty = 0.0$, $\bar{\Lambda} = 80.0$, $H_{ice} = 100.53$.

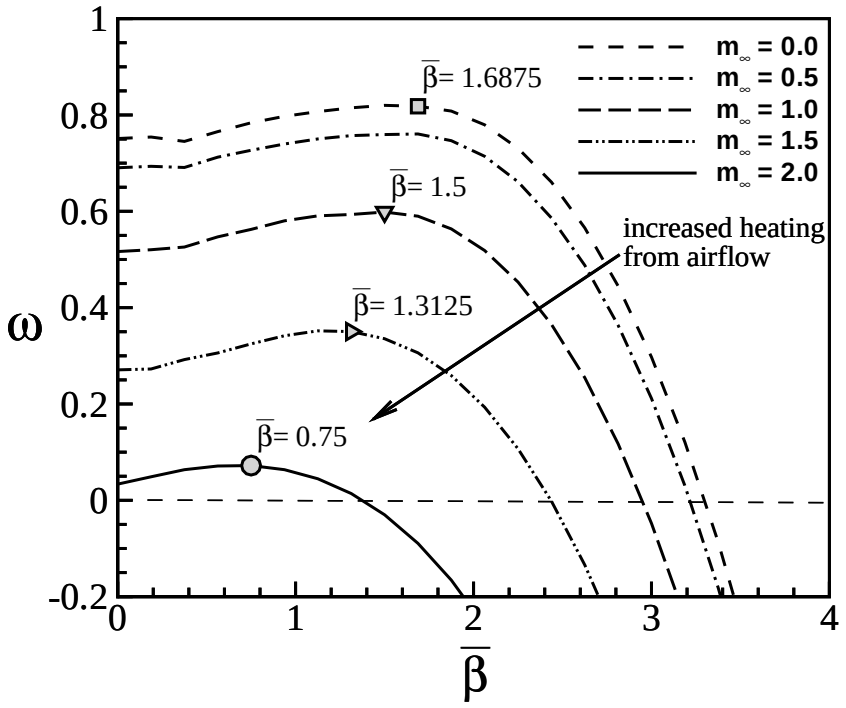

Figure 4.10 Growth rates with increased aerodynamic heating. $\bar{\tau}_4 = 71.875$, $\bar{\Lambda} = 80.0$, $\bar{E} = 0.0113$, $H_{ice} = 100.53$.

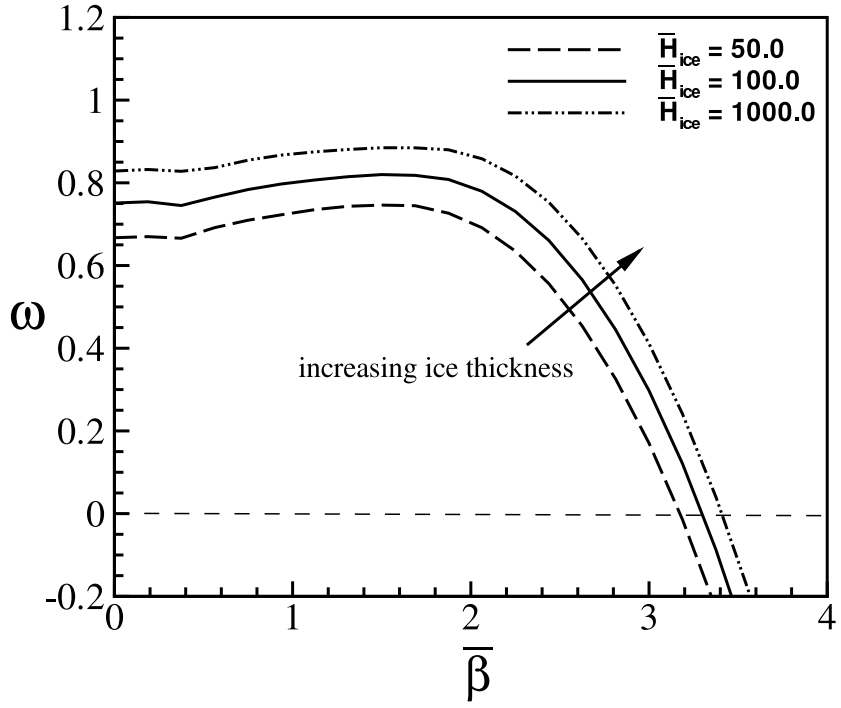

Figure 4.11 Growth rates with increasing height of the main ice sheet. $\bar{\tau}_4 = 71.875$, $\bar{\Lambda} = 80.0$, $\bar{E} = 0.0113$, $m_\infty = 0.0$.

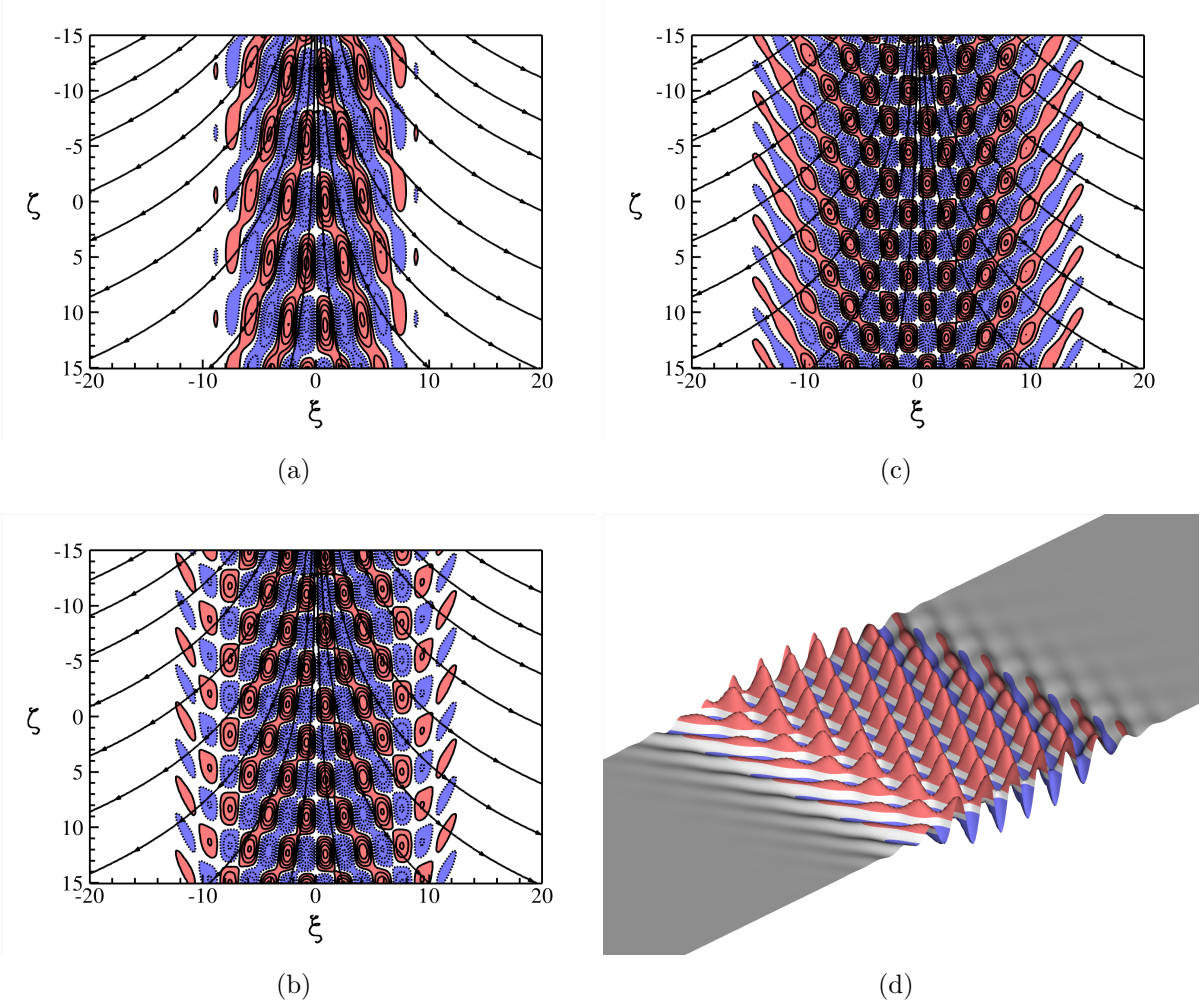

Figure 4.12 Ice surface shapes at time $\bar{\tau}_4 = 71.875$ for $\bar{\Lambda} = 20.0$, $m_\infty = 0.0$, $\bar{\tau}_4 = 71.875$ (see Fig. 4.6 for additional description) : (a) topview for $\bar{\beta} = 0.5625$, (b) topview for $\bar{\beta} = 0.9375$, (c) topview for $\bar{\beta} = 1.125$, (d) three-dimensional view for $\bar{\beta} = 1.125$.

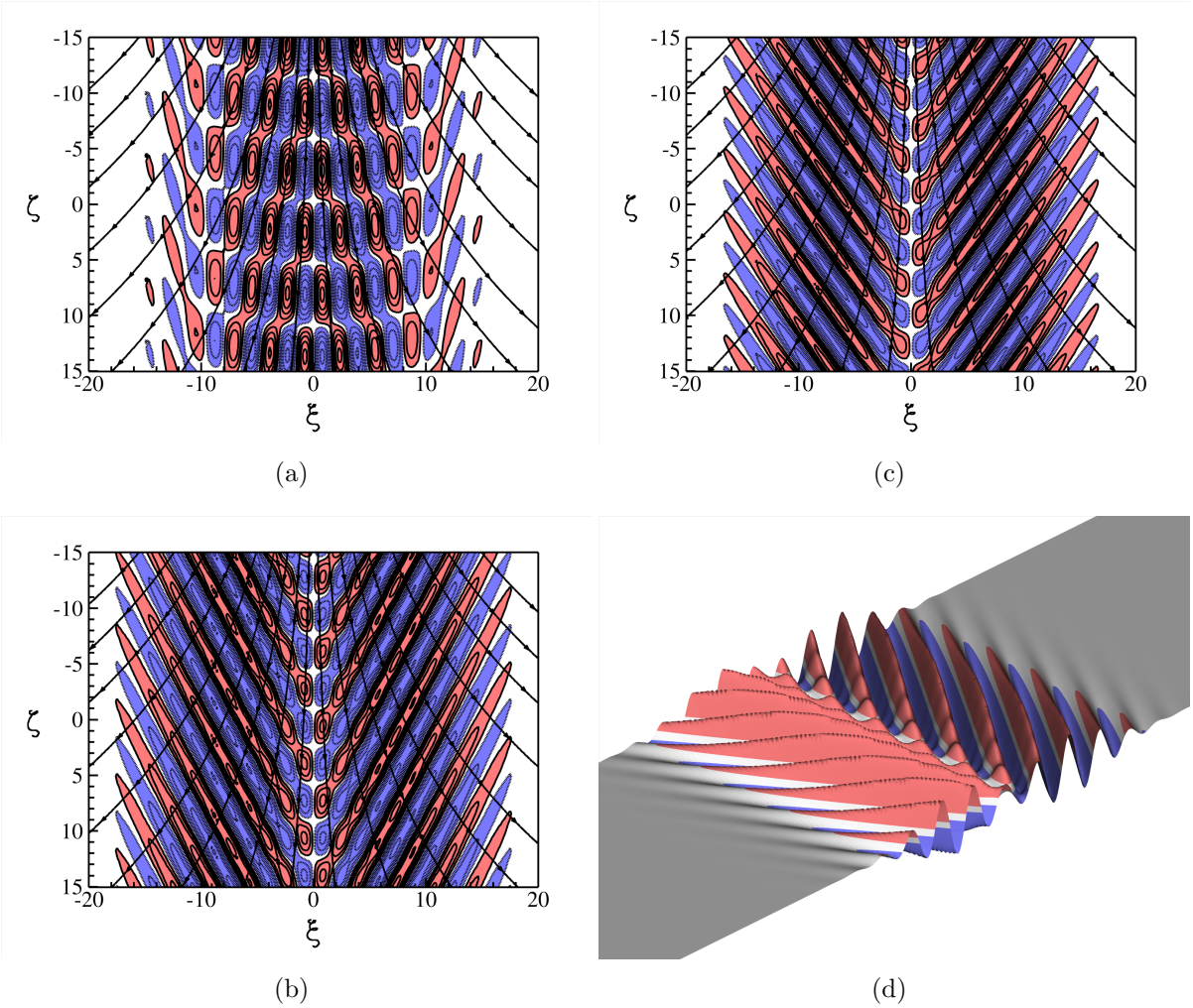

Figure 4.13 Ice surface shapes at time $\bar{\tau}_4 = 71.875$ for $\bar{\Lambda} = 40.0$, $m_\infty = 0.0$, $\bar{\tau}_4 = 71.875$ (see Fig. 4.6 for additional description) : (a) topview for $\bar{\beta} = 0.5625$, (b) topview for $\bar{\beta} = 0.9375$, (c) topview for $\bar{\beta} = 1.125$, (d) three-dimensional view for $\bar{\beta} = 1.125$, of the roughnesses.

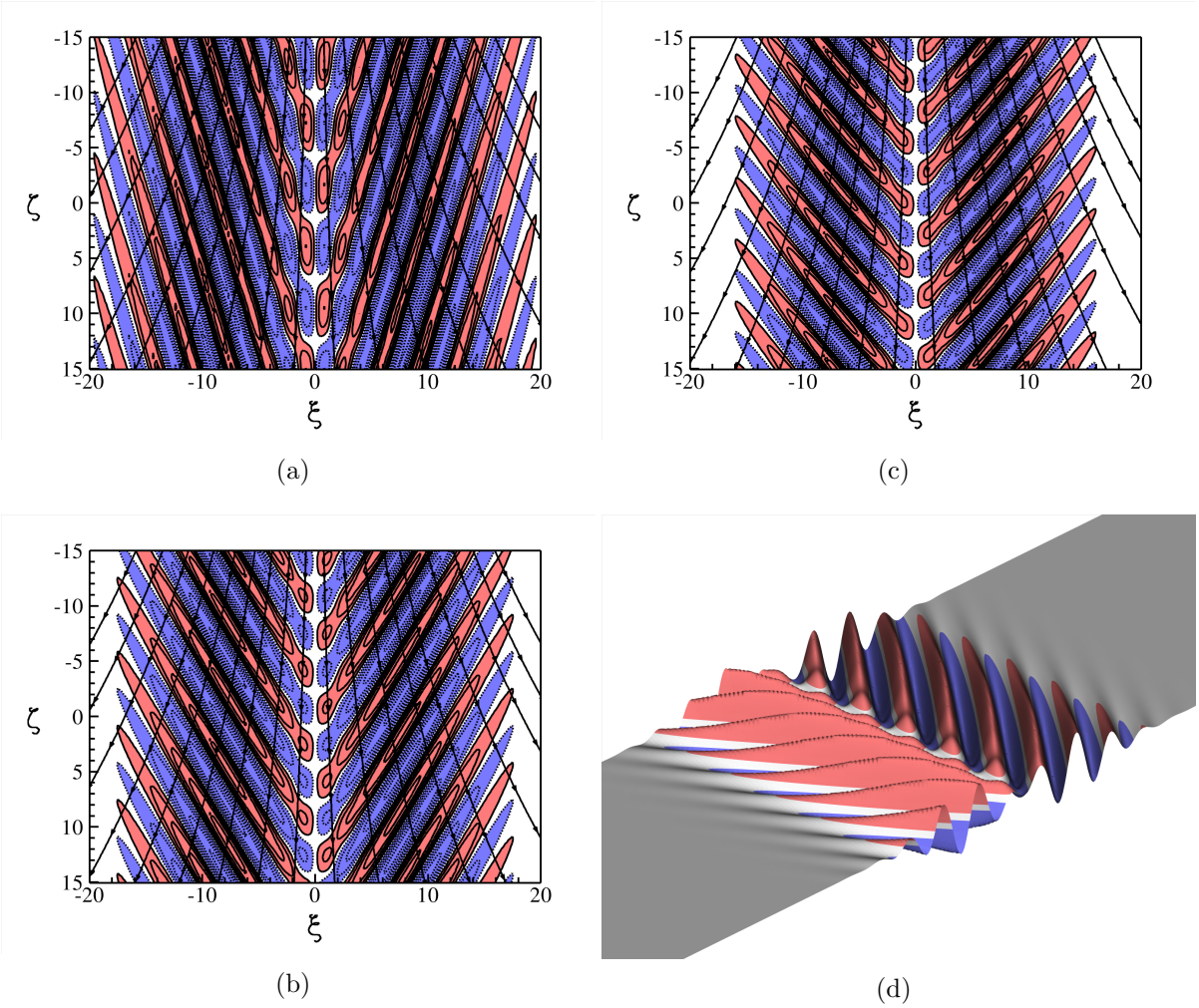

Figure 4.14 Ice surface shapes at time $\bar{\tau}_4 = 71.875$ for $\bar{\Lambda} = 80.0$, $m_\infty = 0.0$, $\bar{\tau}_4 = 71.875$ (see Fig. 4.6 for additional description) : (a) topview for $\bar{\beta} = 0.5625$, (b) topview for $\bar{\beta} = 0.9375$, (c) topview for $\bar{\beta} = 1.125$, (d) three-dimensional view for $\bar{\beta} = 1.125$, of the roughnesses.

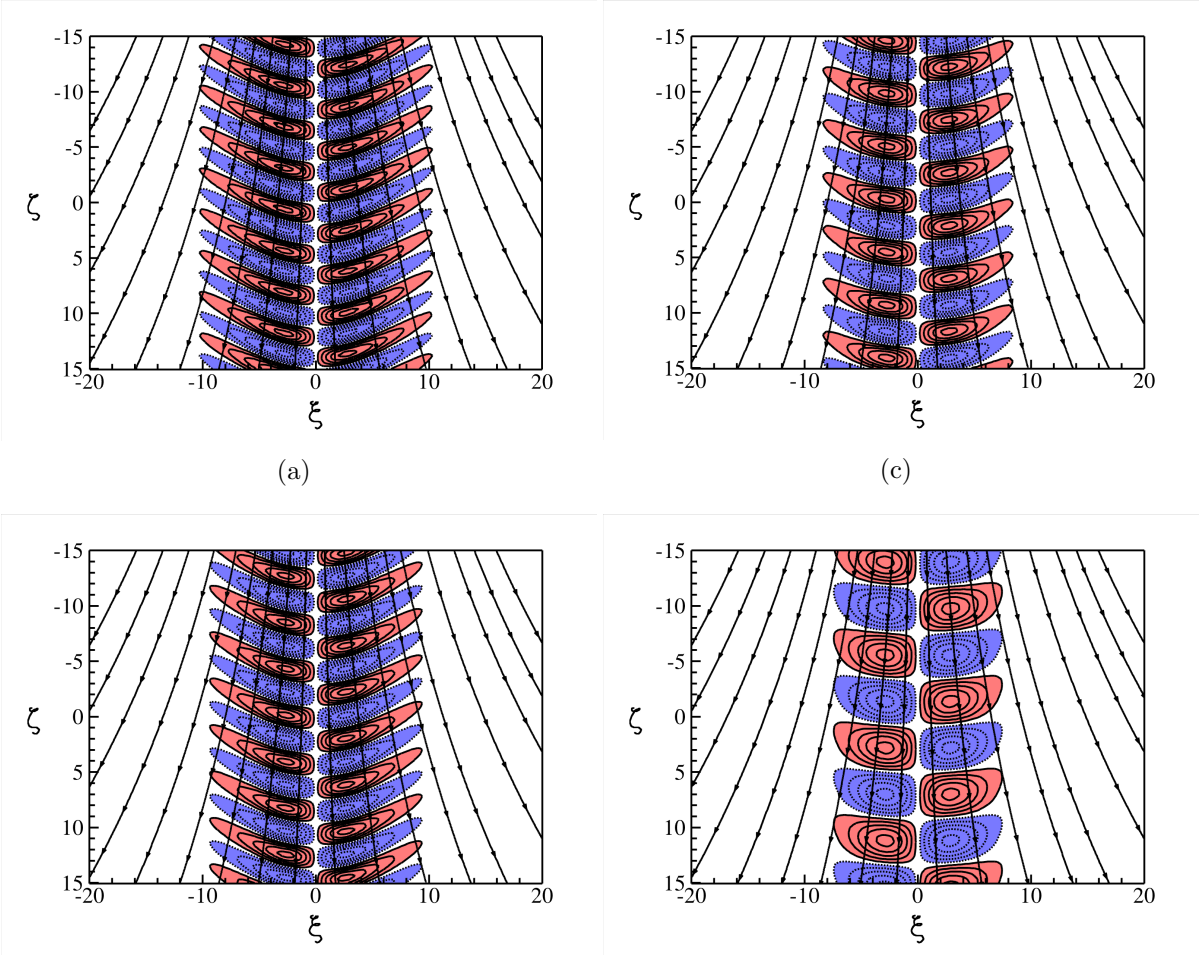

Figure 4.15 Ice surface shapes at time $\bar{\tau}_4 = 71.875$ for $\bar{\Lambda} = 80.0$ (see Fig. 4.6 for additional description) : topviews of roughnesses near maximum growth rates of the symbols shown in Fig. 4.10 with increased aerodynamic heating : (a) $m_\infty = 0.0$, $\bar{\beta} = 1.6875$, (b) $m_\infty = 1.0$, $\bar{\beta} = 1.5$, (c) $m_\infty = 1.5$, $\bar{\beta} = 1.3125$, (d) $m_\infty = 2.0$, $\bar{\beta} = 0.750$.

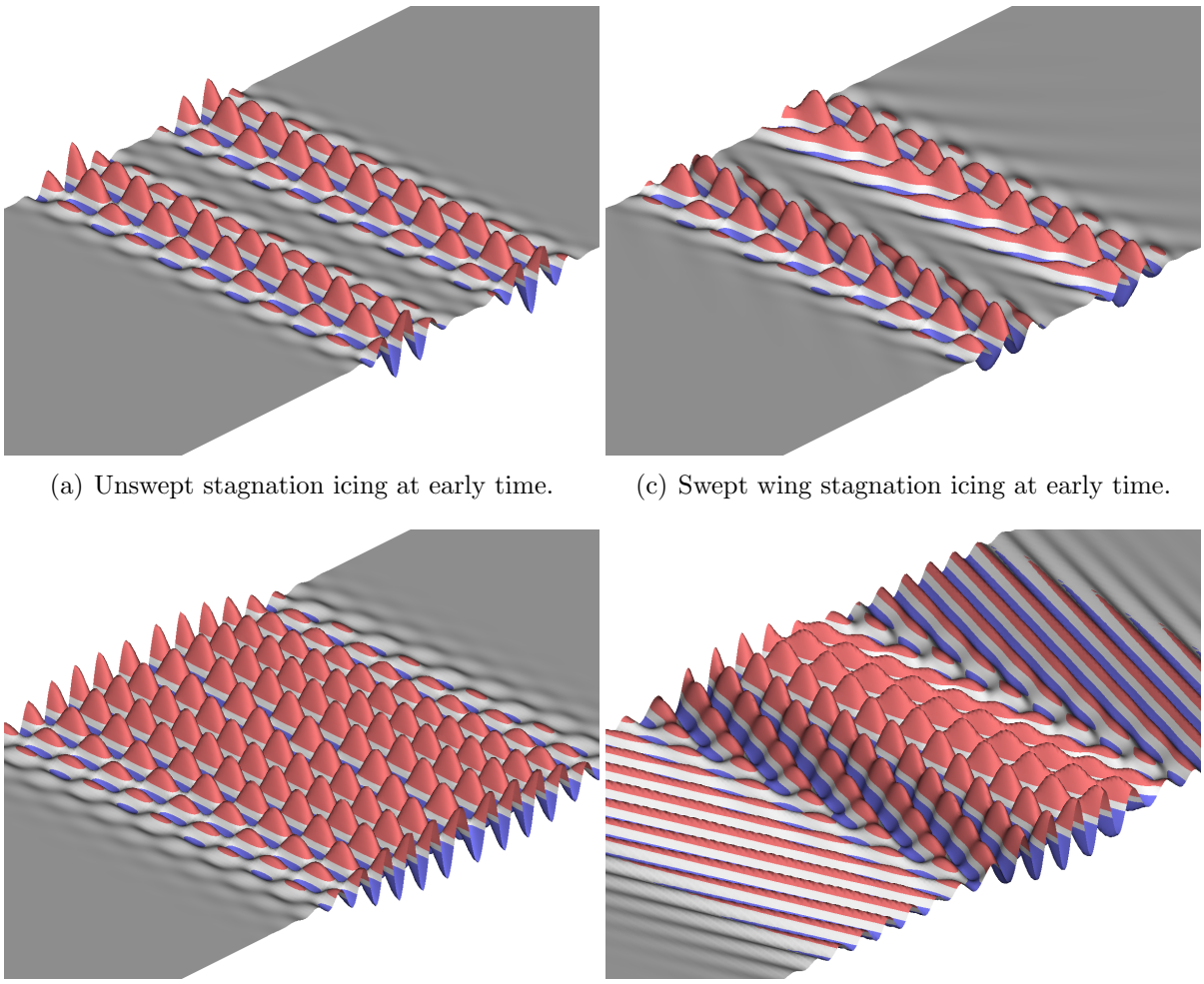

(a) Unswept stagnation icing at early time.

(c) Swept wing stagnation icing at early time.

(b) Unswept stagnation icing at later time.

(d) Swept wing stagnation icing at later time.

Figure 4.16 Ice surface shapes for $m_\infty = 0.0$, $\bar{\beta} = 0.750$, unswept :(a) $\bar{\Lambda} = 0$, $\bar{\tau}_4 = 11.7$ (b) $\bar{\Lambda} = 0$, $\bar{\tau}_4 = 45.12$, and swept : (c) $\bar{\Lambda} = 40$, $\bar{\tau}_4 = 11.7$ (d) $\bar{\Lambda} = 40$, $\bar{\tau}_4 = 126.9$, showing the spreading of the roughnesses with time.

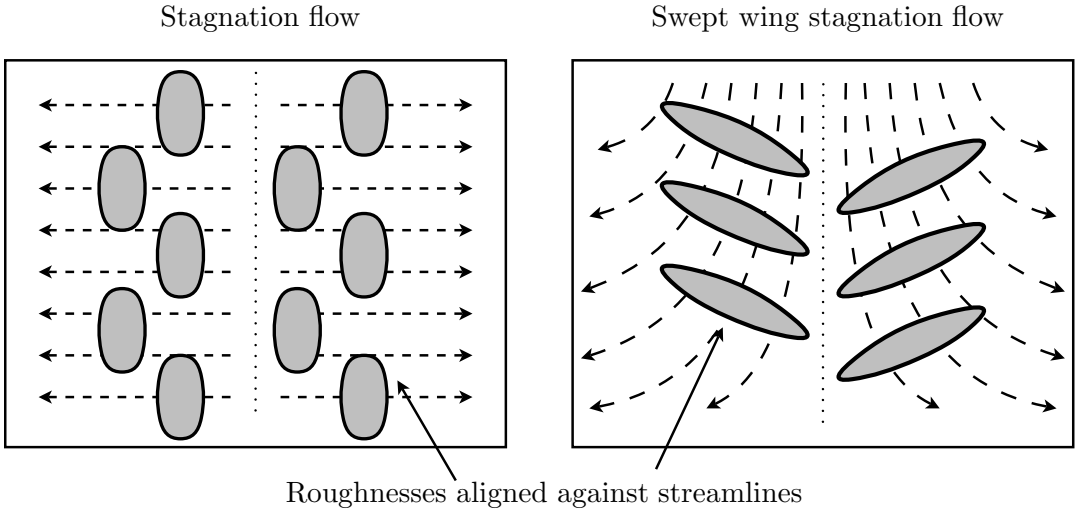

Figure 4.17 Typical roughness alignment with surface limiting streamlines for straight and swept wing attachment line flows.

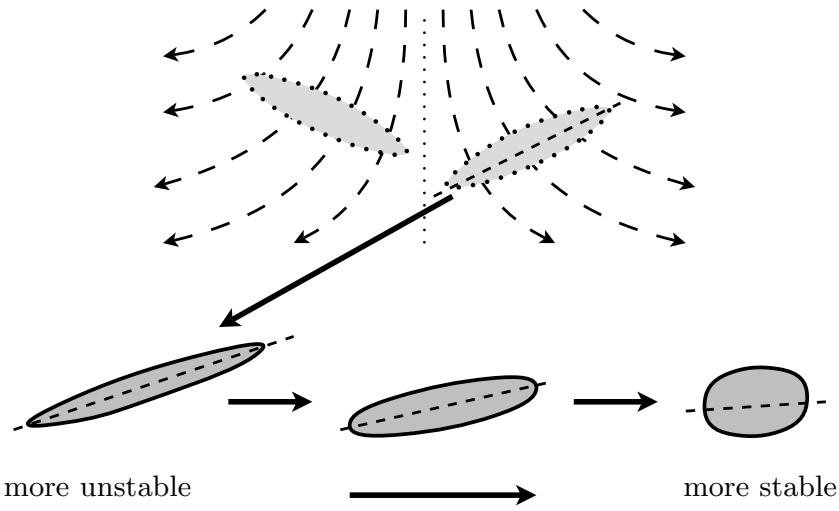

Figure 4.18 Typical change of long and thin roughness shapes into "circular" roughnesses with increased heating or decreasing thickness of the main ice sheet at a fixed sweep angle.

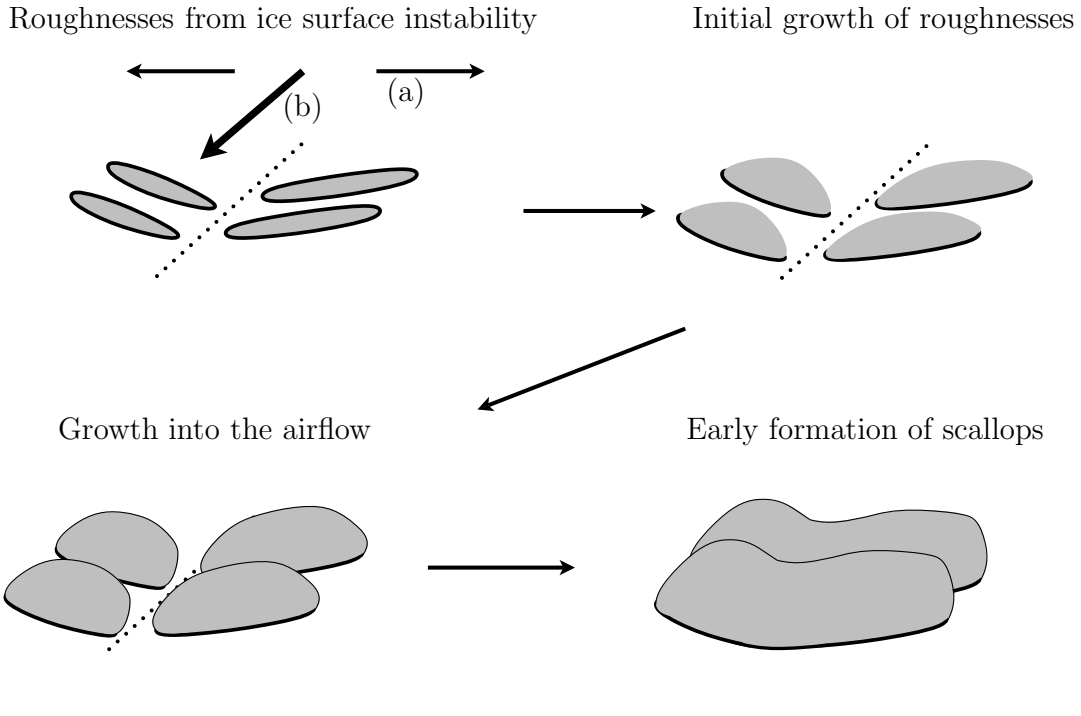

Figure 4.19 Suggested scallop initiation mechanism from roughnesses generated by ice surface instability, (a) & (b) show flow directions $\perp$ and $\parallel$ to attachment line.

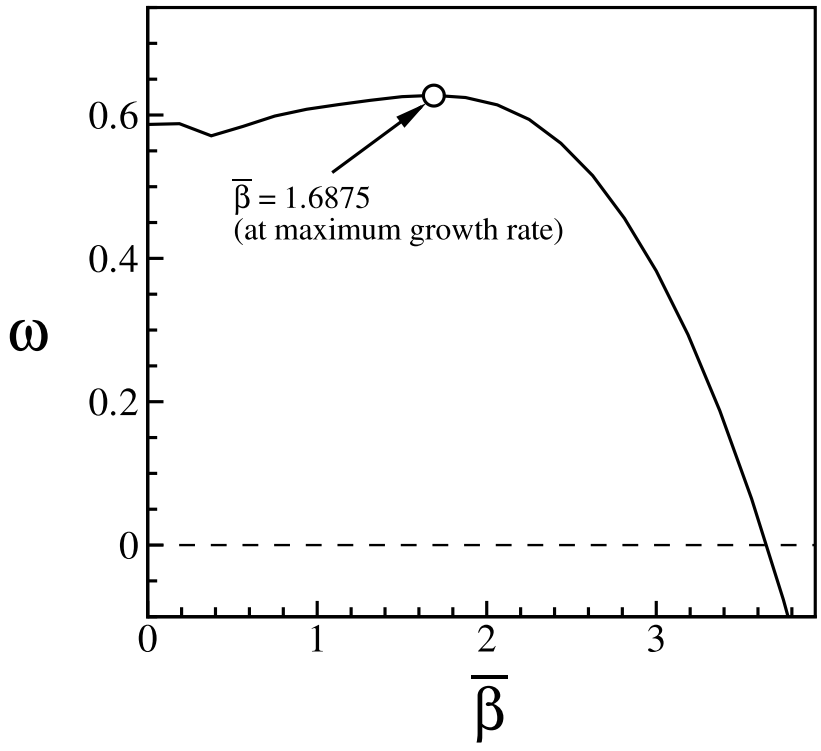

Figure 4.20 Growth rate of roughness shapes for the case corresponding to the experimental results of Presteau *et al.* [5]. $m_\infty = 0.79$, $\bar{\Lambda} = 86.5$, $\bar{H}_{ice} = 29.3$, $\bar{E} = 0.0061$.

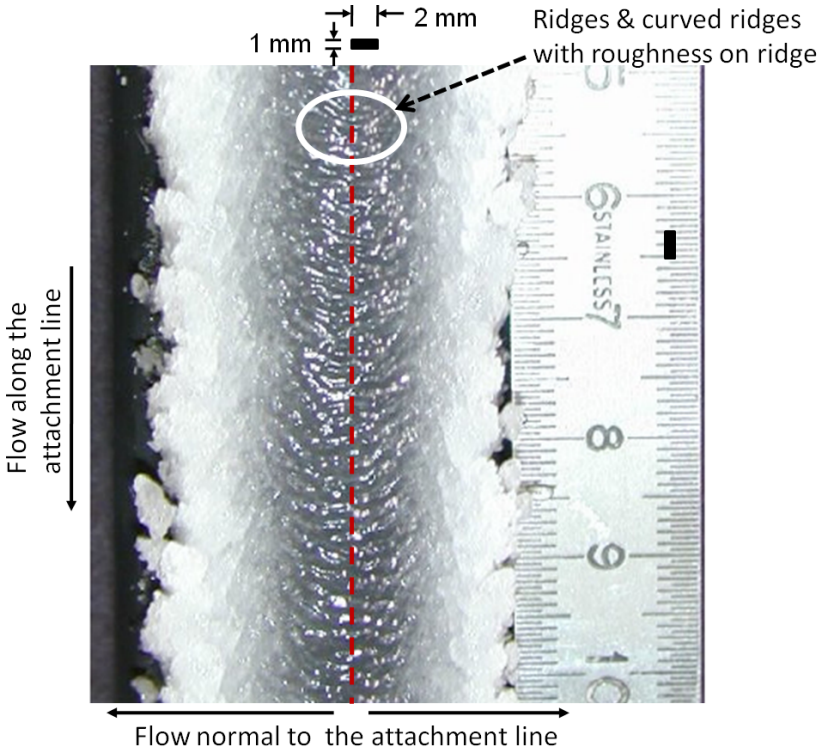

(a)

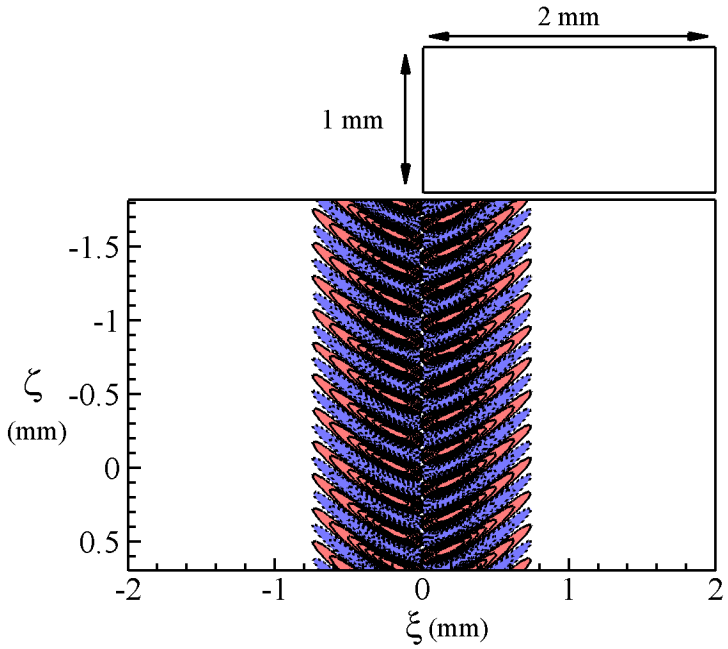

(b)

Figure 4.21 (a) Shapes of roughnesses seen in swept wing icing experiments of Presteau *et al.* [5] (reproduced here with permission of Dr. E. Montreuil), (b) Roughness patterns in the immediate vicinity of the attachment line seen in computations of the linearized stability analysis.

CHAPTER 5. GLAZE ICING ROUGHNESS FORMATION FOR A PARABOLIC LEADING EDGE

5.1 Overview of roughnesses in glaze icing

The experiments of Shin [29, 30], Anderson and Shin [31] and Anderson, Hentschel and Ruff [1] provide information about the sizes of the roughnesses as well as the dimensions of the smooth zone seen in unswept ice accretion. A typical result from the experiments of Anderson, Hentschel and Ruff [1] is shown in Fig. 5.1 which shows presence of a smooth zone near the stagnation line where roughnesses are absent and a clearly defined region away from the stagnation line where the ice roughnesses begin to appear. As seen in Fig. 5.1, the transition from the smooth zone to the rough zone is sharp. These roughnesses also have specific diameters, typically of the order of 0.6-2 mm and usually larger than the boundary layer thickness. In this chapter, a few representative results from the experiments of Anderson, Hentschel and Ruff [1] are chosen for a preliminary comparison with a simplified model for predicting roughness diameters. The simplified model is developed using the stagnation line icing asymptotic model as a guideline. The purpose of this chapter is to make a preliminary assessment of this simplified ice surface instability model, determine deviations from experiments and identify possible sources of error.

Icing experiments of Shin [29, 30], Anderson and Shin [31], Anderson, Hentschel and Ruff [1], use scale models which are exposed to airflow with supercooled water droplets. In these experiments, it is essential to maintain similitude of the flow parameters which

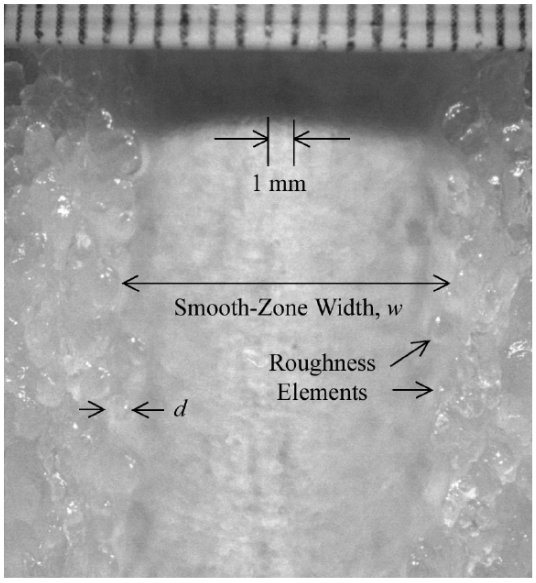

Figure 5.1 Smooth zone seen in experiments (see Anderson, Hentschel and Ruff [1]), reprinted by permission of AIAA.

directly affect ice accretion. A set of scaling parameters is used which take the icing physics into account. Anderson and Tsao [64] give a concise overview of these scaling parameters and the icing physics relevant to the scaling procedure used in the experiments. One such parameter, called droplet inertia parameter, is used to ensure that water droplet trajectories are similar between the model flow conditions and the reference flow conditions, since these trajectories influence the amount of water being accumulated on the surface. The heat transfer from the airflow affects the rate of ice growth which is included in parameters that describe the difference between the free-stream temperature and the freezing temperature of water. The total ice height is controlled by the fraction of incipient water being frozen on the ice surface (defined later as the freezing fraction), the liquid water content of the supercooled droplets in the airflow, the velocity of the incoming flow and the time of ice accretion. All these parameters are discussed exhaustively in Anderson's [65] review of the icing scaling methods. Some of these parameters are used later in this chapter in order to make a comparison with experiments.

The stagnation line icing model discussed earlier shows that ice surface instabilities can be a mechanism for ice roughness formation. This understanding is used to construct a linear stability model for studying ice surface instabilities over a parabolic leading edge which is then used to compare theoretical estimates of roughness diameters and smooth zones with the results seen in experiments. Several effects contribute to the stability of the ice surface (see Fig. 5.2). A smaller ice height as well as an airfoil surface which is much colder than the freezing temperature of water have a stabilizing effect on the ice surface. When the free-stream temperature is colder than the freezing temperature of water, the cooling due to the air heat flux has a destabilizing effect on the ice surface. While the droplet impacts do not have a direct effect on the ice surface stability, the droplet impacts lead to an overall increase in ice height, which in turn affects the ice stability. Also, the Gibbs-Thomson effect at the water/ice interface prevents the formation of very small roughnesses.

At the start of an icing tunnel experiment, the wing is expected to be somewhat near the total temperature of the free-stream airflow. However, this may not be the case since the airfoil is scrubbed and cleaned with a warm solvent prior to each test. In the early phase, when the ice first starts to accrete on a cold airfoil surface, the heat flux within ice dominates the ice growth. Soon after this initial ice accretion, the ice insulates the airflow from the metal skin of the wing (see Rothmayer [48], Anderson and Shin [31]) and the metal skin is expected to slowly adjust to the freezing temperature of water in a transient manner. In this phase, the temperature of the metal skin is likely to be closer to the freezing temperature of water and the cooling heat flux from the airflow and the heat flux within the ice are likely to be similar in magnitude. However, the above is speculative. The fact of the matter is that the airfoil temperature in an icing test is not measured. Since the airfoil temperature is unknown, a series of temperatures are chosen for the airfoil in order to evaluate its effect on the ice surface instability. Based on the stagnation line asymptotic model, a linear stability model for the parabolic leading

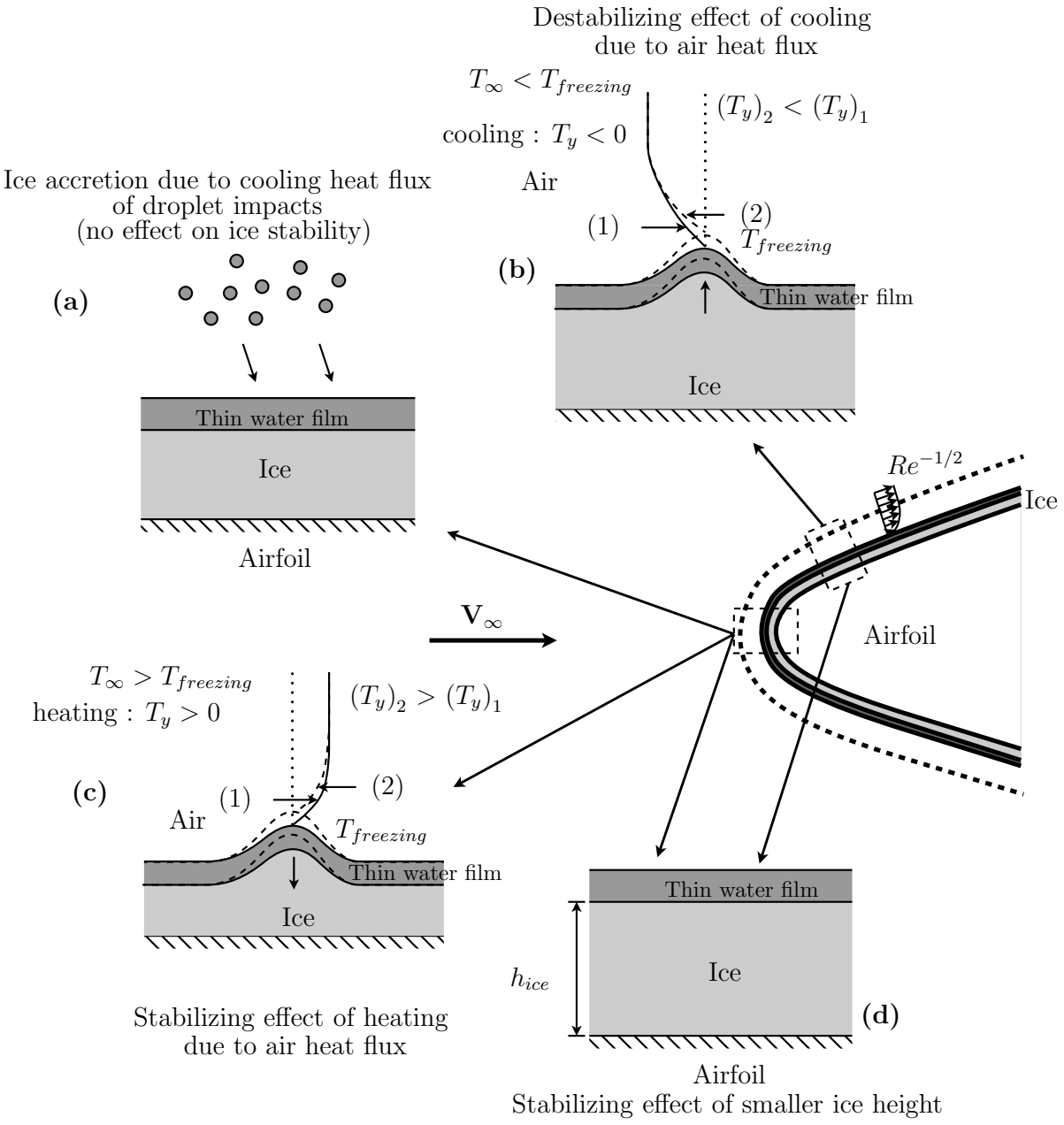

Figure 5.2 Factors influencing the formation of roughnesses and the smooth zone : (a) droplet impacts do not contribute directly to ice stability, but influence the ice thickness, (b) cooling heat flux from the airflow increases the instability of the ice surface, (c) heating or decreased cooling heat flux from the airflow decreases the instability of the ice surface near the stagnation region, (d) thinner ice sheets create a larger net heat flux within ice which promotes growth of the mean ice sheet and suppresses the ice surface instability (the airfoil temperature is expected to be lower than the freezing temperature of water).

edge is constructed for predicting the roughness diameters as well as the presence of the smooth zones.

Based on the stagnation icing line model, the water film on the ice surface is assumed to be thin and passively conducting. The airflow's response to the change in ice shapes is faster than the rate of the ice growth, which suggests that the airflow can be considered to be steady on the ice growth time scale. The heat conduction within ice near the water/ice surface is three-dimensional. These observations are incorporated into the engineering linear stability model. Laminar airflow past a parabolic leading edge is considered. The thin conducting water film and a thin ice sheet of constant thickness lie underneath this airflow. Because, the temperature of the airfoil is not known in icing experiments, the present model uses a prescribed airfoil temperature with values varying between the freezing temperature of water and the free-stream stagnation temperature. Finally, the linear stability analysis is constructed using a parallel flow approximation. For a finite sweep angle, the steady airflow over the airfoil has a stagnation flow along the streamwise direction which affects the pressure distribution over the airfoil, and a spanwise flow along the attachment line which does not cause any changes in the pressure. Therefore, this airflow may be modeled as two-dimensional without any spanwise dependence. A boundary layer solution for the airflow is found using a low Mach number limit (see Section 5.2). This solution uses a temperature formulation similar to the one proposed by Rothmayer [48]. The boundary layer velocities as well as temperature are used to construct the input to the ice surface stability analysis. Since the ice and the air boundary layer are assumed to be thin, the normal direction at the airfoil surface for the stability calculations is taken to coincide with the normal direction for the boundary layer computations. A parallel flow approximation is used to arrive at a low Mach number incompressible formulation for the perturbed airflow (see Section 5.3). This model also includes the role of dissipation in the energy equation of the airflow. A normal mode analysis is then constructed to compute the growth rates of roughnesses

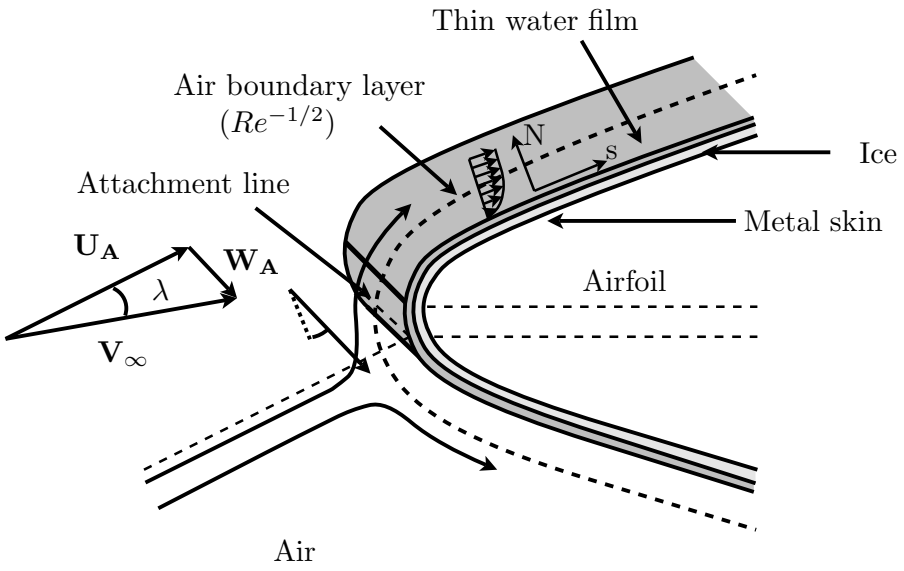

Figure 5.3 Boundary layer over a parabolic leading edge.

of different sizes. The flow conditions used in the experiments are used as input for the stability analysis.

5.2 Boundary layer equations

This section gives the boundary layer equations for the airflow over a parabolic leading edge and includes the flow along the streamwise direction as well as the spanwise flow along the attachment line. However, the linear stability analysis is performed only for unswept icing conditions, since the experimental data for roughness diameters is only available for these conditions.

The velocities at the attachment line are given by

$$U_A = V_\infty \cos(\lambda), \qquad W_A = V_\infty \sin(\lambda).$$

The streamwise and the normal coordinates within the boundary layer are given as $(s, Re^{-1/2}N)$ respectively. The velocities within the boundary layer may then be written

as $(U(s,N),\ Re^{-1/2}V(s,N),\ W(s,N))$. The non-dimensional temperature within the boundary layer is written as

$$T = 1 + \mathcal{T}\hat{T} + \ldots,$$

where $\mathcal{T}$ is the temperature perturbation defined earlier (see Section 3.3). The continuity equation then becomes

$$U_s + V_N = 0. \tag{5.1}$$

Similarly the momentum equations are obtained as

$$UU_s + VU_N = U_e U_{es} + U_{NN}, \tag{5.2}$$

$$0 = P_N, \tag{5.3}$$

$$UW_s + VW_N = W_{NN}, \tag{5.4}$$

where U_e is the inviscid slip velocity at the surface of the parabola. Using the relation between the temperature perturbation $\mathcal{T}$ and Mach number needed to include viscous heating, i.e. $M_\infty = m_\infty \mathcal{T}^{1/2}$, the energy equation becomes

$$U\hat{T}_s + V\hat{T}_N = -U(\gamma-1)m_\infty^2 U_e U_{es} + (\gamma-1)m_\infty^2 \left[\left(\frac{\partial U}{\partial N}\right)^2 + \left(\frac{\partial W}{\partial N}\right)^2\right] + \frac{\partial}{\partial N}\left(\frac{1}{\mathrm{Pr}}\frac{\partial \hat{T}}{\partial N}\right). \tag{5.5}$$

These equations are transformed using Görtler variables

$$\xi = \int_0^s U_e(s)ds, \quad \eta = \frac{U_e N}{\sqrt{2\xi}},$$

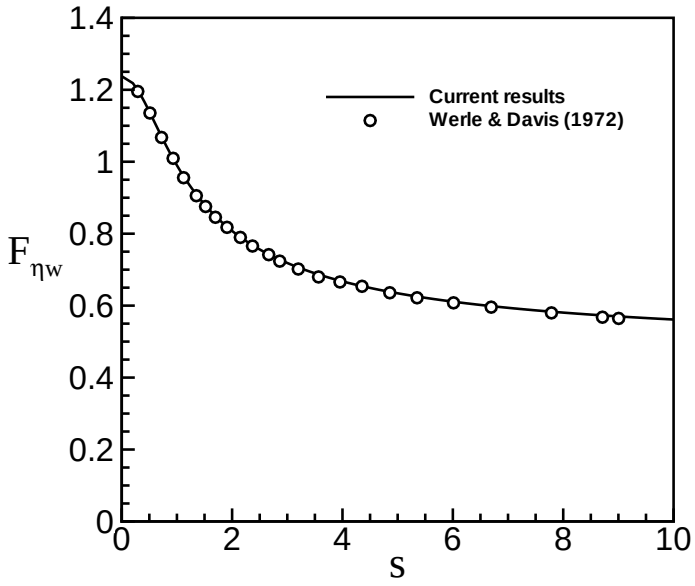

Figure 5.4 Comparison of the boundary layer skin friction parameter with the solution of Werle and Davis [6].

along with the velocities

$$U = U_e F(\xi,\eta), \quad \bar{V}(\xi,\eta) = \frac{\sqrt{2\xi}}{U_e} V + 2\xi\eta \frac{U_e'(s)}{U_e^2} F - \eta F, \quad W = W_e h(\xi,\eta).$$

The pressure gradient parameter is defined to be

$$\beta = 2\xi \frac{U_e'(s)}{U_e^2(s)} = 2\xi \frac{U_e'(\xi)}{U_e(\xi)}.$$

Using these variables, the normal component of the velocity may be written as

$$V = \frac{U_e}{\sqrt{2\xi}} \left[\bar{V} - 2\xi\eta \frac{U_e'(s)}{U_e^2} F + \eta F \right] = \frac{U_e}{\sqrt{2\xi}} \left[\bar{V} - \eta(\beta - 1) F \right].$$

The continuity and the momentum equations in terms of the transformed coordinates

are given by

$$\bar{V}_\eta + F + 2\xi F_\xi = 0, \tag{5.6}$$

$$F_{\eta\eta} - \bar{V}F_\eta + \beta(1 - F^2) - 2\xi F F_\xi = 0, \tag{5.7}$$

$$h_{\eta\eta} - \bar{V}h_\eta - 2\xi F h_\xi = 0, \tag{5.8}$$

where the third equation is for the spanwise velocity. The boundary conditions at the wall are given by $f(0) = f'(0) = 0$, and $h(0) = 0$. The boundary conditions at the edge of the boundary layer are $f'(\infty) = 1$, and $h(\infty) = 1$. The numerical scheme for computing the solution for Eqs. 5.6 through 5.8 is discussed later in Section 5.7. For details on the inviscid solution over a parabolic leading edge, refer to Werle and Davis [6]. A comparison of the boundary layer skin friction parameter computed from Eqs. 5.6 and 5.7 is shown in Fig. 5.4 where w denotes $\eta = 0$. Although the sweep velocity is not being used in the present comparison with experiments in this chapter, the wall shear stress due to the sweep velocity is shown in Fig. 5.5 for completeness and possible future work in swept wing icing. The energy equation reduces to

$$\begin{aligned}\frac{1}{\mathrm{Pr}}\hat{T}_{\eta\eta} - \bar{V}\hat{T}_\eta - 2\xi F\hat{T}_\xi = &-\left[-F(\gamma-1)m_\infty^2 2\xi U_{es}\right] \\ &-(\gamma-1)m_\infty^2\left[(U_e F_\eta)^2 + (W_e h_\eta)^2\right].\end{aligned} \tag{5.9}$$

An expression for temperature similar to Rothmayer [48] may be used, where

$$\hat{T} = \pm[e(\xi,\eta) - 1] + \frac{\gamma-1}{2}m_\infty^2[e(\xi,\eta) - U_e^2 g(\xi,\eta) - W_e^2 k(\xi,\eta)], \tag{5.10}$$

and $W_e^2 k(\xi,\eta)$ incorporates the viscous dissipation due to the sweep velocity. The equa-

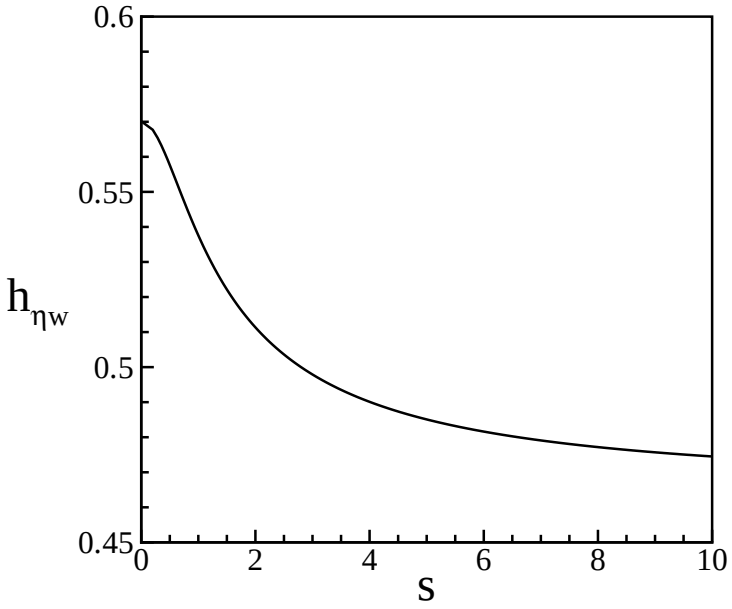

Figure 5.5 Wall shear stress due to the flow along the attachment line.

tions for the temperatures are given by

$$\frac{1}{\mathrm{Pr}} e_{\eta\eta} - \bar{V} e_\eta - 2\xi F e_\xi = 0, \tag{5.11}$$

$$\frac{1}{\mathrm{Pr}} g_{\eta\eta} - \bar{V} g_\eta - 2\beta F g - 2\xi F g_\xi = 2\left(F_\eta^2 - \beta F\right), \tag{5.12}$$

$$\frac{1}{\mathrm{Pr}} k_{\eta\eta} - \bar{V} k_\eta - 2\xi F k_\xi = 2h_\eta^2. \tag{5.13}$$

The boundary conditions at the wall are $e(0) = 0, g(0) = 0$ and $k(0) = 0$. The boundary conditions at the edge of the boundary layer are $e(\infty) = 1$, $g(\infty) = 1$ and $k(\infty) = 1$. The numerical scheme for computing the solution for Eqs. 5.11 through 5.13 is discussed later in Section 5.7. The solution for the heat fluxes due to the temperatures $e(\eta)$, $g(\eta)$ and $k(\eta)$ are shown in Figs. 5.6 through 5.8. Currently the dissipation due to the sweep velocity is not being used, i.e. $W_e = 0$. The temperatures $e(\eta)$ and $g(\eta)$ are used to construct the temperature within the boundary layer for the low Mach number limit.

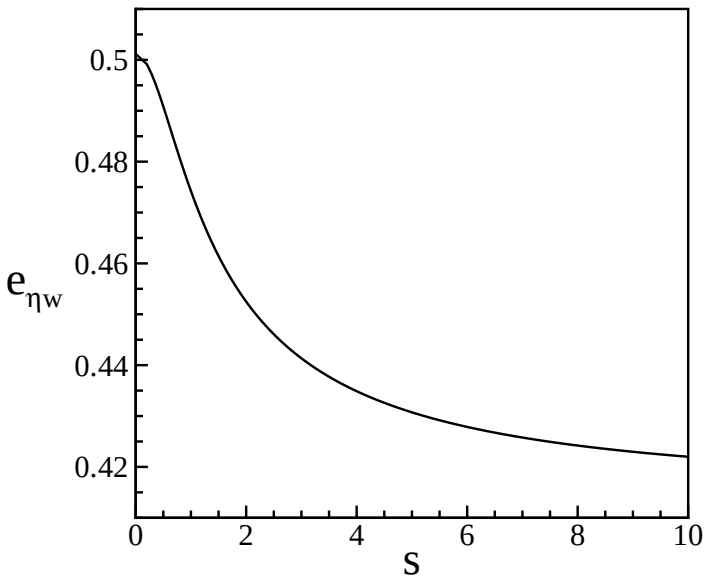

Figure 5.6 The heat flux component e_η at the wall.

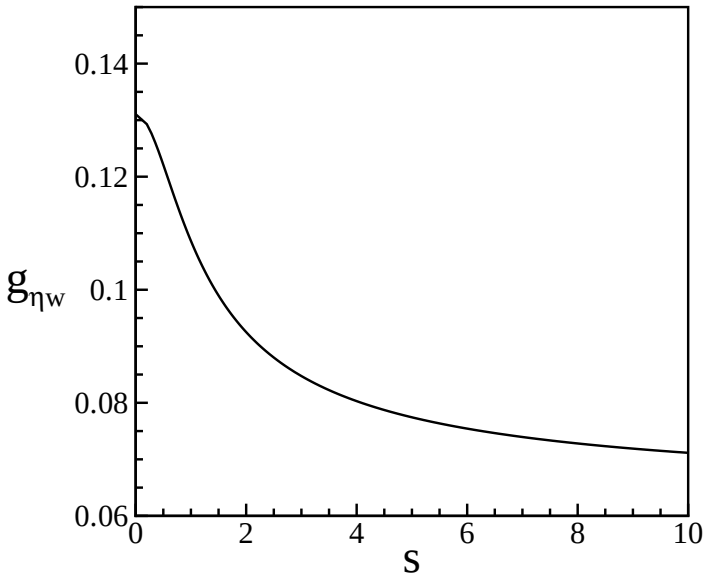

Figure 5.7 The heat flux component g_η at the wall.

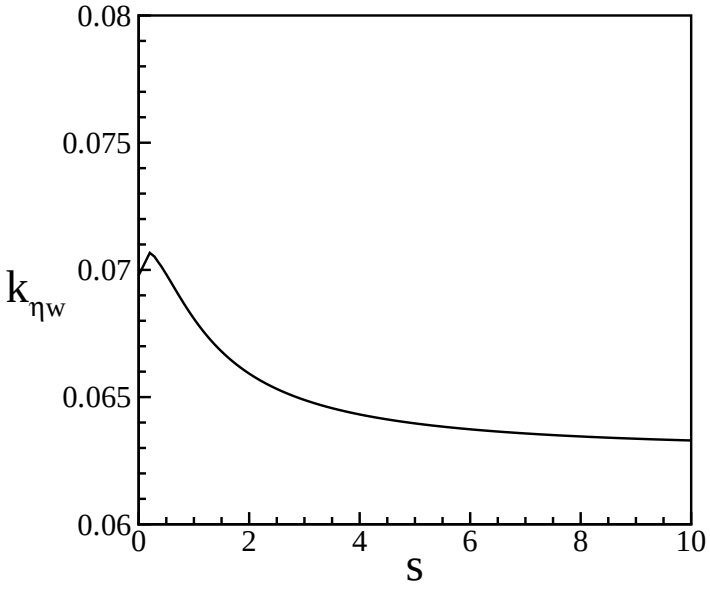

Figure 5.8 The heat flux component k_η at the wall.

5.3 Equations for the airflow and ice growth

In order to investigate the stability of the ice surface, the full Navier Stokes equations are considered in the airflow. A thin conducting water film is present underneath the airflow and ice forms beneath this water film. A small section of the airfoil is considered, where both water and ice are present beneath the airflow. The variables within the airflow may be written as

$$(\rho, u, v, w, P, T) \sim (1, \bar{u}, \bar{v}, \bar{w}, \bar{P}, 1) + M_\infty^2(\bar{\rho}, u_1, v_1, w_1, P_1, \bar{T}) + \dots .$$

The non-dimensional ideal gas relation $1 + \gamma M_\infty^2 P = \rho T$ yields $\gamma \bar{P} = \bar{\rho} + \bar{T}$. Starting from the continuity equation in the airflow (Eq. 2.21), when a steady airflow is assumed, it is found that

$$(\bar{u}_x + \bar{v}_y + \bar{w}_z) + M_\infty^2(u_{1,x} + v_{1,y} + w_{1,z} + \bar{\rho}_x\bar{u} + \bar{\rho}_y\bar{v} + \bar{\rho}_z\bar{w}) + \ldots = 0. \qquad (5.14)$$

Then the continuity equation at the leading order becomes

$$\bar{u}_x + \bar{v}_y + \bar{w}_z = 0. \tag{5.15}$$

The low Mach number momentum equations at the leading order then become

$$\begin{aligned}
\bar{u}\bar{u}_x + \bar{v}\bar{u}_y + \bar{w}\bar{u}_z &= -\bar{P}_x + Re^{-1}\left[\bar{u}_{xx} + \bar{u}_{yy} + \bar{u}_{zz}\right], && (5.16)\\
\bar{u}\bar{v}_x + \bar{v}\bar{v}_y + \bar{w}\bar{v}_z &= -\bar{P}_y + Re^{-1}\left[\bar{v}_{xx} + \bar{v}_{yy} + \bar{v}_{zz}\right], && (5.17)\\
\bar{u}\bar{w}_x + \bar{v}\bar{w}_y + \bar{w}\bar{w}_z &= -\bar{P}_z + Re^{-1}\left[\bar{w}_{xx} + \bar{w}_{yy} + \bar{w}_{zz}\right]. && (5.18)
\end{aligned}$$

For the energy equation (Eq. 2.23), it becomes necessary to consider higher order velocities in the continuity equation. The non-dimensional energy equation is then written as

$$\begin{aligned}
(1 + M_\infty^2\bar{\rho})\left[(\bar{u} + M_\infty^2 u_1)M_\infty^2\bar{T}_x + (\bar{v} + M_\infty^2 v_1)M_\infty^2\bar{T}_y + (\bar{w} + M_\infty^2 w_1)M_\infty^2\bar{T}_z\right] =\\
-(\gamma-1)(\bar{u}_x + \bar{v}_y + \bar{w}_z) - (\gamma-1)(M_\infty^2(\bar{\rho} + \bar{T})(\bar{u}_x + \bar{v}_y + \bar{w}_z) + M_\infty^2(u_{1,x} + v_{1,y} + w_{1,z}))\\
+\gamma(\gamma-1)M_\infty^2 Re^{-1}\Phi + Re^{-1}\frac{\gamma}{\mathrm{Pr}}M_\infty^2\left[\bar{T}_{xx} + \bar{T}_{yy} + \bar{T}_{zz}\right] + \ldots,
\end{aligned}$$

where the viscous dissipation in the airflow Φ is given by

$$\begin{aligned}
\Phi &= 2\bar{u}_x^2 + \bar{u}_y^2 + \bar{u}_z^2 + \bar{v}_x^2 + 2\bar{v}_y^2 + \bar{v}_z^2 + \bar{w}_x^2 + \bar{w}_y^2 + 2\bar{w}_z^2\\
&\quad + \bar{u}_y\bar{v}_x + \bar{u}_z\bar{w}_x + \bar{v}_x\bar{u}_y + \bar{v}_z\bar{w}_y + \bar{w}_x\bar{u}_z + \bar{w}_y\bar{v}_z.
\end{aligned}$$

When the continuity equation (Eq. 5.15) is used and the terms at $\mathcal{O}(M_\infty^2)$ are retained, the energy equation reduces to

$$\bar{u}\bar{T}_x + \bar{v}\bar{T}_y + \bar{w}\bar{T}_z = -(\gamma-1)(u_{1,x} + v_{1,y} + w_{1,z}) \\ +\gamma(\gamma-1)Re^{-1}\Phi + Re^{-1}\frac{\gamma}{\mathrm{Pr}}\left[\bar{T}_{xx} + \bar{T}_{yy} + \bar{T}_{zz}\right].$$

When the higher order continuity equation is considered in Eq. 5.14, it is found that

$$u_{1,x} + v_{1,y} + w_{1,z} = -(\bar{\rho}_x\bar{u} + \bar{\rho}_y\bar{v} + \bar{\rho}_z\bar{w}).$$

Using the fact that the pressure $\bar{P}$ changes only with the streamwise direction and $\gamma\bar{P} = \bar{\rho} + \bar{T}$, the higher order continuity equation yields

$$u_{1,x} + v_{1,y} + w_{1,z} = -((\gamma\bar{P}_x - \bar{T}_x)\bar{u} + (-\bar{T}_y)\bar{v} + (-\bar{T}_z)\bar{w}).$$

Using the above and collecting terms, the energy equation then finally becomes

$$\bar{u}\bar{T}_x + \bar{v}\bar{T}_y + \bar{w}\bar{T}_z = (\gamma-1)\bar{u}\bar{P}_x + (\gamma-1)Re^{-1}\Phi + Re^{-1}\frac{1}{\mathrm{Pr}}\left[\bar{T}_{xx} + \bar{T}_{yy} + \bar{T}_{zz}\right]. \quad (5.19)$$

The above low Mach number equations for air are directly coupled to the local heat conduction problem within the ice. The equation for heat conduction is

$$T_{xx} + T_{yy} + T_{zz} = 0. \quad (5.20)$$

At the ice surface, the temperature is specified using the Gibbs-Thomson relation $T = T_{freezing}(1 - \varepsilon\kappa_{ice})$, where $\kappa_{ice} = -\partial_x^2 f_{ice}[1 + (\partial_x f_{ice})^2]^{-3/2} - \partial_z^2 f_{ice}[1 + (\partial_z f_{ice})^2]^{-3/2}$ and $\varepsilon = \gamma^*_{g,ice/water}/(\rho^*_{ice}H^*_{ice/water}L)$. The Stefan condition at the water/ice interface is given

by

$$\left(\frac{\partial T}{\partial y}\right)_{water} = \frac{k_{ice}}{k_{water}} K_{iw} \left(\frac{\partial T}{\partial y}\right)_{ice} - \frac{\Pr}{K_{wa} C_{ai}} Ste^{-1} D_{aw}^{-1} Re D_{iw} \frac{df_{ice}}{dt}. \tag{5.21}$$

Since a thin water film assumption is being used, the heat flux from the airflow is used in the Stefan condition (also see Section 2.4), i.e.

$$K_{wa} \left[\frac{\partial T}{\partial y}\right]_{water} = M_\infty^2 \left[\frac{\partial \bar{T}}{\partial y}\right]_{air}.$$

5.4 Formulation for ice surface instability problem

A parallel flow approximation is used for investigating the ice surface stability, which leads to the leading order flow variables being functions of the normal coordinate only. For the linear stability analysis for the ice surface stability problem, the velocities and the pressure in the airflow are given by

$$\begin{aligned}(\bar{u}, \bar{v}, \bar{w}, \bar{P}) \sim\ & (u_0(y), v_0(y), w_0(y), P_0(y)) \\ & + \epsilon (u_2(y), v_2(y), w_2(y), p_2(y)) e^{i(\alpha x + \beta z - \omega t)} + \ldots,\end{aligned}$$

and the density and temperature are

$$(\bar{\rho}, \bar{T}) \sim (\rho_1(y), T_1(y)) + \epsilon (\rho_2(y), T_2(y)) e^{i(\alpha x + \beta z - \omega t)} + \ldots .$$

Here, the streamwise and spanwise wave numbers are α and β respectively. Note that $u_0(y)$, $v_0(y)$, $w_0(y)$, $P_0(y)$, $\rho_1(y)$, and $T_1(y)$ are defined later. The temperature within ice is then written as

$$T \sim T_0(y) + \epsilon T_2(y) e^{i(\alpha x + \beta z - \omega t)} + \ldots .$$

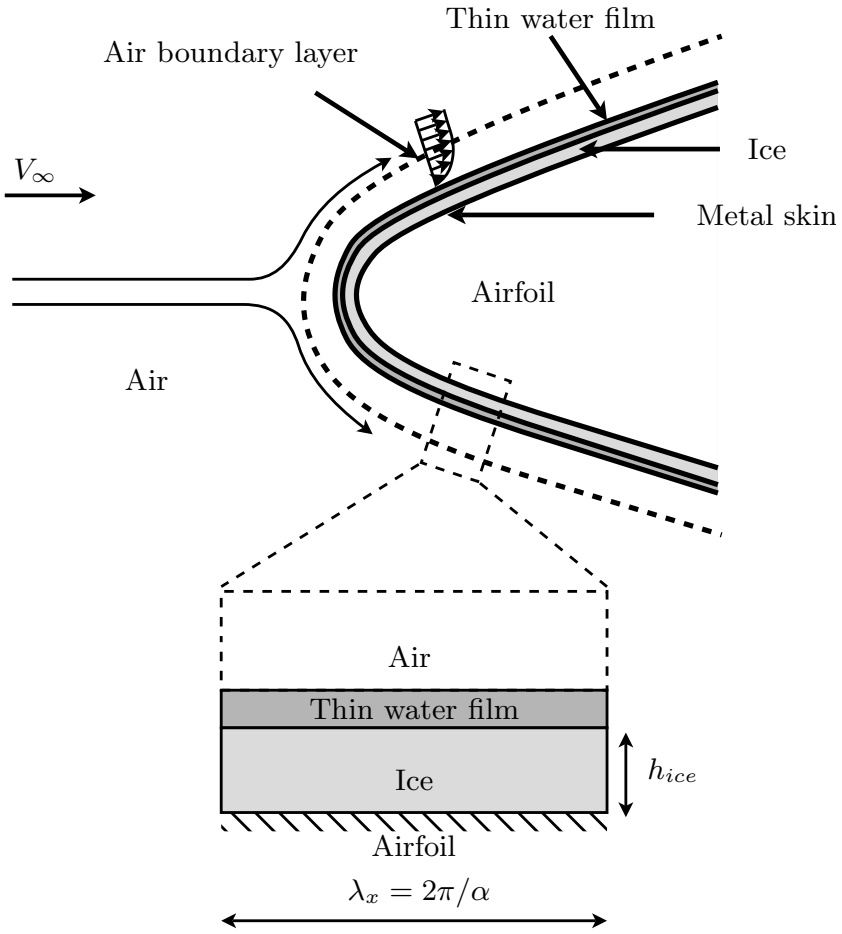

Figure 5.9 The linear stability problem for icing surface instabilities over a parabolic leading edge covered by a thin sheet of ice (the boxed region is the domain for the linear stability computations).

The mean ice height is given by H_{ice}. The total ice height is then written as

$$\bar{f}_{ice} \sim H_{ice} + \epsilon f_{1,ice} e^{i(\alpha x + \beta z - \omega t)} + \dots .$$

The equations derived in the previous section (Eqs. 5.15 through 5.21) are used here to construct the linearized equations. The ideal gas relation for the perturbation quantities becomes $\gamma p_2 = \rho_2 + T_2$. The continuity equation becomes

$$i\alpha u_2 + v_{2,y} + i\beta w_2 = 0. \tag{5.22}$$

A parallel flow assumption is used where the contribution of only the derivatives in the vertical coordinate are considered, and streamwise and spanwise derivatives of the leading order variables are not being considered. Then the linearized momentum equations for the perturbation variables are found to be

$$\begin{aligned}
i\alpha u_0 u_2 + v_2 u_{0,y} + v_0 u_{2,y} + i\beta w_0 u_2 &= -i\alpha p_2 + Re^{-1}(u_{2,yy} - (\alpha^2+\beta^2)u_2), & (5.23)\\
i\alpha u_0 v_2 + v_2 v_{0,y} + v_0 v_{2,y} + i\beta w_0 v_2 &= -p_{2,y} + Re^{-1}(v_{2,yy} - (\alpha^2+\beta^2)v_2), & (5.24)\\
i\alpha u_0 w_2 + v_2 w_{0,y} + v_0 w_{2,y} + i\beta w_0 w_2 &= -i\beta p_2 + Re^{-1}(w_{2,yy} - (\alpha^2+\beta^2)w_2). & (5.25)
\end{aligned}$$

Similarly, the linearized energy equation is given by

$$\begin{aligned}
&i\alpha u_0 T_2 + v_2 T_{1,y} + v_0 T_{2,y} + i\beta w_0 T_2 = -(\gamma-1)u_0 i\alpha p_2 \\
&+(\gamma-1)Re^{-1}\left(2u_{0,y}u_{2,y} + 4v_{0,y}v_{2,y} + 2w_{0,y}w_{2,y} + 2(i\alpha u_{0,y} + i\beta w_{0,y})v_2\right) \\
&+Re^{-1}\frac{1}{\mathrm{Pr}}\left(T_{2,yy} - (\alpha^2+\beta^2)T_2\right). \qquad (5.26)
\end{aligned}$$

At the wall, the linearized variables are given by

$$u_2(0) = -u_{0,y}(0) f_{1,ice}, \quad v_2(0) = -v_{0,y}(0) f_{1,ice},$$
$$w_2(0) = -w_{0,y}(0) f_{1,ice}, \quad T_2(0) = -T_{1,y}(0) f_{1,ice}.$$

The following Squire's transformation is used for the perturbation variables

$$U = i\alpha u_2 + i\beta w_2, \qquad P = (\alpha^2 + \beta^2) p_2, \quad V = i\alpha v_2, \quad F_{ice} = i\alpha f_{1,ice}.$$

A similar transformation is also used for the leading order variables which is given by

$$U_0 = \frac{\alpha u_0 + \beta w_0}{\alpha}, \quad V_0 = v_0.$$

Using these transformations, the continuity equation becomes

$$i\alpha U + V_y = 0. \tag{5.27}$$

The x- and z-momentum equations are combined to obtain

$$i\alpha U_0 U + V U_{0,y} + V_0 U_y = P + Re^{-1}(U_{yy} - (\alpha^2 + \beta^2) U). \tag{5.28}$$

The y-momentum equation is tranformed into

$$i\alpha U_0 V + V V_{0,y} + V_0 V_y = -\frac{i\alpha}{\alpha^2 + \beta^2} P_y + Re^{-1}(V_{yy} - (\alpha^2 + \beta^2) V). \tag{5.29}$$

Pressure is then removed from the momentum equations by using expressions for stream function and vorticity, given by

$$U = \Psi_y, \qquad V = -i\alpha\Psi, \quad \Omega = U_y + \frac{\alpha^2 + \beta^2}{i\alpha} V.$$

The equations for Ψ and Ω then reduce to

$$\Omega = \Psi_{yy} - (\alpha^2 + \beta^2)\Psi, \tag{5.30}$$

$$(i\alpha U_0 + V_{0,y})\Omega + V_0\Omega_y - i\alpha\Psi U_{0,yy} = Re^{-1}(\Omega_{yy} - (\alpha^2 + \beta^2)\Omega). \tag{5.31}$$

At the wall, $\Psi_y = -U_{0,y}F_{ice}$, $\Psi = 0$, $\Omega = \Psi_{yy}$. At the free-stream,$\Psi_y = 0$, $\Omega = 0$. The heat equation for the perturbation temperature in ice is given by

$$T_{2,yy} - (\alpha^2 + \beta^2)T_2 = 0. \tag{5.32}$$

The perturbation temperature at the ice surface is found to be

$$T_2(0) = -T_{0,y}(0)f_{1,ice} - \varepsilon T_{freezing}(\alpha^2 + \beta^2)f_{1,ice}. \tag{5.33}$$

The perturbation temperature in ice at the airfoil surface is $T_2(0) = 0$, because the geometry of the airfoil is fixed and is not subject to small perturbations experienced by the ice surface above it. Using the perturbation quantitiesin the Stefan condition, the local ice growth rate is found to be

$$\omega = i\left[\frac{k_{ice}}{k_{water}}K_{iw}\left(T_{2,y}\right)_{ice} - \left(T_{2,y}\right)_{water}\right] / \left[\Pr\frac{ReD_{iw}}{K_{wa}C_{ai}D_{aw}Ste}f_{1,ice}\right], \tag{5.34}$$

where the heat flux within water is obtained from

$$M_\infty^2\left(T_{2,y}\right)_{air} = K_{wa}\left(T_{2,y}\right)_{water},$$

and $\left(T_{2,y}\right)_{air}$ is evaluated at the ice surface.

5.5 Inputs to ice surface instability problem

The linear ice surface stability problem of Section 5.4 requires the leading order velocities as input for the computation of the growth of the ice sheet. These leading order velocities or temperature may be obtained from Navier-Stokes computations as well as boundary layer equations. For the linear stability analysis in this chapter, the input velocities and temperature are computed using the solution of the boundary layer equations given in Section 5.2, which are found to be

$$u_0 = U = U_e F(\xi,\eta), \tag{5.35}$$

$$v_0 = Re^{-1/2}V = Re^{-1/2}\frac{U_e}{\sqrt{2\xi}}\left[\bar{V}(\xi,\eta) - \eta(\beta-1)F(\xi,\eta)\right], \tag{5.36}$$

$$w_0 = W = W_e h(\xi,\eta), \tag{5.37}$$

$$T_1 = \frac{1}{m_\infty^2}\hat{T} = \frac{1}{m_\infty^2}\left[\pm[e(\xi,\eta)-1] + \frac{(\gamma-1)}{2}m_\infty^2[e(\xi,\eta) - U_e^2 g(\xi,\eta) - W_e^2 k(\xi,\eta)]\right]. \tag{5.38}$$

The gradient of the boundary layer velocity and temperature profiles in the normal direction are also inputs to the linear stability problem. Again, using the solution of the boundary layer equations, these are found to be

$$\frac{\partial u_0}{\partial y} = Re^{1/2}\frac{U_e^2}{\sqrt{2\xi}}F_\eta, \tag{5.39}$$

$$\frac{\partial v_0}{\partial y} = \frac{U_e^2}{2\xi}\left[\bar{V}_\eta - \eta(\beta-1)F_\eta - (\beta-1)F\right], \tag{5.40}$$

$$\frac{\partial w_0}{\partial y} = Re^{1/2}\frac{U_e}{\sqrt{2\xi}}W_e h_\eta, \tag{5.41}$$

$$\frac{\partial T_1}{\partial y} = Re^{1/2}\frac{1}{m_\infty^2}\frac{U_e}{\sqrt{2\xi}}\left[\pm e_\eta + \frac{\gamma-1}{2}m_\infty^2[e_\eta - U_e^2 g_\eta - W_e^2 k_\eta]\right]. \tag{5.42}$$

A typical wall shear stress and surface heat flux within the boundary layer are shown in Figs. 5.10 and 5.11 respectively. Here the change in shear stress and the heat flux in

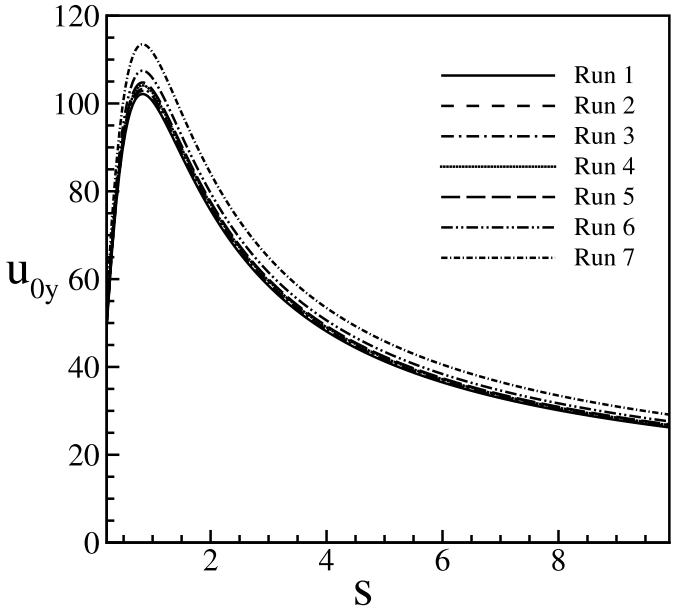

Figure 5.10 Typical wall shear stress as input for the linear stability problem (see Eq. 5.39, and Table 5.1 for the definitions of Runs 1-7).

the boundary layer is due to the increasing nose radius of curvature for the airfoil/ice surface geometry which occurs to the increasing ice height with time (see the following section section 5.6).

5.6 Key parameters from experiments

The icing experiments, mentioned earlier, use a set of scaling parameters to maintain similitude of ice accretion in different test conditions. Anderson [65] explains in detail the various icing scaling methods, some of which are described in this section and these will be used when making a comparison with the experimental results for roughness diameters and smooth zones.

The non-dimensional momentum equation describing the droplet trajectory (see

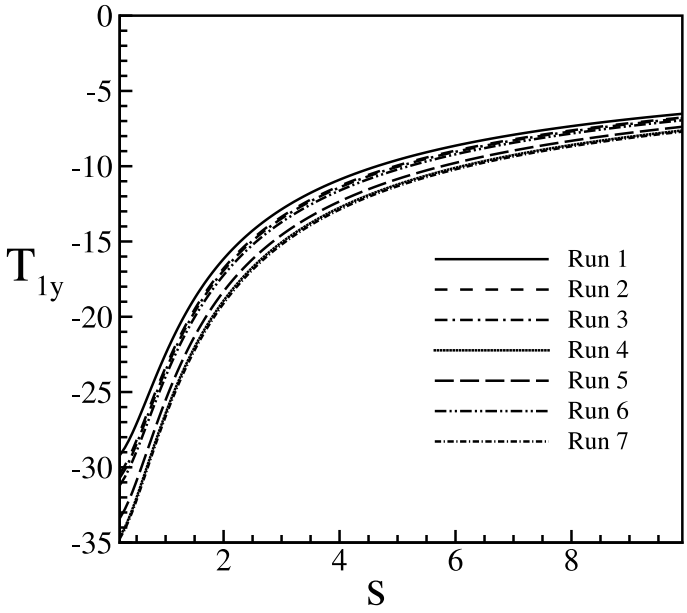

Figure 5.11 Typical wall temperature gradient as input for the linear stability problem (see Eq. 5.42, and Table 5.1 for the definitions of Runs 1-7).

Bragg [66] and Ruff [67]) is given by

$$K\ddot{\tilde{x}} = \frac{C_D R_{rel}}{24}(\tilde{u} - \dot{\tilde{x}})$$

where $\tilde{u}$, $\tilde{x}$ are the non-dimensional velocity and position of the droplet respectively and the drag acting on the droplet is given by $\frac{C_D R_{rel}}{24}$. The Reynolds number of the droplet Re_{rel} is given by

$$Re_{rel} = \frac{\rho^*_{air}(V_\infty \left|\tilde{u} - \dot{\tilde{x}}\right|)\delta}{\mu^*_{air}} = Re_\delta \left|\tilde{u} - \dot{\tilde{x}}\right|,$$

and the droplet Reynolds number Re_δ based on the freestream velocity is defined as

$$Re_\delta = \frac{\rho^*_{air} V_\infty \delta}{\mu^*_{air}}. \tag{5.43}$$

Here, an inertia parameter is also used which is defined by Langmuir and Blodgett [68] as

$$K = \frac{\rho_{water}\delta^2 V_\infty}{18 d \mu^*_{air}}, \tag{5.44}$$

where δ is the Median Volumetric Diameter (MVD) of the water droplet distribution, and d is twice the nose radius of curvature. A typical spray of droplets in icing experiments consists of water droplets with varying diameters. The Median Volumetric Diameter is defined as the diameter of a droplet in a droplet distribution which divides the droplets equally by number into droplets having larger and smaller diameters. It has been observed that the droplet motion in the airflow and their resulting impingement and mass accumulation on the surface can be effectively represented by this diameter. In order to maintain similarity of droplet trajectories, both the inertia parameter of the droplet as well as the non-dimensional droplet drag need to be the same in both test conditions (see Anderson [65]). This is satisfied by defining a modified inertia parameter, which is

$$K_0 = \frac{1}{8} + \frac{\lambda}{\lambda_{Stokes}}\left(K - \frac{1}{8}\right), \qquad K > \frac{1}{8}. \tag{5.45}$$

Here, λ/λ_{Stokes} is a dimensionless range parameter which gives the ratio of the range of the droplet with the actual drag and its range if it is released in still air with an initial velocity of V. For the case when the modified inertia parameter $K_0 \leq 1/8$, droplet impingement will not occur (see Anderson [65] and Langmuir and Blodgett [68]). The non-dimensional range parameter λ/λ_{Stokes} was computed by Langmuir and Blodgett [68] using the droplet Reynolds number Re_δ. Both the inertia parameter K and the droplet Reynolds number Re_δ may be computed using the Median Volumetric Diameter (MVD) reported in experimental results. A fit to the results of Langmuir and Blodgett

[68] (see Anderson [65] for detailed discussion) for the non-dimensional range parameter is given by

$$\frac{\lambda}{\lambda_{Stokes}} = \left(0.8388 + 0.001483 Re_\delta + 0.1847\sqrt{Re_\delta}\right)^{-1}. \tag{5.46}$$

The local collection efficiency of water over the surface is defined as a projection of the stream tube which follows the droplet trajectories from the free-stream airflow to the airfoil surface and varies over the airfoil depending on the local droplet trajectories. The collection efficiency at the stagnation line, β_0, is often considered a key parameter in icing scaling which may be obtained from the modified inertia parameter using the empirical relation

$$\beta_0 = \frac{1.40\left(K_0 - \frac{1}{8}\right)^{0.84}}{1 + 1.40\left(K_0 - \frac{1}{8}\right)^{0.84}}, \tag{5.47}$$

when the non-dimensional inertia parameter $K \leq 7.5$. The ice height in different test conditions needs to be similar with respect to the size of the airfoil. This is determined by considering the ice height at the stagnation line. The ice accretion at the stagnation line (and at other downstream locations as well) depends on the mass of water accumulated on the surface due to the airflow velocity, the liquid water content of the supercooled water droplets in the airflow, the time for ice accretion, the fraction of this water being frozen, and the similarity of droplet trajectories. The similarity of the droplet trajectories is maintained by the stagnation collection efficiency β_0. The total mass of water deposited onto the surface is given by a non-dimensional accumulation parameter A_c, which is defined by

$$A_c = \frac{LWC^* V_\infty \tau}{\rho^*_{ice} d}, \tag{5.48}$$

where τ is the time for ice accretion, LWC^* is the liquid water content in the airflow

(see Section 2.2), ρ_{ice} is the density of ice and d is twice the nose radius of curvature of the leading edge of the airfoil. The freezing fraction n_0 is defined as the fraction of water reaching the airfoil which freezes. The ice height at the stagnation line is then given by

$$\frac{\Delta_0}{d} = n_0 A_c \beta_0, \tag{5.49}$$

where Δ_0 is the ice height. Typical examples of these non-dimensional parameters are given in Table 5.1. The ice height is computed for these flow conditions using the icing scaling parameters mentioned in this section. This ice height is used for computing the heat flux within the ice for the linear stability problem (see Section 5.6.1).

5.6.1 Approach for comparison with experiments

The experimental parameters (given in Table 5.1) are used to compute the stagnation ice height. This ice height is then used in the computation of heat flux for the main ice sheet as an input to the linear stability problem. The exact airfoil temperature is not known (and is not measured in the experiments). The correct approach is to compute the heat conduction problem for the airfoil skin and the interior of the wing along with the heat conduction within ice given known initial conditions from the experiment. In general, it is expected that the airfoil skin will be at some temperature between or near the freestream stagnation temperature of the airflow and the freezing temperature of water with a temperature variation in the streamwise direction. As the ice accretion progresses, the temperature of the airfoil skin is expected to become closer to the freezing temperature of water. Hence, to perform the computations for the linear stability problem, some assumption must be made for the airfoil temperature in order to obtain the heat flux within the ice. Here, this assumption is that the airfoil surface is held at some constant temperature which is between the stagnation temperature of the airflow and the freezing temperature of water.

Table 5.1 Roughness diameters and smooth zones as seen in experiments (see Anderson, Hentschel and Ruff [1]).

Run	T_∞ (^oC)	V_∞ (m/s)	MVD (μm)	LWC^* (g/m^3)	$t(s)$	A_c	n_0	W_S (mm)	D_r (mm)
1	-5.6	67.1	29.9	1	14	0.061	0.216	23.2	0.573
2	-5.7	67.0	30.1	1	22	0.096	0.219	24.4	0.660
3	-5.7	66.9	30.1	1	27	0.117	0.222	23.8	0.691
4	-6.1	66.8	30.2	1	34	0.148	0.240	23.8	0.959
5	-5.9	66.6	30.1	1	43	0.186	0.234	14.1	0.908
6	-5.6	66.8	30.0	1	75	0.326	0.217	7.6	1.020
7	-5.7	66.3	30.1	1.01	147	0.639	0.220	3.8	1.063

5.7 Numerical solution

A Crank-Nicolson scheme in ξ with central differencing in η is used to compute the boundary layer equations (Eqs. 5.6 through 5.13, see Werle and Davis [6]). Using the experimental conditions, the inputs to the linear stability problem are constructed (see Section 5.5). Thereafter, a coupled central differencing scheme in η is used to solve the streamfunction-vorticity equations 5.30 and 5.31 for the linear stability problem. At the wall, a fictitious grid point is added to impose the boundary conditions $\Psi_y = -U_0 F_{ice}\,\Psi = 0$, $\Omega = \Psi_{yy}$ which gives

$$\frac{1}{\Delta y^2}\Psi_2 - \Omega_1 = -2\frac{1}{\Delta y}U_0 F_{ice}.$$

After obtaining the solution of the streamfunction and vorticity, the normal component of the perturbation velocity is obtained as $v_2 = -\Psi$, because $V = i\alpha v_2 = -\Psi_x$ in Section 5.4. Pressure for the linear stability problem is obtained from

$$p_2 = (i\alpha U_0 \Psi_y - i\alpha \Psi U_{0,y} + V_0 \Psi_{yy} - Re^{-1}\Omega_y)/(\alpha^2 + \beta^2).$$

u_2 is obtained from solving Eq. 5.23. Then, w_2 is obtained from $U = \Psi_y$ using the solution for u_2. The perturbation temperature within the airflow is computed using the energy equation where the perturbation velocities and pressure as well as the leading order velocity profiles are the input, i.e.

$$\left[-\frac{v_0}{2\Delta y} - Re^{-1}\frac{1}{\mathrm{Pr}}\frac{1}{\Delta y^2}\right]T_{2,j-1} + \left[Re^{-1}\frac{1}{\mathrm{Pr}}(\frac{2}{\Delta y^2} + \alpha^2 + \beta^2) + (i\alpha u_0 + i\beta w_0)\right]T_{2,j}$$
$$+ \left[\frac{v_0}{2\Delta y} - Re^{-1}\frac{1}{\mathrm{Pr}}\frac{1}{\Delta y^2}\right]T_{2,j+1} = -(\gamma-1)u_0 i\alpha p_2 - v_2 T_{1,y}$$
$$+(\gamma-1)Re^{-1}\left(2u_{0,y}u_{2,y} + 4v_{0,y}v_{2,y} + 2w_{0,y}w_{2,y} + i\alpha 2u_{0,y}v_2 + i\beta 2w_{0,y}v_2\right).$$

A grid stretching is used as in the stagnation/attachment line icing problem discussed earlier. The temperature of the airfoil beneath the ice is varied over a range of values close to the freezing temperature of water. A uniformly thin ice height is assumed over the airfoil, which is approximated from Eq. 5.49 for the given experimental conditions using the scaling parameters mentioned earlier in Section 5.6 (details are provided in subsequent section 5.8). This ice height is then used to compute the leading order heat flux within the ice $T_{1,y}$ and is used in the boundary condition for the perturbation temperature at the ice surface (Eq 5.33). Both the linearized airflow and heat conduction within ice are computed with $f_{1,ice} = 1$ and selected streamwise and spanwise wave numbers, α and β. The heat fluxes within air and ice are then computed which are used to evaluate the growth rate for the ice surface (Eq. 5.34).

5.8 Results and discussion

The series of test conditions chosen for prediction of roughness diameters and the smooth zone using the linear stability model is taken from Test Series A of Anderson, Hentschel and Ruff [1] (Table 5.1). Here the free-stream temperature is kept close to -5.7 ^oC and the free-stream velocity is approximately 67 m/s. This also ensures the

free-stream total temperature is almost the same in all the conditions. The chosen icing experiments were conducted on 5/30/96 for airfoil with chord length 53.3 cm and these experiments provide data for both the smooth zone as well as the roughness diameters. For the different conditions (Run 1 through 7 in Table 5.1), the accumulation parameter A_c gradually increases with increasing time for ice accretion and the stagnation freezing fraction n_0 is approximately constant. The ice height is computed from Eq. 5.49, which uses the accumulation parameter A_c, the stagnation freezing fraction n_0 and the stagnation collection efficiency β_0. Both the parameters A_c and n_0 are given in the experimental data. The collection efficiency β_0 is computed from Eq. 5.47 for which Eqs. 5.44 through 5.46 are computed using the Median Volumetric Diameter.

The increase in the accumulation parameter A_c effectively represents an increase in the ice height (see Fig. 5.12). For a fixed accumulation parameter ($A_c = 0.096$), Fig. 5.13 shows a grid independence check for Run 2 of Table 5.1 where, for the fine grid ($\bigcirc$), the number of η grid points in the airflow is 151, the number of grid points in s is 451 and the number of grid points in η inside the ice is 81, and for the coarse grid, the number of η grid points in the airflow is 101, the number of grid points in s is 401 and the number of grid points in η inside the ice is 51. The number of grid points for the wave numbers in the streamwise and spanwise directions are (N_α, N_β) = (401, 401) and (N_α, N_β) = (101, 101) for the coarse grid. For the fine grid, (N_α, N_β) = (101, 101). Here, the temperature of the airfoil is kept at 273 K and the maximum growth rate for each location is shown with respect to increasing streamwise distance s. Using a range of streamwise and spanwise wavelengths, the growth rates at each location are computed. The maximum growth rate for these wavelengths is then reported with respect to location and this is shown in Fig. 5.13. The streamwise wavelength is arbitrarily catagorized as long if $\lambda_x > 2s$ or short if $\lambda_x < 2s$, where s is the streamwise location. The parallel flow approximation used in the derivation of the linear stability problem is no longer valid for the "long" wave lengths because these wave lengths are much larger than the thickness

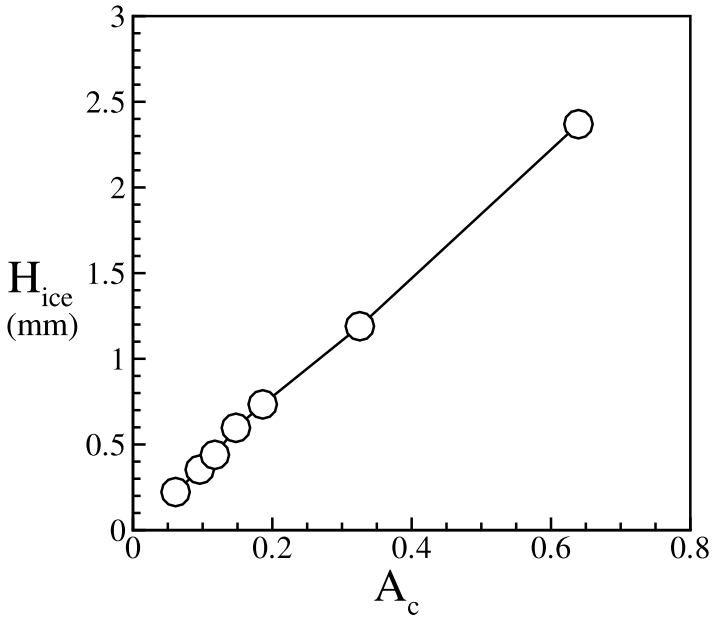

Figure 5.12 Estimated ice heights for increasing accumulation parameter (see Section 5.6 and Table 5.1).

of the air boundary layer. It is seen that a long wave length solution predominates the growth rates near the stagnation line. As the streamwise distance increases, there is a change to a short wave length solution which also gives increasing growth rates. A smooth zone is seen due to wave lengths with stable or negative growth rates near the stagnation point. It is seen that, for cases with airfoil temperature colder than freezing, the maximum growth rate initially shows a long wave length solution near the stagnation line (discussed later in this section) and a shorter wavelength solution downstream of the stagnation line. This short wave length solution for the maximum growth is initially stable because of negative growth rate, and shows a sharp change to positive growth rate with increasing streamwise distance s, at distances similar to the typical width of the smooth zone seen in icing experiments (this is also discussed later in this section).

If the assumed temperature of the airfoil skin is kept constant, increasing ice height leads to decreasing heat flux within ice. Since the free-stream velocity as well as the free-stream temperature are constant, the cooling heat flux from the airflow is also constant.

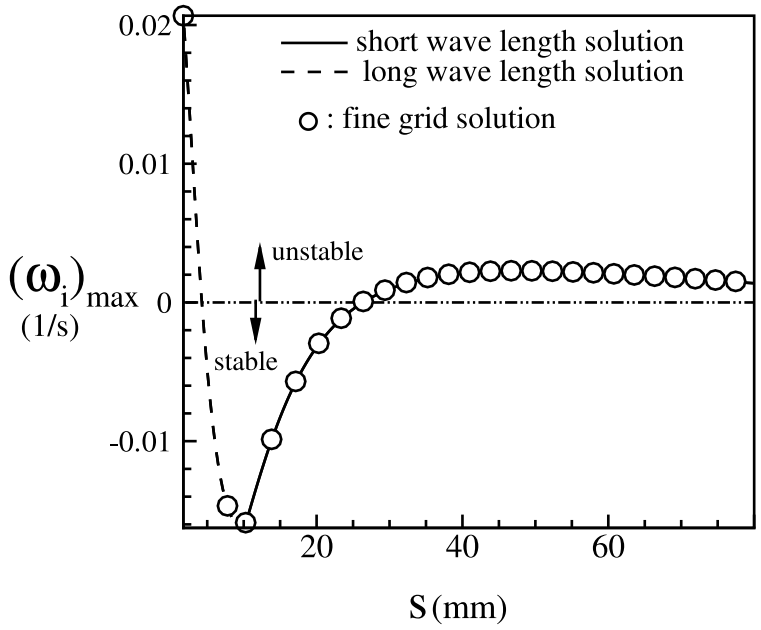

Figure 5.13 Grid independence for maximum growth rate with streamwise location for Run 2 of Table 5.1. The airfoil temperature is kept at 273 K and constant ice height over the airfoil surface is assumed.

This effect of the decreasing heat flux within ice with increasing accumulation parameter is seen in Fig. 5.14, where the airfoil skin is kept at a temperature 273 K. The influence of the airfoil temperature is shown in Fig. 5.15. As the temperature of the airfoil is decreased to 272 K, the ice surface becomes stable. When the temperature of the airfoil is kept at the freezing temperature of water, there is no influence of the heat flux from the airfoil and the ice surface becomes more unstable due to the cooling heat flux from the airflow.

There is a distinct change in the shape of the roughnesses for the maximum growth rate as s increases. In order to illustrate the typical pattern of the roughness sizes in the streamwise and spanwise directions, four streamwise locations (■ in Fig 5.14) are chosen. Here, the locations (a), (b) have negative growth rates while the locations (c) and (d) have positive growth rates. Fig. 5.18 shows that the spanwise wavelength for the maximum growth rate increases as s increases while the streamwise wavelength for the maximum growth rate remains almost constant. For these four locations, the change in the growth rate with varying wavelengths is seen in Figs. 5.17 and 5.16. The growth rates can show a range of unstable wave lengths in the spanwise direction, which is similar to behavior seen by Tsao and Rothmayer [41, 42, 43, 44] and Otta and Rothmayer [52] (see Fig. 5.16). A range of wavelengths for the streamwise and spanwise directions is obtained close to the maximum growth rate at each streamwise location, such that the growth rates corresponding to these wavelengths fall within 5 % of the maximum growth rate at that particular streamwise location. Fig. 5.19 shows that this range of wavelengths for the streamwise direction grows slightly, but stays almost constant along with the wavelength for the maximum growth rate. However, Fig. 5.19 shows that, for the spanwise direction, the wavelength corresponding to the maximum growth rate at each streamwise location grows along with the computed range of wavelengths near this maximum growth rate.

Both the roughness diameters as well as the width of the smooth zones are similar to

the values seen in experiments (Table 5.1). Using the results of Fig. 5.15, a comparison is made with the experimental values of the smooth zone in Fig. 5.21. The end of smooth zone is defined as the location of a sharp transition from negative to positive maximum growth rate for the short wave length solution discussed earlier. For the larger accumulation parameter in Fig. 5.21, the smooth zone is defined based on the change from the "long" wavelength to short wavelength for the maximum growth rate. A comparison is also made with the experimental values of the roughness diameters in Fig. 5.22. These roughness diameters are averages of the streamwise and spanwise diameters about 18-22 mm downstream of the stagnation line for each value of the accumulation parameter. These comparisons show that both the location of the smooth zone as well as the roughness diameters are very sensitive to the temperature of the airfoil skin. Airfoil temperatures much lower than freezing lead to the appeareance of smooth zones much farther away from the stagnation line. Colder airfoil surface also leads to longer roughness diameters which is seen in Fig. 5.22. The agreement for larger accumulation parameters is more difficult because the present model assumes a thin and smooth constant ice height everywhere over the airfoil surface and does not include any change in geometry of the ice shape seen in actual icing experiments. When the airfoil temperature is at freezing, the roughness diameters are smaller and the smooth zone is absent. Hence, in order to obtain correct estimates of the smooth zones along with roughness diameters for the early ice accretion times of these experiments, it is necessary to compute the transient ice accretion along with the local heat transfer inside the metal skin. Since a constant ice height is being assumed, this analysis does not account for the change in the ice shape with increasing time. It might also be necessary to include the curvature of the airfoil near the leading edge as well as non-parallel flow effects close to the stagnation line in the linear stability problem.

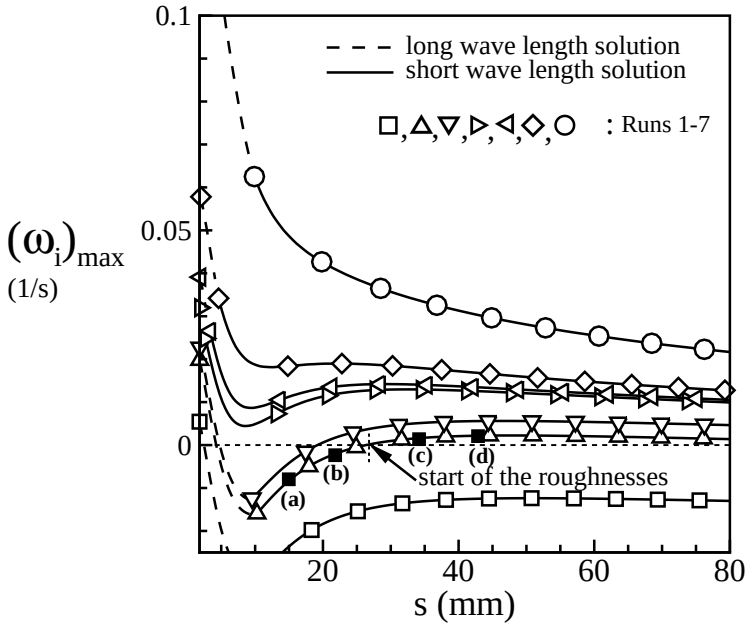

Figure 5.14 Typical maximum growth rate at different locations on the airfoil for the linear stability problem (see Table 5.1). Note the presence of a smooth zone in some of the calculations. The temperature of the airfoil is kept at 273 K.

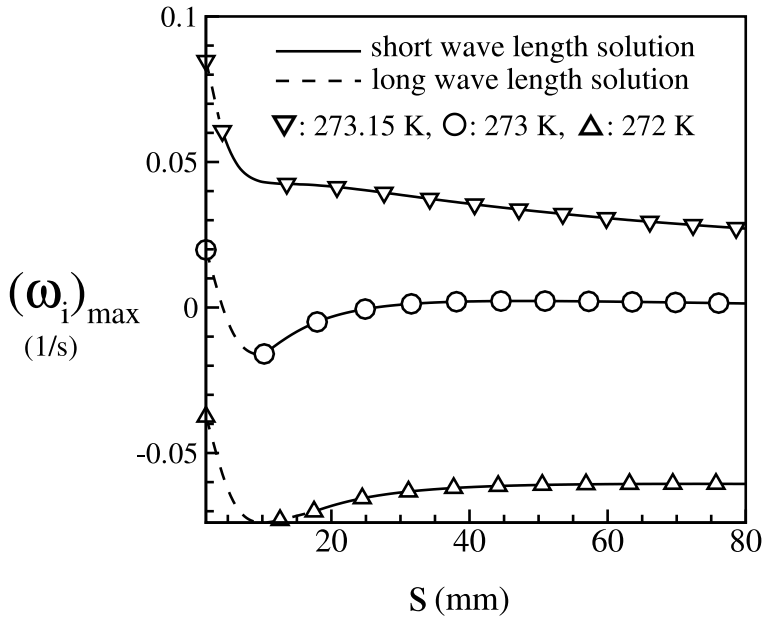

Figure 5.15 Increase in maximum growth rate with airfoil temperature closer to the freezing temperature of water for Run 2 of Table 5.1.

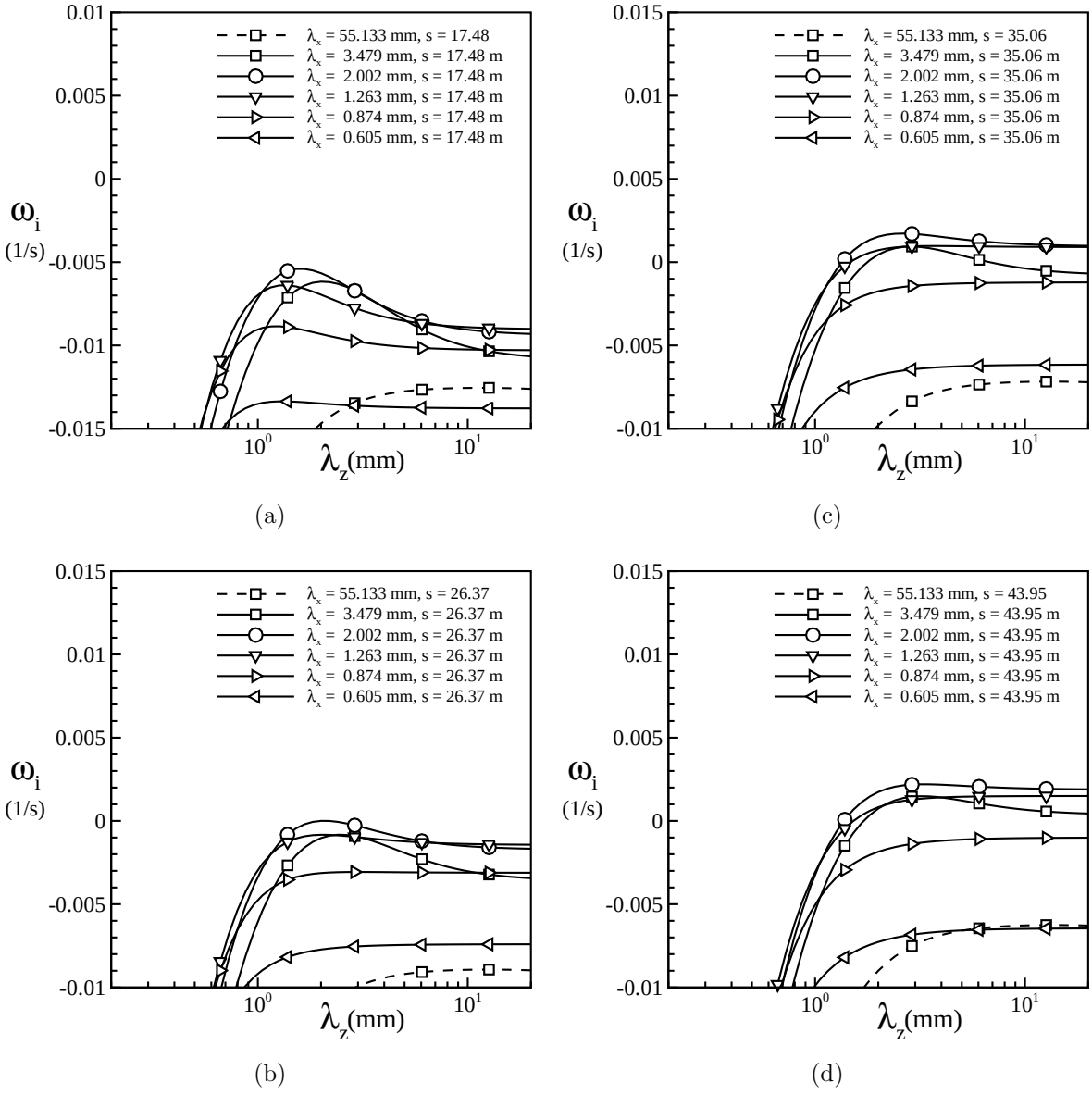

Figure 5.16 Change in growth rate with location for test Date : 5/30/96, C = 53.3 cm, Run 2, Series A: (a) s = 16.92 mm (b) s = 25.24 mm (c) s = 33.71 mm (d) s = 42.25 mm, (■ in Fig. 5.14).

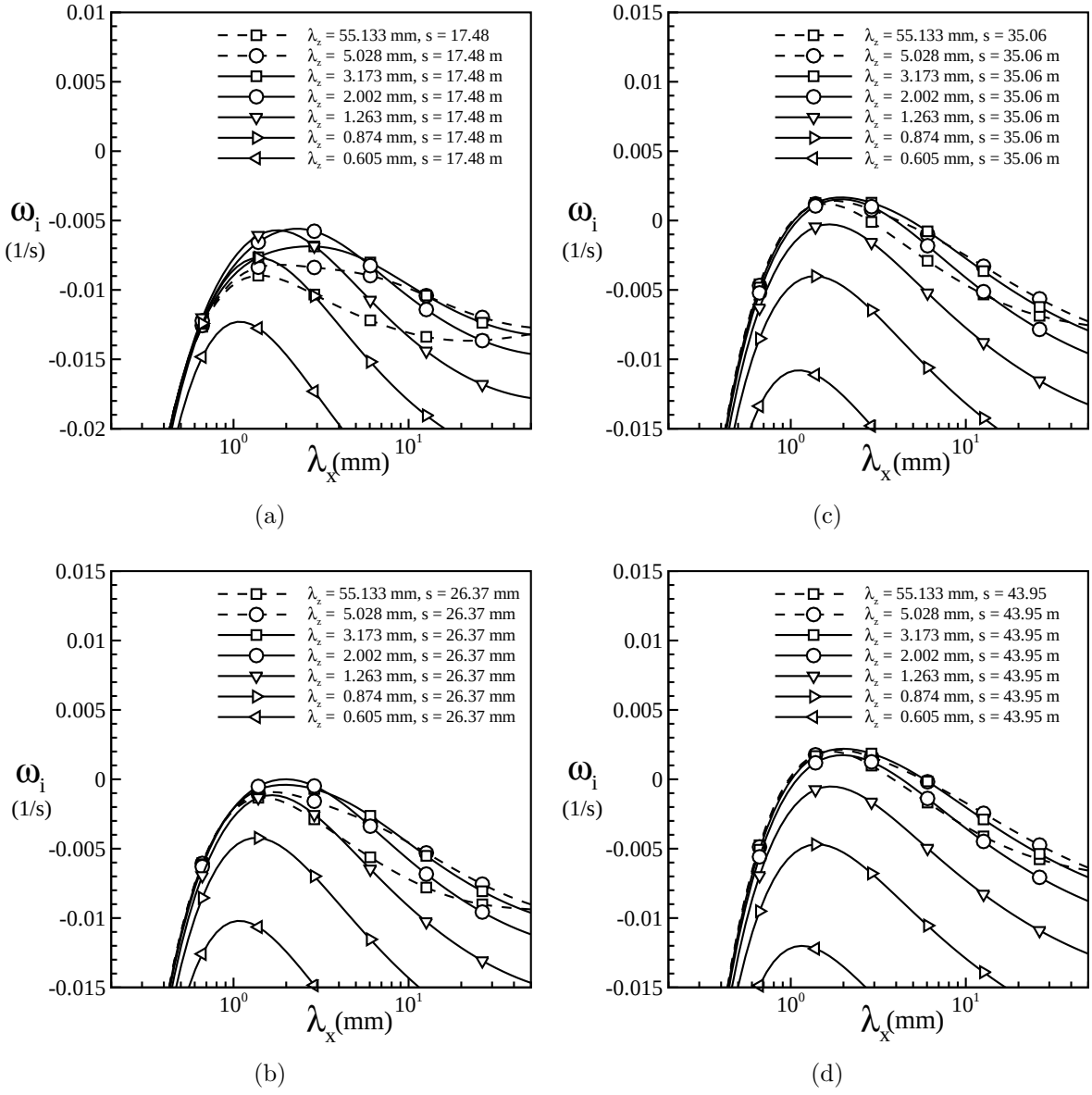

Figure 5.17 Change in growth rate with location for test Date : 5/30/96, C = 53.3 cm, Run 2, Series A: (a) s = 16.92 mm (b) s = 25.24 mm (c) s = 33.71 mm (d) s = 42.25 mm, (■ in Fig. 5.14).

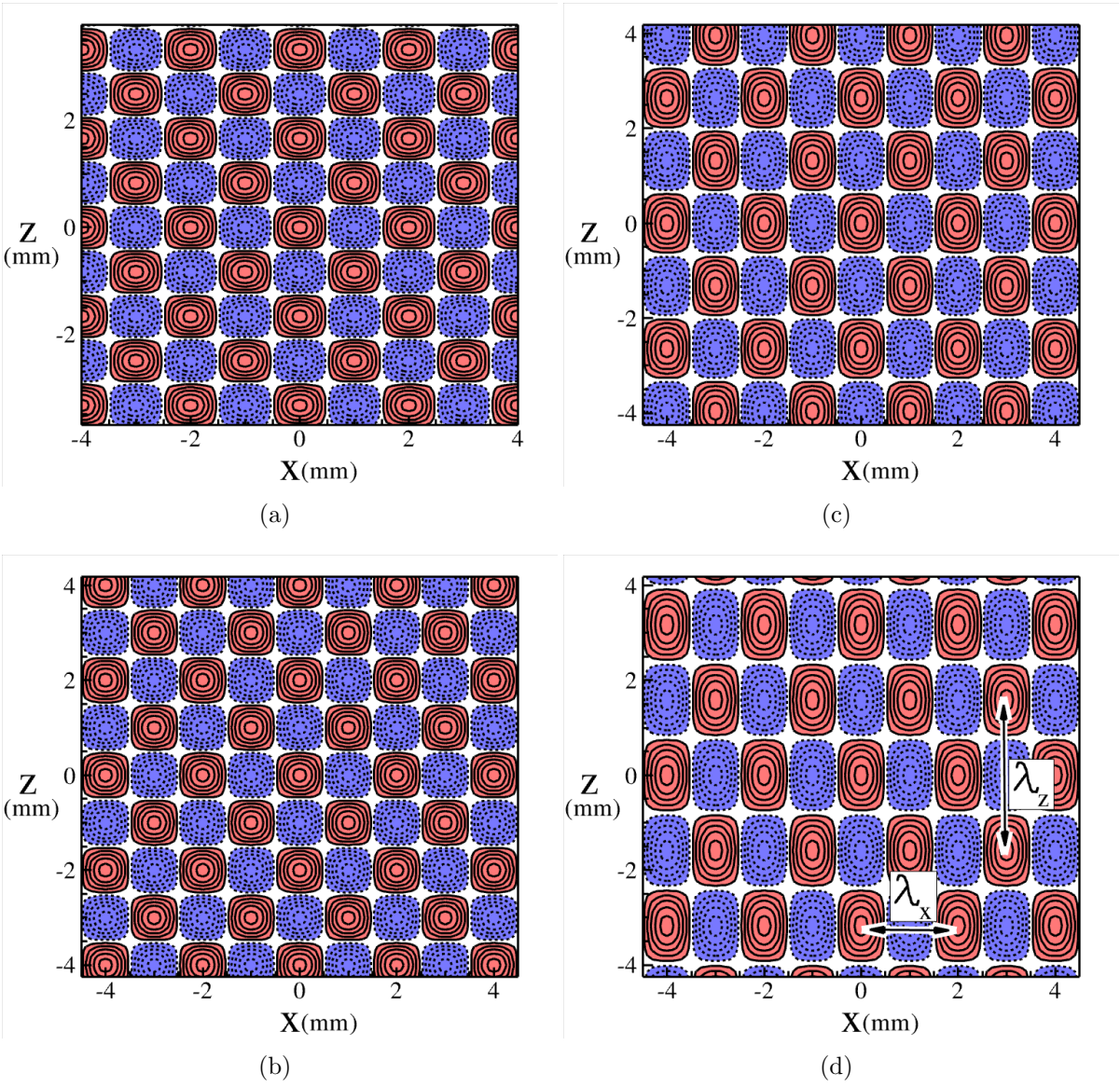

Figure 5.18 Change in roughness pattern at maximum growth rate with location for test Date : 5/30/96, C = 53.3 cm, Run 2, Series A: (a) s = 16.92 mm (b) s = 25.24 mm (c) s = 33.71 mm (d) s = 42.25 mm. Also shown are the typical streamwise and spanwise wavelengths λ_x, λ_z respectively, (■ in Fig. 5.14).

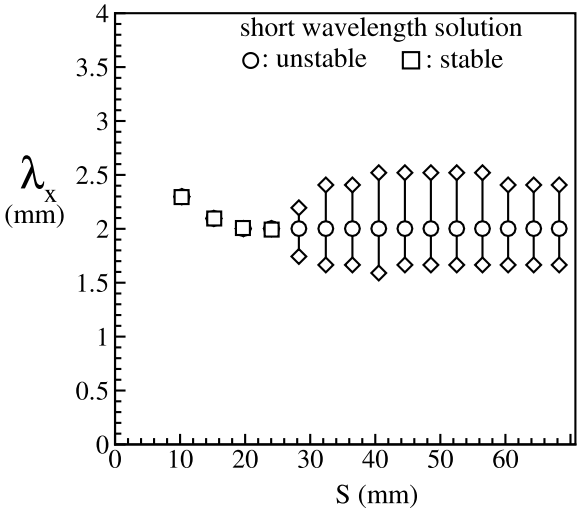

Figure 5.19 Variation of roughness diameters at the maximum growth rate with streamwise location. The bars $\diamond - \diamond$ are diameters with growth rates which are within 5 % of the maximum growth rate (see Fig. 5.17 for typical range of wave numbers around maximum growth rate).

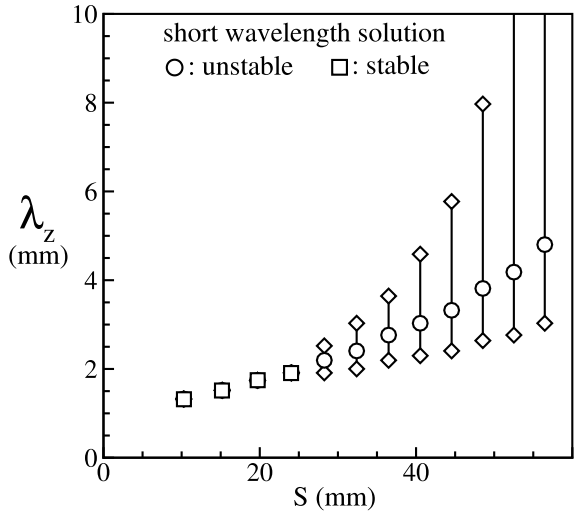

Figure 5.20 Variation of roughness diameters at the maximum growth rate with streamwise location. The bars $\diamond - \diamond$ are diameters with growth rates which are within 5 % of the maximum growth rate (see Fig. 5.16 for typical range of wave numbers around maximum growth rate).

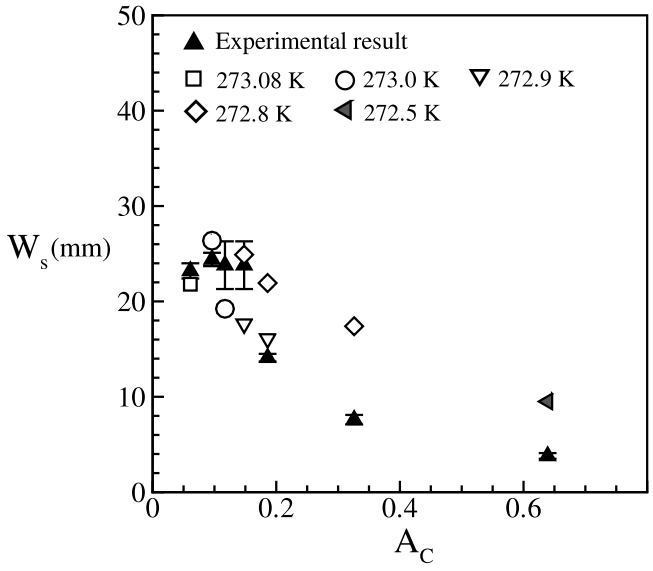

Figure 5.21 Comparison of the width of the smooth zones with predictions from the linear stability calculations. The open symbols represent a sharp transition from negative to positive maximum growth rate with s ($A_c < 0.4$) and the gray symbol for $A_c = 0.639$ identifies the smooth zone based on the change from long wave length to short wavelength solution.

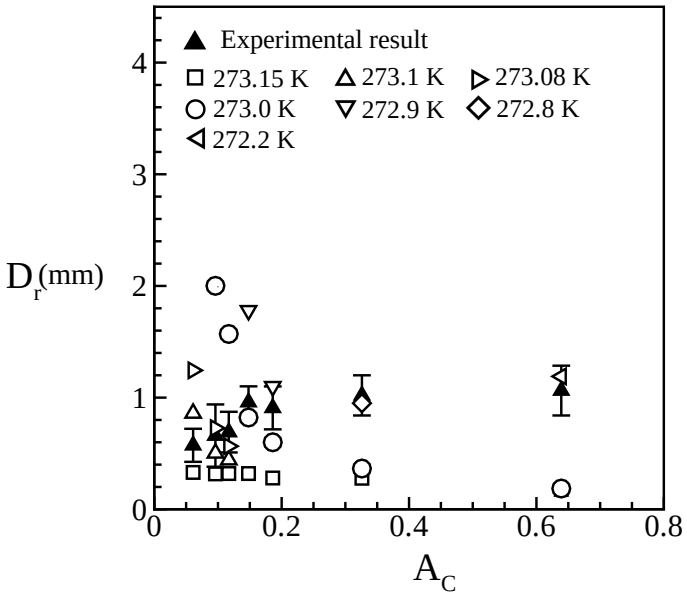

Figure 5.22 Comparison of the roughness diameters with predictions from the linear stability calculations.

CHAPTER 6. CONCLUSION

The stability of ice surfaces is examined near the stagnation line of swept and unswept wings for conditions of in-flight icing. A high Reynolds number model of roughness formation is developed, where the roughness dimensions are on the scale of the air boundary layer thickness. The low Mach number high Reynolds number formulation for the airflow is incompressible at leading order and includes the bulk effect of Mach number heating in the Hiemenz solution. The thin water film covering the ice is found to be passively conducting. Using a Hiemenz solution in the airflow and linearized perturbation equations in the air and ice, growth rates are obtained for ice surfaces. The ice surface near the stagnation line is found to be unstable in situations of aerodynamic cooling. The ice surface instability exhibits a strong dependence on the heat flux from the airflow, which suppresses the instability at larger Mach numbers. The instability is also seen to be primarily three-dimensional at lower Mach numbers.

Swept wing stagnation line computations reveal that the sweep angle and the resulting flow along the attachment line have a strong influence on the shape of the roughnesses, their orientation and the growth rates associated with these roughnesses. As the sweep angle increases, the roughnesses show a change in orientation, where the roughness pattern at maximum growth rate takes the form of elongated ridges which are aligned approximately perpendicular to the airflow limiting surface streamlines. The increase in sweep angle also makes the ice surface more unstable than an unswept stagnation line flow. These results are consistent with observations from icing experiments.

A preliminary non-asymptotic linearized stability analysis based on the stagnation

line analysis is also developed for studying the stability of ice surfaces on a parabolic leading edge with spacially varying heat flux under conditions of glaze icing. It is seen that the growth rates for the ice surface instability on thin ice sheets are very sensitive to the temperature of the airfoil skin and the ice thickness. The spanwise wavelengths are usually larger than the streamwise wavelengths for the maximum growth rate for each location on the airfoil. The wavelengths of these roughnesses are consistent with roughness sizes observed in experiments, providing that the airfoil skin temperature is selected correctly and very close to freezing. Sharply defined smooth zones are also observed in some of the stability calculations when the airfoil skin temperature is close to freezing. However, a general lack of detailed agreement with the experiments suggest that other effects, such as a much more detailed model of the heat conduction within the airfoil skin should be included in future simulations.

APPENDIX A. NUMERICAL SCHEME FOR THE STAGNATION / ATTACHMENT LINE ICING PROBLEM

For the stagnation icing problem, the momentum equations for the perturbation variables (see Chapter 3) are found to be

$$\begin{aligned}
&\xi f'(\eta)\bar{U}_\xi + \bar{U} f'(\eta) - f(\eta)\bar{U}_\eta + \bar{V}\xi f''(\eta) \\
&\qquad + i\bar{\beta} g(\eta)\bar{U} &= -\bar{P}_\xi + \bar{U}_{\xi\xi} + \bar{U}_{\eta\eta} - \bar{\beta}^2\bar{U}, &\text{(A.1)}\\
&\xi f'(\eta)\bar{V}_\xi - f(\eta)\bar{V}_\eta - \bar{V} f'(\eta) + i\bar{\beta} g(\eta)\bar{V} &= -\bar{P}_\eta + \bar{V}_{\xi\xi} + \bar{V}_{\eta\eta} - \bar{\beta}^2\bar{V}, &\text{(A.2)}\\
&\xi f'(\eta)\bar{W}_\xi - f(\eta)\bar{W}_\eta + \bar{V} g'(\eta) + i\bar{\beta} g(\eta)\bar{W} &= -i\bar{\beta}\bar{P} + \bar{W}_{\xi\xi} + \bar{W}_{\eta\eta} - \bar{\beta}^2\bar{W}, &\text{(A.3)}\\
&\xi f'(\eta)\bar{T}_\xi - f(\eta)\bar{T}_\eta + \bar{V} T'_H + i\bar{\beta} g(\eta)\bar{T} &= \frac{1}{\mathrm{Pr}}\left[\bar{T}_{\xi\xi} + \bar{T}_{\eta\eta} - \bar{\beta}^2\bar{T}\right]. &\text{(A.4)}
\end{aligned}$$

The continuity equation is given by

$$i\beta\bar{W} = -\left[\frac{\partial\bar{U}}{\partial\xi} + \frac{\partial\bar{V}}{\partial\eta}\right]. \tag{A.5}$$

Using Eqs. A.1, A.2, A.3 and A.5, the Poisson equation for pressure is given by

$$-2f'(\eta)\bar{U}_\xi - 2\xi f''(\eta)\bar{V}_\xi + 2f'(\eta)\bar{V}_\eta - i2\bar{\beta} g'(\eta)\bar{V} = \bar{P}_{\xi\xi} + \bar{P}_{\eta\eta} - \bar{\beta}^2\bar{P}. \tag{A.6}$$

The boundary conditions for the perturbation variables at the ice surface are

$$\bar{U}(\xi,0) = -\xi f''(\eta)\,\bar{F}_{ice}, \qquad \bar{V}(\xi,0) = f'(\eta)\,\bar{F}_{ice} = 0,$$
$$\bar{W}(\xi,0) = -g'(\eta)\,\bar{F}_{ice}, \qquad \bar{T}(\xi,0) = -T'_H(\eta)\,\bar{F}_{ice}.$$

To obtain a boundary condition for pressure, the y-momentum equation (Eq. A.2) is evaluated at the ice surface which becomes

$$0 = -\frac{\partial \bar{P}}{\partial \eta} + \frac{\partial^2 \bar{V}}{\partial \eta^2}. \tag{A.7}$$

The continuity equation at the ice surface is rewritten as

$$-i\bar{\beta} g'(\eta)\,\bar{F}_{ice} = -\left[\frac{\partial \bar{U}}{\partial \xi} + \frac{\partial \bar{V}}{\partial \eta}\right]. \tag{A.8}$$

This is incorporated in the pressure equation at the ice surface, as illustrated later in this section. Including grid stretching, the governing equations for the perturbation variables are found to be

$$\begin{aligned} &\xi f'(\eta)\frac{1}{\xi_{\xi'}}\frac{\partial \bar{U}}{\partial \xi'} + \bar{U} f'(\eta) - f(\eta)\frac{1}{\eta_{\eta'}}\frac{\partial \bar{U}}{\partial \eta'} + \xi f''(\eta)\,\bar{V} + i\bar{\beta} g(\eta)\bar{U} \\ &= -\frac{1}{\xi_{\xi'}}\frac{\partial \bar{P}}{\partial \xi'} + \frac{1}{\xi_{\xi'}}\frac{\partial}{\partial \xi'}\left(\frac{1}{\xi_{\xi'}}\frac{\partial \bar{U}}{\partial \xi'}\right) + \frac{1}{\eta_{\eta'}}\frac{\partial}{\partial \eta'}\left(\frac{1}{\eta_{\eta'}}\frac{\partial \bar{U}}{\partial \eta'}\right) - \bar{\beta}^2 \bar{U}, \end{aligned} \tag{A.9}$$

$$\begin{aligned} &\xi f'(\eta)\frac{1}{\xi_{\xi'}}\frac{\partial \bar{V}}{\partial \xi'} - f(\eta)\frac{1}{\eta_{\eta'}}\frac{\partial \bar{V}}{\partial \eta'} - f'(\eta)\,\bar{V} + i\bar{\beta} g(\eta)\bar{V} \\ &= -\frac{1}{\eta_{\eta'}}\frac{\partial \bar{P}}{\partial \eta'} + \frac{1}{\xi_{\xi'}}\frac{\partial}{\partial \xi'}\left(\frac{1}{\xi_{\xi'}}\frac{\partial \bar{V}}{\partial \xi'}\right) + \frac{1}{\eta_{\eta'}}\frac{\partial}{\partial \eta'}\left(\frac{1}{\eta_{\eta'}}\frac{\partial \bar{V}}{\partial \eta'}\right) - \bar{\beta}^2 \bar{V}, \end{aligned} \tag{A.10}$$

$$-2f'(\eta)\left[\frac{1}{\xi_{\xi'}}\frac{\partial\bar{U}}{\partial\xi'}-\frac{1}{\eta_{\eta'}}\frac{\partial\bar{V}}{\partial\eta'}\right]-2\xi f''(\eta)\frac{1}{\xi_{\xi'}}\frac{\partial\bar{V}}{\partial\xi'}= \frac{1}{\xi_{\xi'}}\frac{\partial}{\partial\xi'}\left(\frac{1}{\xi_{\xi'}}\frac{\partial\bar{P}}{\partial\xi'}\right)+\frac{1}{\eta_{\eta'}}\frac{\partial}{\partial\eta'}\left(\frac{1}{\eta_{\eta'}}\frac{\partial\bar{P}}{\partial\eta'}\right)-\bar{\beta}^2\bar{P}, \tag{A.11}$$

and

$$\xi f'(\eta)\frac{1}{\xi_{\xi'}}\frac{\partial\bar{T}}{\partial\xi'}-f(\eta)\frac{1}{\eta_{\eta'}}\frac{\partial\bar{T}}{\partial\eta'}+\bar{V}T'_H+i\bar{\beta}g(\eta)\bar{T}= \frac{1}{\mathrm{Pr}}\left[\frac{1}{\xi_{\xi'}}\frac{\partial}{\partial\xi'}\left(\frac{1}{\xi_{\xi'}}\frac{\partial\bar{T}}{\partial\xi'}\right)+\frac{1}{\eta_{\eta'}}\frac{\partial}{\partial\eta'}\left(\frac{1}{\eta_{\eta'}}\frac{\partial\bar{T}}{\partial\eta'}\right)-\bar{\beta}^2\bar{T}\right]. \tag{A.12}$$

To implement grid stretching, the coordinates (ξ,η) are transformed to (ξ',η'), which is a coordinate system with uniform grid stretching. Using the transformations $[\xi(\xi'),\eta(\eta')]$, the second derivative for $\bar{U}$ is written as

$$\frac{1}{\eta_{\eta'}}\frac{\partial}{\partial\eta'}\left(\frac{1}{\eta_{\eta'}}\frac{\partial\bar{U}}{\partial\eta'}\right)=\frac{1}{\eta_{\eta' i,j}}\frac{1}{\Delta\eta'}\left(\frac{1}{\eta_{\eta' i,j+1/2}}\frac{\partial\bar{U}}{\partial\eta'}-\frac{1}{\eta_{\eta' i,j-1/2}}\frac{\partial\bar{U}}{\partial\eta'}\right) \frac{1}{\eta_{\eta' i,j}}\frac{1}{\Delta\eta'^2}\left(\frac{2}{\eta_{\eta' i,j+1}+\eta_{\eta' i,j}}\left(\bar{U}_{i,j+1}-\bar{U}_{i,j}\right)-\frac{2}{\eta_{\eta' i,j}+\eta_{\eta' i,j-1}}\left(\bar{U}_{i,j}-\bar{U}_{i,j-1}\right)\right).$$

Collecting terms and rewriting, the expression for $\bar{U}_{\eta\eta}$ is

$$\frac{1}{\eta_{\eta'}}\frac{\partial}{\partial\eta'}\left(\frac{1}{\eta_{\eta'}}\frac{\partial\bar{U}}{\partial\eta'}\right) = \frac{1}{\eta_{\eta' i,j}}\frac{1}{\Delta\eta'^2}\left[J_3\bar{U}_{i,j+1}-2J_2\bar{U}_{i,j}+J_1\bar{U}_{i,j-1}\right],$$

where $J_3=\frac{2}{\eta_{\eta' i,j+1}+\eta_{\eta' i,j}}$, $J_2=\left(\frac{1}{\eta_{\eta' i,j+1}+\eta_{\eta' i,j}}+\frac{1}{\eta_{\eta' i,j}+\eta_{\eta' i,j-1}}\right)$, $J_1=\frac{2}{\eta_{\eta' i,j}+\eta_{\eta' i,j-1}}$. Similarly the expression for $\bar{U}_\eta$ is

$$\frac{1}{\eta_{\eta'}}\frac{\partial\bar{U}}{\partial\eta'} = \frac{1}{\eta_{\eta',i,j}}\frac{1}{2\Delta\eta'}\left(\bar{U}_{i,j+1}-\bar{U}_{i,j-1}\right).$$

The expression for $\bar{U}_{\xi\xi}$ is

$$\frac{1}{\xi_{\xi'}}\frac{\partial}{\partial\xi'}\left(\frac{1}{\xi_{\xi'}}\frac{\partial\bar{U}}{\partial\xi'}\right) = \frac{1}{\xi_{\xi',i,j}}\frac{1}{\Delta\xi'^2}\left[K_3\bar{U}_{i+1,j} - 2K_2\bar{U}_{i,j} + K_1\bar{U}_{i-1,j}\right],$$

where $K_3 = \frac{2}{\xi_{\xi',i+1,j}+\xi_{\xi',i,j}}$, $K_2 = \left(\frac{1}{\xi_{\xi',i+1,j}+\xi_{\xi',i,j}} + \frac{1}{\xi_{\xi',i,j}+\xi_{\xi',i-1,j}}\right)$, $K_1 = \frac{2}{\xi_{\xi',i,j}+\xi_{\xi',i-1,j}}$. A higher order finite difference expression is chosen for terms in the equations with a coefficient of ξ such that second order accurary is preserved with the chosen domain. This also implies that the domain size is limited by the largest ξ and its influence on the finite difference scheme. Using the fourth order central difference scheme, the expression for $\bar{U}_{\xi}$ is

$$\frac{1}{\xi_{\xi'}}\frac{\partial\bar{U}}{\partial\xi'} = \frac{1}{\xi_{\xi',i,j}}\frac{1}{12\Delta\xi'}\left(\bar{U}_{i+2,j} - 8\bar{U}_{i+1,j} + 8\bar{U}_{i-1,j} - \bar{U}_{i-2,j}\right).$$

Using a 3rd order differentiation for η and second order differentiation for ξ for Eq. A.8, the finite difference expression is

$$\begin{aligned}\frac{1}{\xi_{\xi',i}}\frac{1}{12\Delta\xi'}&\left(\bar{U}_{i+2,1} - 8\bar{U}_{i+1,1} + 8\bar{U}_{i-1,1} - \bar{U}_{i-2,1}\right)\\ &+\frac{1}{\eta_{\eta',j}}\frac{-2\bar{V}_{i,0} - 3\bar{V}_{i,1} + 6\bar{V}_{i,2} - \bar{V}_{i,3}}{6\Delta\eta'} = i\bar{\beta}g'(\eta)\,\bar{F}_{ice}.\end{aligned}$$

Using $\bar{V}_{i,1} = 0$, this expression reduces to

$$\frac{1}{\xi_{\xi',i}}\frac{3\left(\bar{U}_{i+1,1} - \bar{U}_{i+1,1}\right)}{2\Delta\xi'\Delta\eta'} + \frac{1}{\eta_{\eta',j}}\frac{-\bar{V}_{i,0} + 3\bar{V}_{i,2} - \frac{1}{2}\bar{V}_{i,3}}{\Delta\eta'^2} = \frac{3}{\Delta\eta'}i\bar{\beta}g'(\eta)\,\bar{F}_{ice}. \quad \text{(A.13)}$$

With grid stretching, the pressure boundary condition (Eq. A.7) is rewriten as

$$-\frac{1}{\eta_{\eta'}}\frac{\partial\bar{P}}{\partial\eta} + \frac{1}{\eta_{\eta'}}\frac{\partial}{\partial\eta}\left(\frac{1}{\eta_{\eta'}}\frac{\partial\bar{V}}{\partial\eta}\right) = 0.$$

The finite difference expression for this equation is obtained as

$$-\frac{1}{\eta_{\eta',j}}\frac{-3\bar{P}_{i,1}+4\bar{P}_{i,2}-\bar{P}^{g}_{i,3}}{2\Delta\eta'}+\frac{1}{\eta_{\eta' i,j}}\frac{1}{\Delta\eta'^{2}}\left[J_3\bar{V}_{i,2}-2J_2\bar{V}_{i,1}+J_1\bar{V}_{i,0}\right]=0. \tag{A.14}$$

In this equation, $\bar{V}_{i,1}=0$. Hence

$$-\frac{1}{\eta_{\eta',j}}\frac{-3\bar{P}_{i,1}+4\bar{P}_{i,2}-\bar{P}^{g}_{i,3}}{2\Delta\eta'}+\frac{1}{\eta_{\eta' i,j}}\frac{1}{\Delta\eta'^{2}}\left[J_3\bar{V}_{i,2}+J_1\bar{V}_{i,0}\right]=0. \tag{A.15}$$

Combining Eqs. A.13 and A.15,

$$\begin{aligned}-\frac{1}{\eta_{\eta',j}}\frac{-3\bar{P}_{i,1}+4\bar{P}_{i,2}-\bar{P}_{i,3}}{2\Delta\eta'}+\frac{1}{\eta_{\eta' i,j}}\frac{1}{\Delta\eta'^{2}}\left[J_3\bar{V}_{i,2}+J_1\bar{V}_{i,0}\right]+\\ \frac{1}{\xi_{\xi',i}}\frac{3J_1\left(\bar{U}_{i+2,j}-8\bar{U}_{i+1,j}+8\bar{U}_{i-1,j}-\bar{U}_{i-2,j}\right)}{12\Delta\xi'\Delta\eta'}+\frac{J_1}{\eta_{\eta',j}}\frac{-\bar{V}_{i,0}+3\bar{V}_{i,2}-\frac{1}{2}\bar{V}_{i,3}}{\Delta\eta'^{2}}\\ =\frac{3J_1}{\Delta\eta'}i\bar{\beta}g'\left(\eta\right)\bar{F}_{ice}.\end{aligned}$$

Rewriting, the pressure boundary condition becomes

$$\begin{aligned}-\frac{1}{\eta_{\eta',j}}\frac{-3\bar{P}_{i,1}+4\bar{P}_{i,2}}{2\Delta\eta'}+\frac{1}{\eta_{\eta',j}}\frac{[J_3+3J_1]}{\Delta\eta'^{2}}\bar{V}_{i,2}=\frac{1}{\eta_{\eta',j}}\frac{-\bar{P}^{g}_{i,3}}{2\Delta\eta'}+\frac{J_1}{\eta_{\eta',j}}\frac{\frac{1}{2}\bar{V}^{g}_{i,3}}{\Delta\eta'^{2}}\\ -\frac{1}{\xi_{\xi',i}}\frac{3J_1\left(\bar{U}^{g}_{i+2,j}-8\bar{U}^{g}_{i+1,j}+8\bar{U}^{g}_{i-1,j}-\bar{U}^{g}_{i-2,j}\right)}{12\Delta\xi'\Delta\eta'}+\frac{3J_1}{\Delta\eta'}i\bar{\beta}g'\left(\eta\right)\bar{F}_{ice}.\end{aligned}$$

Stretching in ξ is given by

$$\xi(\xi')=\tanh^{-1}(a_4\xi')*\exp(a_3\left|\xi'\right|)*\frac{\left|\xi'_{max}-\xi_C\right|}{k_{max}}+\xi'_C.$$

ξ_C is at the attachment line, i.e. $\xi_C=0$. The Jacobian for ξ is given by

$$\xi_{\xi'}(\xi')=\left[\frac{a_4}{1-a_4^2\xi'^2}+a_3\tanh^{-1}(a_4\xi')\right]\exp(a_3\left|\xi'\right|)\frac{\left|\xi'_{max}-\xi'_C\right|}{k_{max}},\qquad \xi'>0.$$

$$\xi_{\xi'}(\xi')=\left[\frac{a_4}{1-a_4^2\xi'^2}-a_3\tanh^{-1}(a_4\xi')\right]\exp(a_3\left|\xi'\right|)\frac{\left|\xi'_{max}-\xi'_C\right|}{k_{max}},\qquad \xi'<0.$$

APPENDIX B. ALTERNATE BOUNDARY LAYER FORMULATION

Another formulation for the boundary layer equations in Section 5.2 may be obtained, where the streamwise and vertical velocities within the boundary layer are expressed using a stream function given by

$$\Psi = \sqrt{2\xi} f(\xi, \eta).$$

For a stream function formulation with $U = \Psi_N$, $V = -\Psi_s$, the momentum equation for the streamwise direction is found to be

$$\Psi_N \Psi_{sN} - \Psi_s \Psi_{NN} = U_e U_{es} + \Psi_{NNN},$$

where s is the stream-wise coordinate and N is the coordinate normal to the surface. Using the definition for the stream function, this momentum equation then reduces to

$$f_{\eta\eta\eta} + f f_{\eta\eta} + \beta(1 - f_\eta^2) = 2\xi(f_\eta f_{\eta\xi} - f_\xi f_{\eta\eta}).$$

Similarly, using $W = W_e h(\xi, \eta)$, the spanwise momentum equation reduces to

$$h_{\eta\eta} + f h_\eta = 2\xi(f_\eta h_\xi - f_\xi h_\eta).$$

Again using the Görtler variables , the energy equation is simplified to

$$\frac{1}{\mathrm{Pr}_{air}}\hat{T}_{\eta\eta} + f\hat{T}_{\eta} = 2\xi(f_{\eta}\hat{T}_{\xi} - f_{\xi}\hat{T}_{\eta}) - \left(-2\xi f_{\eta}(\gamma-1)m_{\infty}^{2}U_{es}\right) \\ -(\gamma-1)m_{\infty}^{2}\left(U_{e}^{2}\left(f_{\eta\eta}\right)^{2} + \left(W_{\eta}\right)^{2}\right).$$

Then a temperature split is used given by $\hat{T} = \pm[e(\xi,\eta)-1]+\frac{\gamma-1}{2}m_{\infty}^{2}[e(\xi,\eta)-U_{e}^{2}g(\xi,\eta)-W_{e}^{2}k(\xi,\eta)]$. The three energy equations are then given by

$$\begin{aligned} \frac{1}{\mathrm{Pr}}e_{\eta\eta} + fe_{\eta} &= 2\xi(f_{\eta}e_{\xi} - f_{\xi}e_{\eta}), \\ \frac{1}{\mathrm{Pr}}g_{\eta\eta} + fg_{\eta} - 2\beta f_{\eta}g &= 2\xi(f_{\eta}g_{\xi} - f_{\xi}g_{\eta}) + 2\left(f_{\eta\eta}^{2} - \beta f_{\eta}\right), \\ \frac{1}{\mathrm{Pr}}k_{\eta\eta} + fk_{\eta} &= 2\xi(f_{\eta}k_{\xi} - f_{\xi}k_{\eta}) + 2h_{\eta}^{2}. \end{aligned}$$

The boundary conditions at the wall are given by $f(0) = f'(0) = 0, h(0) = 0, e(0) = 0, g(0) = 0, k(0) = 0$ and the boundary conditions at the edge of the boundary layer are $f'(\infty) = 1, h(\infty) = 1, e(\infty) = 1, g(\infty) = 1, k(\infty) = 1$.

APPENDIX C. EQUATIONS FOR INTERFACE BOUNDARIES

A generic single-valued surface evolving with time may be defined by

$$x_2^* = f^*(x_2^*(t^*), x_3^*(t^*), t^*).$$

In order to obtain an equation for the evolution of the surface, the equation depicting the surface is differentiated with respect to time using chain rule, which gives

$$\frac{\partial x_2^*}{\partial t^*} = \frac{\partial x_1^*}{\partial t^*}\frac{\partial f^*}{\partial x_1^*} + \frac{\partial x_3^*}{\partial t^*}\frac{\partial f^*}{\partial x_3^*} + \frac{\partial f^*}{\partial t^*}.$$

The velocities on this surface are given by

$$(u_1^*, u_2^*, u_3^*) = \frac{\partial}{\partial t^*}(x_1^*, x_2^*, x_3^*).$$

This is used to obtain the kinematic condition which is

$$u_2^* = u_1^*\frac{\partial f^*}{\partial x_1^*} + u_3^*\frac{\partial f^*}{\partial x_3^*} + \frac{\partial f^*}{\partial t^*}.$$

For this generic single-valued surface, the surface normals directed outward are given by

$$\hat{n} = \frac{\nabla(x_2^* - f)}{|\nabla(x_2^* - f)|}.$$

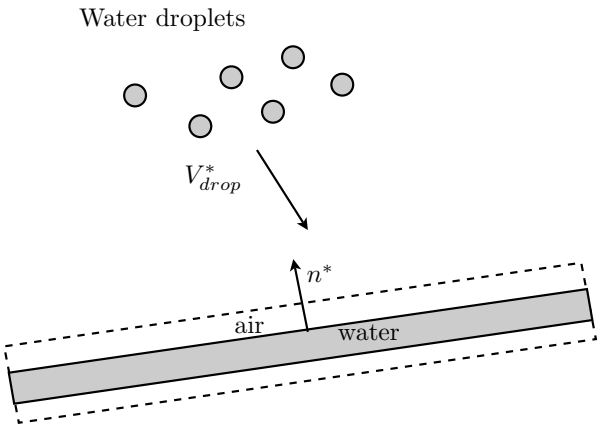

Figure C.1 Mass accumulation due to uniform deposition of droplets.

For obtaining the effect of mass accumulation due to droplet impacts, droplets are assumed to impact the surface with a constant liquid water content LWC^* as seen in Fig C.1. Then, considering the control volume in Fig C.1, the mass accumulated on the surface is

$$\frac{dm^*}{dt^*} = LWC^* V^*_{i,drop} n^*_i dS.$$

This implies that the increment in the water film surface is proportional to this mass accumulation which gives

$$\rho^*_{surface} d\delta^*_{surface} dS = -dm = -LWC^* V^*_{i,drop} n^*_i dS dt^*.$$

Then, the rate of growth of the water film is obtained as

$$\rho^*_{water} \frac{d\delta^*_{water}}{dt^*} = -LWC^* V^*_{i,drop} n^*_i.$$

The liquid water content LWC^* is the local liquid water content over the surface. It is assumed that the airflow does not change the droplet trajectories close to the surface. Simplifying the equation and using the expression for the surface normals, the increment

in the water film is found to be

$$\frac{d\delta^*_{water}}{dt^*} = \frac{LWC^*}{\rho^*_{water}}\left[v^*_{1,d}\frac{\partial f^*_{water}}{\partial x^*_1} + v^*_{3,d}\frac{\partial f^*_{water}}{\partial x^*_3} + \left|v^*_{2,d}\right|\right]\left[\left(\frac{\partial f^*_{water}}{\partial x^*_1}\right)^2 + 1 + \left(\frac{\partial f^*_{water}}{\partial x^*_3}\right)^2\right]^{-1/2}.$$

The kinematic condition becomes

$$u^*_{2,air} = u^*_{1,air}\frac{\partial f^*_{water}}{\partial x^*_1} + u^*_{3,air}\frac{\partial f^*_{water}}{\partial x^*_3} + \frac{\partial f^*_{water}}{\partial t^*}.$$

If a velocity match is considered at the air/water interface, the rate of increase of the water film height affects the velocities within the water film. This gives the velocities within water as

$$v^*_{i,water} = v^*_{i,air} - \frac{d\delta^*_{water}}{dt^*}n^*_i.$$

All these conditions are combined to evaluate the changes in the water film surface. If a control volume like the one shown in Fig. C.2 is considered, then the total energy including the energy added due to the supercooled water impact layer and the heat transfer to the airflow and the water is conserved. This gives

$$\frac{\partial}{\partial t^*}\iiint (\rho c)^*_{water}\Delta T dV + \iint \mathbf{q}\bullet\hat{\mathbf{n}}dS = 0.$$

Using Fourier law of conduction, the surface normal definitions for the water film and the increment in the water film for the added mass, the heat flux balance at the air/water interface becomes

$$k^*_{air}\left[\frac{\partial T^*}{\partial x^*_j}\right]_{air} n^*_j = k^*_{water}\left[\frac{\partial T^*}{\partial x^*_j}\right]_{water} n^*_j + (\rho c)^*_{water}\left[T^*_{water} - T^*_{impact}\right]\frac{d\delta^*_{water}}{dt},$$

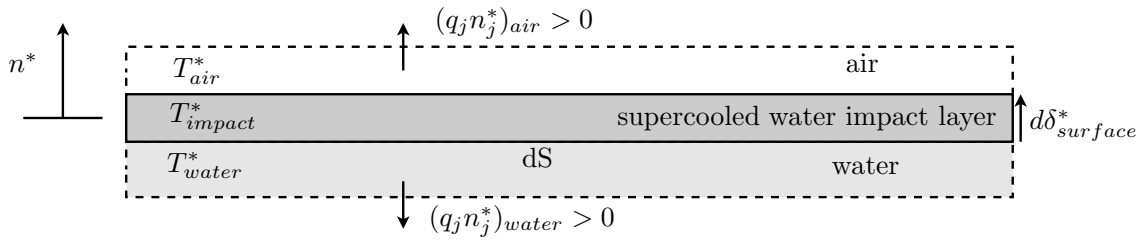

Figure C.2 Temperature change with uniform deposition of droplets.

It is assumed that the added water is being added uniformly and comes immediately to a thermal equilibrium.

The movement of the ice surface imposes an injection velocity inside water. This condition needs to consider the density changes associated with the phase change of water to ice and the resulting change in volume to expansion. Then, injection velocity felt by water due to movement of the ice surface is given by

$$v^*_{i,ice} = \frac{\rho^*_{water}}{\rho^*_{ice}} \frac{d\delta^*_{ice}}{dt^*} n^*_i.$$

Here the surface normals are defined using the single-valued ice surface f^*_{ice}. The kinematic condition for the ice surface is

$$u^*_{2,water} = u^*_{1,water} \frac{\partial f^*_{ice}}{\partial x^*_1} + u^*_{3,water} \frac{\partial f^*_{ice}}{\partial x^*_3} + \frac{\partial f^*_{ice}}{\partial t^*}.$$

Using the injection velocities inside water at water/ice interface, the kinematic condition becomes

$$n^*_2 \frac{\rho^*_{water}}{\rho^*_{ice}} \frac{d\delta^*_{ice}}{dt^*} = \frac{df^*_{ice}}{dt^*} + n^*_1 \frac{\rho^*_{water}}{\rho^*_{ice}} \frac{df^*_{ice}}{dx^*_1} \frac{d\delta^*_{ice}}{dt^*} + n^*_3 \frac{\rho^*_{water}}{\rho^*_{ice}} \frac{df^*_{ice}}{dx^*_3} \frac{d\delta^*_{ice}}{dt^*},$$

If a control volume like the one shown in Fig. C.3 is considered, then the total energy including the energy added due to the supercooled water impact layer and the heat

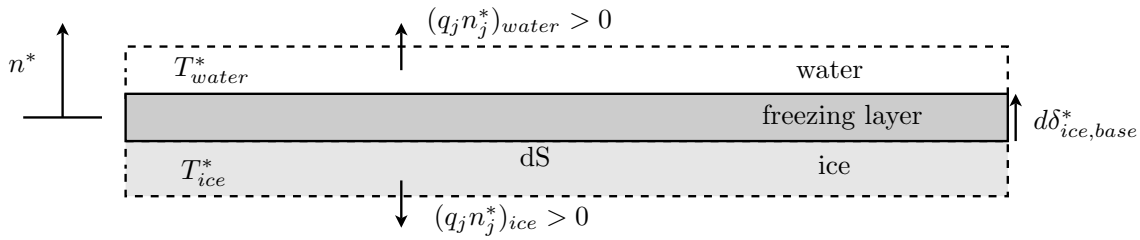

Figure C.3 Growth of ice surface due to heat flux from water and ice.

transfer to the airflow and the water is conserved. This gives

$$\frac{\partial}{\partial t^*} \iiint \rho^*_{water} L^*_{water/ice} dV + \iint \mathbf{q} \bullet \hat{\mathbf{n}} dS = 0.$$

Again using Fourier law of heat conduction and the surface normals at the ice surface f^*_{ice}, the Stefan condition for the ice growth is obtained as

$$k^*_{water} \left[\frac{\partial T^*}{\partial x^*_j}\right]_{water} n^*_j = k^*_{ice} \left[\frac{\partial T^*}{\partial x^*_j}\right]_{ice} n^*_j - L^*_{water/ice} \rho^*_{ice} \frac{d\delta^*_{ice,base}}{dt^*}.$$

This does not include the increment due to the density change from water to ice. This is used in the previously obtained kinematic condition for the ice surface.

BIBLIOGRAPHY

[1] D. Anderson, D. B. Hentschel, and G. A. Ruff. Measurement and correlation of ice accretion roughness. In *36th AIAA Aerospace Sciences Meeting and Exhibition*, January 1998. Paper AIAA-98-0486.

[2] M. Vargas and J. C. Tsao. Observations on the growth of roughness elements into icing feathers. In *45th AIAA Aerospace Sciences Meeting and Exhibition*, January 2007. Paper AIAA-2007-0900.

[3] H. Schlichting and K. Gersten. *Boundary Layer Theory*. Springer-Verlag, 2000.

[4] M. Vargas, J. C. Tsao, and A. P. Rothmayer. Review of role of icing feathers in ice accretion formation. In *SAE Aircraft and Engine Icing International Conference*, Septermber 2007. Paper 2007-01-3294.

[5] X. Presteau, E. Montreuil, A. Leroy, D. Guffond, R. Henry, and P. Personne. Experimental study of the scallop formation on swept cylinder. In *SAE Aircraft and Engine Icing International Conference*, 2007. Paper 2007-01-3296.

[6] M. J. Werle and R. T. Davis. Incompressible laminar boundary layers on a parabola at angle of attack: A study of the separation point. *ASME Journal of Applied Mechanics*, 39(1):7–12, 1972.

[7] National Transportation Safety Board. Aircraft accident report: In-flight icing encounter and uncontrolled collision with terrain Comair flight 3272 Embraer EMB-

120RT, N265CA, Monroe, Michigan, January 9, 1997. Technical report, 1998. Safety Board Report, NTSB/AAR-98/04, PB98-910404, November 1998.

[8] National Transportation Safety Board. Aircraft accident report: In-flight icing encounter and loss of control Simmons Airlines, d.b.a. American Eagle Flight 4184 Avions de Transport Regional (ATR) Model 72-2112, N401AM, Roselawn, Indiana, October 31, 1994. Technical report, 1996. Safety Board Report, NTSB/AAR-96/01, PB96-910401, Volume I, July 1996.

[9] R. W. Gent, N. P. Dart, and J. T. Cansdale. Aircraft icing. *Philosophical Transactions of the Royal Society of London A*, 358:2873–2911, 2000.

[10] G. Poots. *Ice and Snow Accretion on Structures*. John Wiley and Sons., 1996.

[11] H.R. Pruppacher and J.D. Klett. *Microphysics of clouds and precipitation*. Kluwer Academic Publishers, 1997.

[12] S.C. Tan and M. Papadakis. Droplet breakup, splashing and re-impingement on an iced airfoil. In *4th AIAA Theoretical Fluid Mechanics Meeting*, June 2005. Paper AIAA-2005-5185.

[13] W.B. Wright. Users manual for the NASA Glenn ice accretion code LEWICE 2.0. Technical report, NASA Glenn Research Center, 1999. NASA CR-1999-209409.

[14] C.S. Bidwell, D. Pinella, and P. Garrison. Ice accretion calculations for a commercial transport using the LEWICE3D, ICEGRID3D and CMARC programs. In *37th AIAA Aerospace Sciences Meeting and Exhibition*, January 1999. Paper AIAA-99-0250, also NASA Technical Memorandum 1999-208895.

[15] Y. Bourgault, H.. Beaugendre, and W.G. Habashi. Development of a shallow water icing model in FENSAP-ICE. *Journal of Aircraft*, 37(4):640–646, January-February 2000.

[16] H. Beaugendre, F. Morency, and W.G. Habashi. FENSAP-ICE's three-dimensional in- flight ice accretion module: ICE3D. *Journal of Aircraft*, 40(2), March-April 2003.

[17] P. Tran, M.T. Brahimi, I. Paraschivoiu, A. Pueyo, and F. Tezok. Ice accretion on aircraft wings with thermodynamic effects. *Journal of Aircraft*, 32:444–446, 1995.

[18] T. G. Myers. Extension to the messinger model for aircraft icing. *AIAA Journal*, 39(2):211–218, 2001.

[19] T. G. Myers and J.P.F. Charpin. A mathematical model for atmospheric ice accretion and water flow on a cold surface. *International Journal of Heat and Mass Transfer*, 47:5483–5500, 2004.

[20] T. G. Myers, J.P.F. Charpin, and C.P. Thompson. Slowly accreting ice due to supercooled water impinging on a cold surface. *Physics of Fluids*, 14(1):240–256, 2002.

[21] R. W. Gent. TRAJICE2: a combined water droplet and ice accretion prediction code for aerofoils. Technical report, 1994. RAE Technical Report 90054.

[22] B. L. Messinger. Equilibrium temperature of an unheated icing surface as a function of airspeed. *Journal of the Aeronautical Science*, 20(1):20–42, 1953.

[23] Y. Bourgault, Z. Boutanios, and W.G. Habashi. Three-dimensional Eulerian approach to droplet impingement simulation using FENSAP-ICE, part 1: Model, algorithm, and validation. *Journal of Aircraft*, 37(1), January-February 2000.

[24] W.B. Wright. A summary of validation results for LEWICE 2.0. In *37th AIAA Aerospace Sciences Meeting and Exhibition*, January 1999. Paper AIAA-99-0249, also NASA Technical Memorandum 1998-208687.

[25] M. Vargas. Current experimental basis for modeling ice accretions on swept wings. In *4th AIAA Theoretical Fluid Mechanics Meeting*, June 2005. AIAA-2005-5188.

[26] M. G. Potapczuk. A review of NASA Lewis' development plans for computational simulation of aircraft icing. In *37th AIAA Aerospace Sciences Meeting and Exhibition*, January 1999. Paper AIAA-99-0243.

[27] T. Cebeci and K. Kafyeke. Aircraft icing. *Annual Review of Fluid Mechanics*, 35:11–21, 2003.

[28] R.J. Hansman and S.R. Turnock. Investigation of surface water behavior during glaze ice accretion. *Journal of Aircraft*, 26(2):140–147, 1989.

[29] J. Shin. Characteristics of surface roughness associated with leading edge ice accretion. In *32nd AIAA Aerospace Sciences Meeting and Exhibition*, January 1994. Paper AIAA-1994-799.

[30] J. Shin. Characteristics of surface roughness associated with leading edge ice accretion. *Journal of Aircraft*, 33(2):316–321, January 1996.

[31] D. Anderson and J. Shin. Characterization of ice roughness from simulated icing encounters. In *35th AIAA Aerospace Sciences Meeting and Exhibition*, January 1997. Paper AIAA-1997-52.

[32] R. C. Henry, R. J. Hansman, and K. S. Breuer. Heat transfer variation on protuberances and surface roughness elements. *Journal of Thermophysics and Heat Transfer*, 9(1):175–180, 1995.

[33] B. D. Matheis. *Numerical investigation of roughness effects in aircraft icing calculations*. PhD thesis, Iowa State University, 2008.

[34] M. Vargas and E. Reshotko. Physical mechanisms of glaze ice scallop formations on swept wings. In *36th AIAA Aerospace Sciences Meeting and Exhibition*, January 1998. Paper AIAA-1998-491.

[35] M. Vargas and E. Reshotko. Parametric experimental study of the formation of glaze ice shapes on swept wings. In *37th AIAA Aerospace Sciences Meeting and Exhibition*, January 1999. Paper AIAA-1999-94.

[36] M. Vargas and E. Reshotko. LWC and temperature effects on ice accretion formation on swept wings at glaze ice conditions. In *38th AIAA Aerospace Sciences Meeting and Exhibition*, January 2000. Paper AIAA-2000-483.

[37] M. Vargas, J. A. Giriunas, and T. P. Ratvasky. Ice accretion formations on a NACA 0012 swept wing tip in natural icing conditions. In *40th AIAA Aerospace Sciences Meeting and Exhibition*, January 2002. Paper AIAA-2000-483.

[38] W. Olsen and E. Walker. Experimental evidence for modifying the current physical model for ice accretion on aircraft structures. Technical report, 1987. NASA TM 87184.

[39] G. J. Wang and A. P. Rothmayer. Air driven water flow past small scale surface roughness. In *43rd AIAA Aerospace Sciences Meeting and Exhibition*, January 2005. Paper AIAA-2005-0653.

[40] G. J. Wang and A. P. Rothmayer. Properties of thin water films driven by air through surface roughness. In *45th AIAA Aerospace Sciences Meeting and Exhibition*, January 2007. Paper AIAA-2007-0901.

[41] J. C. Tsao and A. P. Rothmayer. A mechanism for ice roughness formation on an airfoil leading edge contributing to glaze ice accretion. In *36th AIAA Aerospace Sciences Meeting and Exhibition*, January 1998. Paper AIAA-98-0485.

[42] J. C. Tsao and A. P. Rothmayer. Triple-deck simulation of surface ice accretion. In *38th AIAA Aerospace Sciences Meeting and Exhibition*, January 2000. Paper AIAA-2000-0234.

[43] J. C. Tsao and A. P. Rothmayer. Transient effects in predicting bulk surface properties for aircraft ice accretion. In *39th AIAA Aerospace Sciences Meeting and Exhibition*, January 2001. Paper AIAA-2001-0677.

[44] J. C. Tsao and A. P. Rothmayer. Application of triple-deck theory to the prediction of glaze ice roughness formation on an airfoil leading edge. *Computer and Fluids*, 31(8):977–1014, 2002.

[45] A. P. Rothmayer. On the creation of ice surface roughness by interfacial instabilities. In *41th AIAA Aerospace Sciences Meeting and Exhibition*, January 2003. Paper AIAA-2003-972.

[46] J. C. Tsao. Cross flow effects on glaze ice roughness formation. In *41st AIAA Aerospace Sciences Meeting and Exhibition*, January 2003. Paper AIAA-2003-1219.

[47] A. P. Rothmayer. Stagnation point icing. In *44th AIAA Aerospace Sciences Meeting and Exhibition*, January 2006. Paper AIAA-2006-1081.

[48] A. P. Rothmayer. Scaling laws for water and ice layers on airfoils. In *41th AIAA Aerospace Sciences Meeting and Exhibition*, January 2003. Paper AIAA-2003-1217.

[49] A. P. Rothmayer. Equations for aircraft icing. Unpublished.

[50] S. H. Davis. *Theory of Solidification*. Cambridge University Press, 2001.

[51] S. C. Gupta. *The Classical Stefan Problem : Basic concepts, modelling and analysis*. Elsevier, 2003.

[52] S. P. Otta and A. P. Rothmayer. Instability of stagnation line icing. *Accepted in Computers & Fluids*, 2008.

[53] K. Stewartson. Multistructured boundary layers on flat plates and related bodies. *Advances in Applied Mechanics*, 14:145–239, 1974.

[54] J. C. Tannehill, D. A. Anderson, and R. H. Pletcher. *Computational Fluid Mechanics and Heat Transfer*. Taylor and Francis, Philadelphia, 1997.

[55] I. H. Abbott and A. E. V. Doenhoff. *Theory of Wing Sections*. Dover, New York, 1959.

[56] S. P. Otta and A. P. Rothmayer. Laminar subsonic, supersonic and transonic boundary-layer flow past a flat plate. *AIAA Journal*, 44(1):102–107, January 2006.

[57] M. Vargas. Current experimental basis for modeling ice accretions on swept wings. *Journal of Aircraft*, 44(1):274–290, 2007.

[58] U. H. Von Glahn and V. H. Gray. Effect of ice formations on section drag of swept NACA 63A-009 airfoil with partial-span leading-edge slat for various modes of thermal ice protection. Technical report, 1954. NACA RM E53J30.

[59] S. Blair. Ice accretion test for two BAC airfoils in the NASA Lewis Icing Research Tunnel. Technical report, August 1967. Boeing Document T6-5049.

[60] A. Shah. Statistical experiment on ice accretion and correlation of ice shapes for swept airfoils. Technical report, May 1969. Boeing Document D6-58363.

[61] R. W. Wilder. A theoretical and experimental means to predict ice accretion shapes for evaluating aircraft handling and performance characteristics. Technical report, November 1978. AGARD Advisory Report No. 127 Aircraft Icing.

[62] T. Hedde and D. Guffond. Improvement of the ONERA 3D icing code. In *30th AIAA Aerospace Sciences Meeting and Exhibit*, January 1993. AIAA Paper 93-0169.

[63] E. Reshotko, M. Vargas, and H. Reed. Ice formation on swept wings-relation to crossflow instability. *Bulletion of the American Physical Society*, 43(9), November 1998.

[64] D. Anderson and J.C. Tsao. Overview of icing physics relevant to scaling. In *SAE/FAA In-Flight Icing/Ground De-Icing International Conference*, June 2005. Paper 2003-01-2130.

[65] D. Anderson. Manual of scaling methods. Technical Report CR-2004-212875, Ohio Aerospace Institute, Brook Park, Ohio, March 2004.

[66] M. B. Bragg. A similarity analysis of the droplet trajectory equation. *AIAA Journal*, 20(12):1681–1686, December 1982.

[67] G. A. Ruff. Analysis and verification of the icing scaling equations. Technical report, March 1986. AEDC-TR-85-30, Vol 1 (Rev).

[68] I Langmuir and K.B. Blodgett. A mathematical investigation of water droplet trajectories. Technical report, February 1946. Army Air Forces Technical Report No. 5418.